Utrecht University

In-situ Raman Spectroscopy to Monitor the Reaction Intermediates of the Electrochemical CO2 Reduction on Well-defined Cu2O Submicro-Crystals

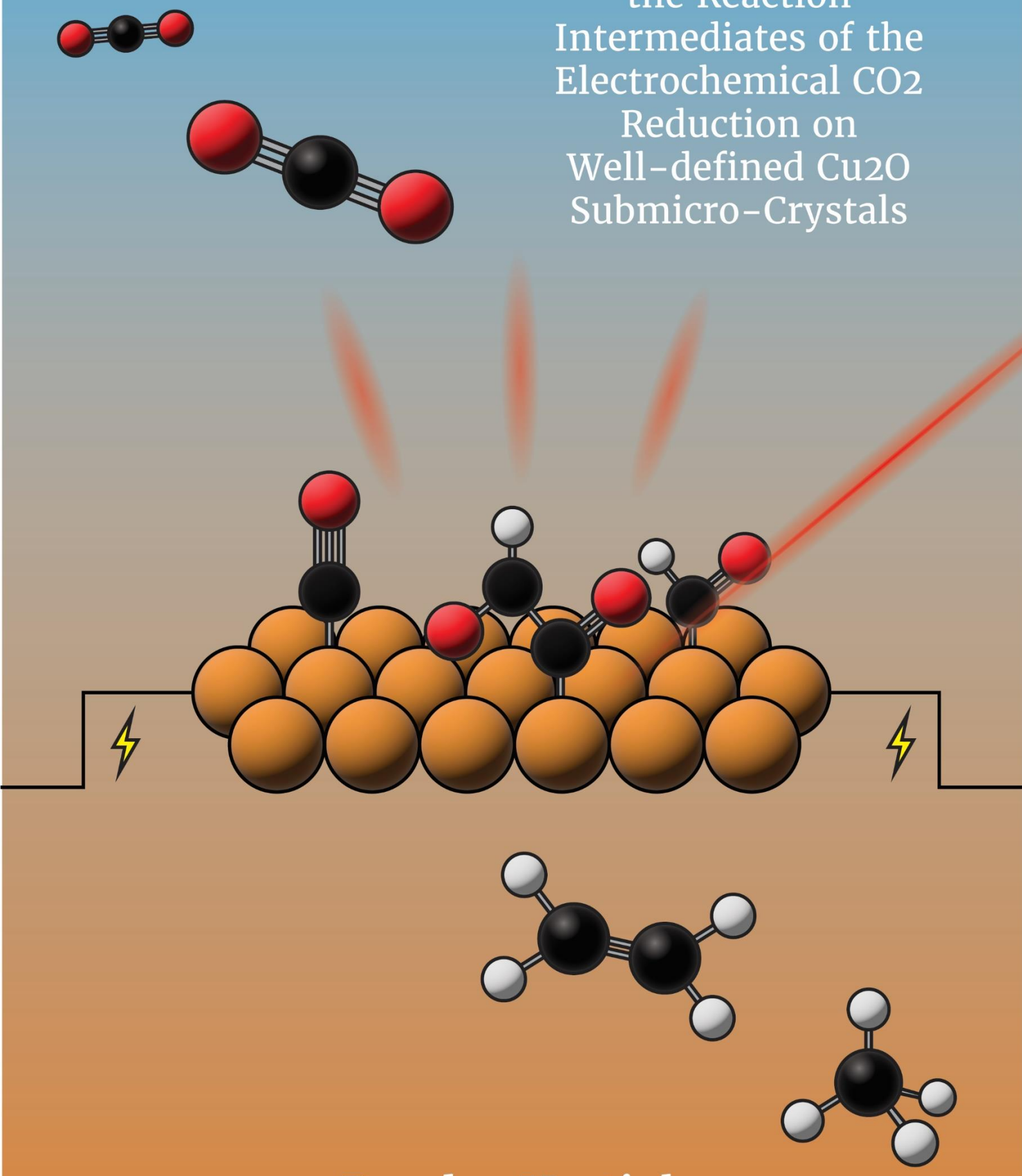

Bas den Hartigh

In-situ Raman Spectroscopy to Monitor the Reaction Intermediates of the Electrochemical CO_2 Reduction on Well-defined Cu_2O Submicro-Crystals

---

Bas den Hartigh

6191940

Supervised by:

Jim de Ruiter

Dr. Ward van der Stam

Dr. Matteo Monai

September 2022

Utrecht University

INORGANIC CHEMISTRY & CATALYSIS

LAYMAN ABSTRACT

Two of the main challenges that we face today in our pursuit to a sustainable society are the storage of renewable energy such as wind and solar, and finding a sustainable alternative production route to fuels and other chemicals such as methane and ethylene. One of the possible solutions to both these problems is the electrochemical reduction of carbon dioxide (CO_2) (eCO2RR), where CO_2 and water are can be converted into methane and ethylene with renewable energy. This reaction happens with the help of a catalyst, which is a material that enables or speeds up a reaction without being used in the reaction itself. The properties of the catalyst, such as the composition, has a large influence on the outcome of the reaction. Copper is known to be a good catalyst for producing products such as methane and ethylene and is thus ideal for a sustainable alternative production route to these chemicals. Despite extensive research, scientists still lack understanding of crucial parts of the reaction itself. When performing the eCO2RR with a copper catalyst, the products that are formed are a mixture of many different chemicals. This makes that this reaction is not industrially applicable since it requires costly separation steps to purify the formed products. Most of the knowledge that is available about the reaction comes from intricate calculations and speculations. Experimental evidence has been mainly found for the initial parts of the reaction, but the later stages of the reaction remain mainly unexplored. In this thesis, Raman spectroscopy has been employed on the eCO2RR on a copper catalyst to monitor the later stages of the reaction. A reaction follows a certain path during which the reactants, in our case CO_2 and H_2O on a copper surface, transition into the products via intermediate species. Raman spectroscopy is able to measure both these intermediate species and the copper surface simultaneously. By employing this technique, we propose to have found experimental evidence for an intermediate in the later stages of the reaction. This intermediate has been found to be of high importance for the outcome of the reaction, i.e. what product will be formed. Knowledge like this enables researchers to engineer new and improved catalysts that are more selective towards one single product, circumventing the costly separation steps and making the eCO2RR more industrially feasible.

ABSTRACT

The electrochemical reduction of CO_2 (eCO2RR) is a promising method to mitigate our carbon emissions and provide alternative production routes to oil for valuable chemicals. Besides that, it can provide a solution to the storage problem of renewable energies by storing it into chemical bonds. Copper is a widely studied catalyst for the eCO2RR because of its unique ability to form valuable C_{2+} products such as ethylene and ethanol which are widely used in the chemical industry as reactant and solvent, respectively. Despite the vast amount of research, there is still much unclear about the dynamic reaction mechanism behind the eCO2RR. It is generally accepted that the rate determining step of the eCO2RR is concerted proton-electron transfer into CO*. However, what happens beyond CO* has solely been speculated by DFT calculations and catalytic tests, but spectroscopic evidence is still lacking as the reaction steps beyond CO* happen extremely fast. In this research, a combination of time-dependent activity measurements with time-resolved *in-situ* Raman is employed on the eCO2RR to study the reaction mechanism beyond CO*. A dynamic system with changing catalytic performance is preferred here to be able to correlate changes in the catalytic activity to changes in the surface intermediates, measured with Raman. For this, well-defined Cu_2O sub-micro crystals with three different morphologies have been employed: cubes with (100) facets, octahedrons with (111) facets, and truncated-octahedrons with a combination of (100) & (111) facets. Different morphologies have been employed as the exposed facets are found to have a large effect on the catalytic performance. Furthermore, oxygen-derived copper catalysts are found to possess an initial increased catalytic performance, but also a quicker deactivation, due to the initial presence of sub-surface oxygen atoms that deplete over time. This dynamic behavior is ideal for this study as changes in the catalytic selectivity can be correlated to simultaneous changes in the surface intermediates, measured with the *in-situ* Raman. The time-dependent activity measurements reveal a dynamic catalytic behavior with a significant shift in selectivity for methane and ethylene over time. The time-resolved Raman data shows that the surface intermediates of the catalyst under working conditions shifts from being dominated by linear CO to new intermediates beyond CO with vibrations between 460 – 510 cm^{-1}, which became dominant after ~30 min at -1.0V. Before and after this shift in surface intermediates, the catalysts were forming methane and ethylene, only with different efficiencies. This suggests that there are two reaction pathways towards methane and ethylene, the first involves linear CO, the second involves the new intermediates beyond CO. Furthermore, since both methane and ethylene are produced with intermediates beyond CO, it is suggested that they possess a shared intermediate beyond CO. This shared intermediate is suggested to be located at 495 cm^{-1} in the time-dependent Raman measurements and possesses an aldehyde nature, -CHO, based on literature. Another new vibration that is located between 500 – 510 cm^{-1} is suggested to be more methane directing, and a new vibration at 460 cm^{-1} to be a bridged CO modality. This thesis reveals that the combination of time-dependent activity and time-resolved Raman measurements on a dynamic system is beneficial for elucidating on the reaction mechanism of the eCO2RR.

ABBREVATIONS

CCS	=	Carbon capture and storage
CCU	=	Carbon capture and utilization
eCO2RR	=	Electrochemical CO_2 Reduction Reaction
HER	=	Hydrogen evolution reaction
OER	=	Oxygen evolution reaction
RDS	=	Rate determining step
GCE	=	Glassy carbon electrode
CPE	=	Carbon paper electrode
ODC	=	Oxygen-derived copper
XRD	=	X-Ray diffraction
EM	=	Electron microscopy
SEM	=	Scanning electron microscopy
F.E.	=	Faradaic efficiency
CV	=	Cyclic voltammetry
GC	=	Gas chromatograph
LSPR	=	Local surface plasmon resonance
OCP	=	Open circuit potential

TABLE OF CONTENTS

1 INTRODUCTION 12

2 THEORETICAL BACKGROUND 22

2.1 Principles of Electrochemical CO_2 Reduction 22
2.1.1 Electrochemical Cell Design 23
2.1.2 The Electrolyte 25
2.1.3 Kinetic Barriers 27

2.2 Raman Spectroscopy 29
2.2.1 Surface Enhanced Raman Spectroscopy 32

3 METHODOLOGIES 34

3.1 Synthesis 34

3.2 Electrode preparations 35

3.3 Characterization 35

3.4 Catalytic Testing 36

3.5 Raman Measurements 37

4 RESULTS 38

4.1 Material Characteristics 38

4.2 Catalytic Performance 41

4.3 Post-catalytic Structure & Morphology 44

4.4 Time-dependent catalytic behavior 47

4.5 Raman spectroscopy 49
4.5.1 Potential Dependent Raman 49
4.5.2 Temporal Spectral Evolution 52

CONCLUSIONS 58

OUTLOOK 60

BIBLIOGRAPHY 61

ACKNOWLEDGMENTS 67

APPENDIX A. SUPPLEMENTARY FIGURES 68

LIST OF FIGURES

FIGURE 1: SCHEMATIC OF THE ECO2RR, WHERE TWO ELECTRODES ARE SUBMERGED INTO AN ELECTROLYTE. CO_2 IS REDUCED INTO PRODUCTS SUCH AS HCOOH, CO, CH_4, AND C_2H_4 AT THE CATHODE AND WATER IS OXIDIZED INTO O_2 AT THE ANODE. 12

FIGURE 2 A: OVERVIEW OF SEVERAL OF THE TRANSITION METALS WITH THEIR MAIN PRODUCT FOR THE ECO2RR. B: THE ADSORPTION ENERGIES FOR THE CO* AND H* INTERMEDIATES FOR THE SAME TRANSITION METALS. FIGURES ADAPTED FROM BAGGER ET AL. [12] 13

FIGURE 3: CATALYTIC SELECTIVITY OF POLYCRYSTALLINE COPPER IN 0.1M $KHCO_3$ SATURATED WITH CO_2 (PH=6.8) IN THE POTENTIAL RANGE OF -0,4V TILL -1,2V . DATA ARE FROM HORI ET AL.[13] (HOLLOW POINTS) AND KUHL ET AL.[14] (FILLED POINTS) FIGURE ADAPTED FROM NITOPI ET AL. [8] 15

FIGURE 4: : OVERVIEW OF ALL THE PROPOSED INTERMEDIATES FOR THE ECO2RR TOWARDS METHANE, ETHYLENE AND ETHANOL. WITH THE Y-AXIS SHOWING THE AMOUNT OF ELECTRONS TRANSFERRED AND THE X-AXIS THE AMOUNT OF CARBON ATOMS. FIGURE ADAPTED FROM NITOPI ET AL. [8] 17

FIGURE 5: THE TWO BINDING MODES FOR THE CO* INTERMEDIATE ON A METAL SURFACE. LEFT: LINEAR CO, WHERE THE CARBON IS SINGLE BONDED TO THE METAL. RIGHT: BRIDGED CO WHERE THE CARBON IS DOUBLE BONDED TO THE METAL 18

FIGURE 6: VIBRATION MODES WITH THEIR CORRESPONDING FREQUENCY (CM^{-1}) OF LINEARLY ADSORBED CO* ON A CU CATALYST. LEFT VIBRATION IS THE C-O STRETCH VIBRATION WHICH IS VISIBLE AT ~2000 CM^{-1}, THE MIDDLE VIBRATION IS THE CU-CO FRUSTRATED ROTATION VIBRATION AT 280CM^{-1}, AND THE RIGHT VIBRATION IS THE CU-C STRETCH VIBRATION AT 360 CM^{-1}. 19

FIGURE 7: SCHEMATIC REPRESENTATION OF A METALLIC COPPER CATALYST AND AN ODC CATALYST. THE ODC CATALYST POSSESSES A ROUGHENED SURFACE WITH RESIDUAL OXYGEN ATOMS, RESULTING IN HIGHER VALENT COPPER ATOMS AT THE SURFACE. 20

FIGURE 8: SCHEMATICS OF LEFT: CU_2O CUBE, MIDDLE: OCTAHEDRON, RIGHT: TRUNCATED-OCTAHEDRON 21

FIGURE 9: A: SCHEMATIC OF THE ELECTROCHEMICAL H-CELL, CONSISTING OF TWO COMPARTMENTS: THE ANODE AND THE CATHODE, SEPARATED WITH A PROTON-SELECTIVE MEMBRANE. A REFERENCE ELECTRODE IS ADDED TO THE CATHODE SIDE, AND CO_2 IS PURGED THROUGH THE SYSTEM FROM THE BOTTOM. B: SCHEMATIC FOR THE WORKING ELECTRODE PART OF A GDE, CONSISTING OF A POROUS GAS DIFFUSION LAYER, A CATALYST LAYER AND THE ELECTROLYTE. CO_2 IS PURGED THROUGH THE GAS DIFFUSION LAYER AND PRODUCTS EXIT VIA THE OTHER SIDE. 23

FIGURE 10: FREE ENERGY DIAGRAMS FOR THE TWO POSSIBLE WAYS TO PRODUCE SURFACE ADSORBED HYDROGEN. THE LEFT DIAGRAM IS IN ACIDIC SOLUTIONS WHEN H^+ IS PRESENT, AND THE RIGHT DIAGRAM IS IN BASIC SOLUTION WHEN NO H^+ IS PRESENT. THE ACTIVATION ENERGY IS SIGNIFICANTLY LOWER IN ACIDIC SOLUTIONS. FIGURE ADAPTED FROM WANG ET AL.[51]. 25

FIGURE 11: PARTIAL CURRENT DENSITY TOWARDS C_{2+} PRODUCTS FOR DIFFERENT CATIONS AT THE CU(111) AND CU(100) SURFACE. THE DOTS REPRESENT THEORETICAL DATA POINTS AND THE LINE EXPERIMENTAL DATA. FIGURE ADAPTED FROM RINGE ET AL.[54] 26

FIGURE 12: CALCULATED ENERGY DIAGRAMS FOR THE ECO2RR TOWARDS METHANE ON THE CU(211) SURFACE. APPLYING AN OVERPOTENTIAL LOWERS THE OVERALL ΔG AND THE ENERGY BARRIERS FOR EACH REACTION STEP. FIGURE ADAPTED FROM NØRSKOV ET AL. [57] 27

FIGURE 13: THE TWO DIFFUSIVE BARRIERS THAT OCCUR IN THE ECO2RR. LEFT VISUALIZES THE DEPENDENCY ON SURFACE PROTONS WHICH ARE REQUIRED IN THE PROTON-COUPLED REACTIONS STEPS. BESIDES THE ECO2RR, THE SURFACE PROTONS ARE ALSO USED IN THE COMPETING HER. THE RIGHT VISUALIZES THE DEPENDENCY ON CO* COVERAGE, WHICH IS AN IMPORTANT PARAMETER FOR THE PRODUCTION OF C_{2+} PRODUCTS TO FORM A C-C BOND. TOO LOW CO* COVERAGE INHIBITS THE C-C COUPLING AND RESULTS IN LESS C_{2+} PRODUCTION. 28

FIGURE 14: DIFFERENT VIBRATION MODES FOR THE SYMMETRIC CO_2 MOLECULE, WHERE RAMAN AND IR ARE COMPLEMENTARY TO EACH OTHER. 29

FIGURE 15: WORKING PRINCIPLE OF RAMAN SPECTROSCOPY. MOST OF THE INCOMING LIGHT GETS ELASTICALLY SCATTERED, RESULTING IN RAYLEIGH SCATTERING. SOME OF THE INCOMING LIGHT GETS INELASTICALLY SCATTERED, RESULTING IN AN ENERGY SHIFT (STOKES OR ANTI-STOKES SHIFT). 30
FIGURE 16: SCHEMATIC REPRESENTATION OF THE RESONANCE OF INCOMING LIGHT WITH THE PLASMON VIBRATION, RESULTING IN AN INCREASE OF THE ELECTROMAGNETIC FIELD 32
FIGURE 17: PICTURE OF THE DESIGNED IN-SITU RAMAN CELL WITH ITS COMPONENTS. 37
FIGURE 18: HIGH-RESOLUTION SEM IMAGES OF ALL THREE CATALYSTS WITH THEIR RESPECTIVE X-RAY DIFFRACTOGRAMS AND A REFERENCE DIFFRACTOGRAM FOR CU_2O. 38
FIGURE 19: RECORDED CVS FOR THE CU_2O CUBES AND OCTAHEDRONS FROM -1,4V TO 1,6V. BOTH CATALYSTS SHOW A DISTINCT REDUCTION AND OXIDATION AREA. 40
FIGURE 20: LEFT: AVERAGE CATALYTIC PERFORMANCE FOR ALL THREE CATALYSTS AT -1,2V AND -1,4V OVER 30 MINUTES. ONLY THE GAS PRODUCTS HAS BEEN PLOTTED HERE. RIGHT: OVERALL CATALYTIC PERFORMANCE FOR ALL THREE CATALYSTS AS THE SAME OVERPOTENTIALS, NOW ALSO WITH HCOOH ADDED. 41
FIGURE 21: UPPER GRAPH: CURRENT AND POTENTIAL OVER TIME FOR THE CATALYTIC TEST OF THE TRUNCATED-OCTAHEDRONS AT -1,2V. A CLEAR DECREASE IN BOTH CAN BE SEEN AFTER ~650 MINUTES, INDICATING THE MALFUNCTIONING OF THE SYSTEM. LOWER GRAPH: F.E. OVER TIME FOR THE SAME EXPERIMENT, WITH THE SAME DECREASE AFTER THE MALFUNCTIONING HAPPENS. 43
FIGURE 22: UPPER GRAPH: EX-SITU XRD MEASUREMENTS OF THE CUBES AND OCTAHEDRONS AFTER 5 AND 60 MINUTES AT -1.0V. WITH THE RED LINES INDICATING THE CU_2O (111) & (100) AND THE BLUE LINES THE CU(111) & (100). LOWER GRAPH: EX-SITU SEM PICTURES OF THE CUBES AND OCTAHEDRONS AFTER 5, 15 & 60 MINUTES AT -1.0V. THE CUBES SHOW MORE DENDRITE FORMATION OVER TIME THAN THE OCTAHEDRONS. 45
FIGURE 23: TIME-DEPENDENT ACTIVITY DATA FOR ALL THREE CATALYSTS AT -1,8$V_{AG/AGCL}$ (TOP) & -2,0$V_{AG/AGCL}$ (BOTTOM). THE LEFT TWO GRAPHS SHOW THE F.E. OVER TIME FOR ALL 4 THE GAS PRODUCTS, THE RIGHT TWO GRAPHS SHOW THE PARTIAL CURRENT OVER TIME FOR C_2H_4 AND CH_4. 47
FIGURE 24: AVERAGE OF 25 RAMAN SPECTRA TAKEN AT DIFFERENT OVERPOTENTIALS FOR THE CU_2O OCTAHEDRONS. PEAKS FOR REACTION INTERMEDIATES, ELECTROLYTE SPECIES, THE GLASSY CARBON SUBSTRATE AND PVP CAN BE FOUND. THERE IS ALSO THE UNKNOWN PEAK AT 500 CM^{-1}. 49
FIGURE 25: TIME-RESOLVED RAMAN SPECTRA RECORDED ON THE CUBES (LEFT) AND THE OCTAHEDRONS (RIGHT). ALL MEASUREMENTS WERE TAKEN IN THE TIMESPAN OF 2 HOURS AT -1.0V. THE BOTTOM SHOWS THE ZOOMED IN PARTS OF THE 400 CM^{-1} AND 2000 CM^{-1} REGIONS FOR EACH EXPERIMENT. 52
FIGURE 26: THE VIBRATION AT 495 CM^{-1} IS SUGGESTED TO BE AN ETHYLENE DIRECTING SPECIES (TOP) AND THE 500 CM^{-1} VIBRATION IS SUGGESTED TO BE A METHANE DIRECTING SPECIES WHICH ALSO HAS A SLIGHTLY STRONGER BOND TO THE METAL SURFACE THAN THE 495CM^{-1}, AS INDICATING BY THE THICKER BOND. 53
FIGURE 27: LEFT: EVOLUTION OF THE 500 CM^{-1} RAMAN BANDS OVER TIME FOR THE CUBES AND OCTAHEDRONS, WITH BLUE SPECTRA REPRESENTING THE START OF THE EXPERIMENT AND YELLOW THE END OF THE EXPERIMENT. RIGHT: THE PEAK RATIO B2/B1 OVER TIME FOR THE CUBES AND OCTAHEDRONS. 54
FIGURE 28: SPECTRAL EVOLUTION OF THE FRUSTRATED ROTATION VIBRATION OF LINEAR CO (P1 @ 280 CM^{-1}) AND THE STRETCH VIBRATION OF LINEAR CO (P2 @ 360 CM^{-1}) IN THE FIRST 35 MINUTES OF THE TEMPORAL RAMAN MEASUREMENTS. THE LEFT GRAPH IS FOR THE CUBES AND THE RIGHT GRAPH FOR THE OCTAHEDRONS. THE BOTTOM TWO GRAPHS SHOW THE RATIO OF P2/P1 OVER THIS TIMEFRAME WHERE A DECREASE IS FOUND FOR THE CUBES AND AN INCREASE FOR THE OCTAHEDRONS BEFORE LINEAR CO DISAPPEARS FROM THE SURFACE (AFTER 35 MINUTES). 55
FIGURE 29: SIMPLIFIED VERSION OF THE COMPLETE OVERVIEW OF ALL THE REACTION INTERMEDIATES AS PROVIDED BY NITOPI ET AL.[10]. THE KEY INTERMEDIATES HAVE BEEN ADDED TOGETHER WITH THEIR PROPOSED VIBRATIONAL ENERGIES AS DISCUSSED IN THE LAST SECTION. 57
FIGURE 30: PICTURE OF THE H-CELL FOR THE CATALYTIC TESTS WITH THE THREE DIFFERENT ELECTRODES. 68
FIGURE 31: CATALYTIC SELECTIVITY OF THE OCTAHEDRONS AFTER 20 MINUTES AT -1.0V. ONLY ~3% C_2H_4 IS FOUND AT THESE OVERPOTENTIALS. 68
FIGURE 32: ZOOMED OUT SEM IMAGES OF THE CU_2O CUBES (TOP), TRUNCATED-OCTAHEDRONS (MIDDLE) AND OCTAHEDRONS (BOTTOM). 69

FIGURE 33: THE DUPLO EXPERIMENTS OF THE TIME-DEPENDENT ACTIVITY DATA FOR ALL THREE CATALYSTS AT -1,2V (TOP) & -1,4V (BOTTOM). THE LEFT TWO GRAPHS SHOW THE F.E. OVER TIME FOR ALL 4 THE GAS PRODUCTS, THE RIGHT TWO GRAPHS SHOW THE PARTIAL CURRENT OVER TIME FOR C_2H_4 AND CH_4. 69
FIGURE 34: AVERAGE OF 25 RAMAN SPECTRA TAKEN AT THE GIVEN OVERPOTENTIALS FOR THE CU_2O CUBES IN 0.1M $KHCO_3$. 69
FIGURE 35: TEMPORAL RAMAN MEASUREMENTS OF THE TRUNCATED-OCTAHEDRONS. THE TRUNCATED-OCTAHEDRONS GAVE VERY LITTLE SIGNAL FROM INTERMEDIATES FROM THE ECO2RR. 69
FIGURE 36: RAMAN SPECTRA OF THE CU_2O CATALYST AND THE GLASSY CARBON AT OCP IN CO_2-SATURATED 0.1M $KHCO_3$ (PH=6.8). THE TOP THREE SPECTRA ARE FROM $KHCO_3$, PVP, AND L-ASCORBID ACID POWDERS. 69

1 INTRODUCTION

The ever-increasing atmospheric concentration of carbon dioxide (CO_2), with all its consequences such as rising global temperatures, gives rise to high demand for new technologies to reduce its concentration[1–2]. Two possible ways to reduce the concentration are carbon capture and storage (CCS) and carbon capture and utilization (CCU). The difference between both techniques is that CCU utilizes the captured CO_2 to use as chemical feedstock, where CCS merely stores it underground. The main disadvantage of CCS that it requires expensive equipment to capture and purify the CO_2, while it does not provide any significant financial benefit[3]. CCU on the other hand, utilizes the captured CO_2 in chemical processes to convert it into chemicals and fuels[4]. Employing CCU will tackle three problems simultaneously: (1) it lowers the atmospheric CO_2 concentrations, (2) it offers a sustainable alternative for the petrochemical routes towards chemicals and fuels, and (3) it stores intermittent renewable energies in chemical bonds. The main problem of CCU is the inherent thermodynamic stability of CO_2 (ΔG_f^0 = −394 kJ/mol in gas phase), making the chemical conversion of CO_2 energy demanding[5]. Because of this, the chemical conversion of CO_2 strongly relies on catalysts to activate the CO_2 and lower the chemical energy barriers[6]. The catalytic conversion of CO_2 can be done using gas-phase reactions, liquid-phase reactions, photocatalytic reactions, or electrochemical reactions[7]. This thesis focuses on the latter, the electrochemical conversion of CO_2.

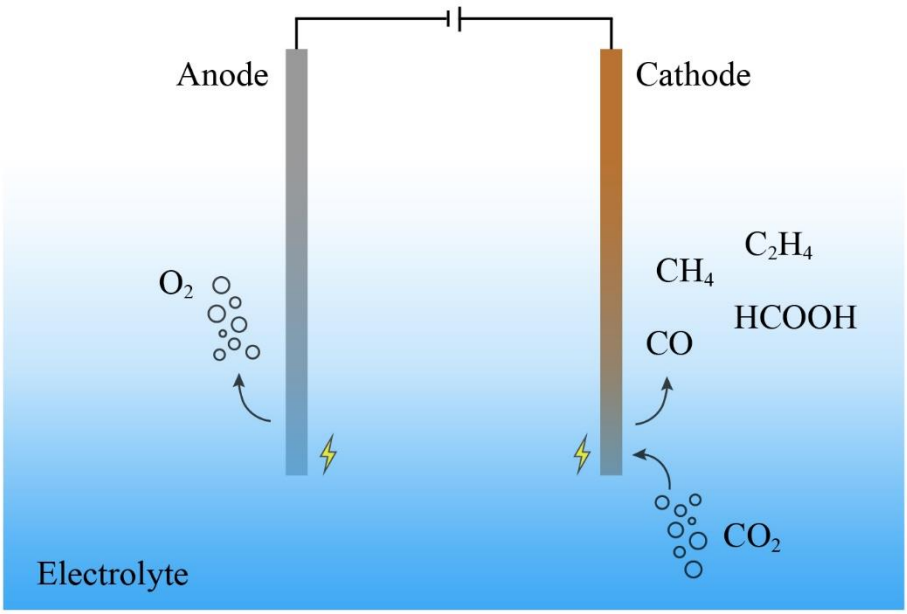

Figure 1: Schematic of the eCO2RR, where two electrodes are submerged into an electrolyte. CO_2 is reduced into products such as HCOOH, CO, CH_4, and C_2H_4 at the cathode and water is oxidized into O_2 at the anode.

The electrochemical conversion of CO_2 happens via a reduction reaction and is called the electrochemical CO_2 reduction reaction (eCO2RR). The eCO2RR is a redox half reaction of the form:

$$x CO_2 + n H^+ + n e^- \rightarrow \text{product(s)} + y H_2O \quad (1)$$

$$H_2O \rightarrow O_2 + 4H^+ + 4e^- \quad (2)$$

Since it is a redox reaction, there is also an oxidation reaction happening at the anode, which is often the oxygen evolution reaction (OER) (equation 2). Figure 1 shows a schematic of a setup for the eCO2RR. Both electrodes are submerged in an electrolyte, which is a salt solution for the transportation of reactants and products and to make the whole system conductive and will be explained in more detail in 2.1.2. CO_2 is purged through the system and solubilized in the electrolyte, though with low solubility, and is reduced at the cathode into water and valuable products, such as CO, HCOOH, CH_4 and C_2H_4. Hence, the cathode is the most important part in the eCO2RR, and the majority of research has been conducted on the cathode. The cathode often consists of a catalyst material of a transition metal deposited on a conductive material[8,9]. The anode is often a platina catalyst where water is oxidized into oxygen and protons.

The first reported study on the eCO2RR dates back to 1870, when Royer was able to reduce CO_2 to formic acid[10]. Since then, researchers have been studying the eCO2RR, but it really gained interest in the last couple of decades thanks to its potential importance for tackling the anthropogenic CO_2 problem. Yoshio Hori was the first one to report the full product analysis of the eCO2RR with a variety of transition metals as the catalyst[11]. Figure 2a shows the main products for these metals when employed in the eCO2RR with their respective Faradaic efficiency (F.E.)[12]. The F.E. shows the efficiency with which the total amount of electrons put into the system went into that particular product. The metals were divided into 4 different groups, depending on their main product: H_2 (red), CO (blue), HCOOH (yellow), and beyond CO (turquoise). The main product of a metal mainly depends on the binding energies of key intermediates for the eCO2RR. The metals in red are essentially inactive for the eCO2RR, as H_2 is not a product from the reduction of CO_2, but from the reduction of H_2O, also called the hydrogen evolution reaction (HER):

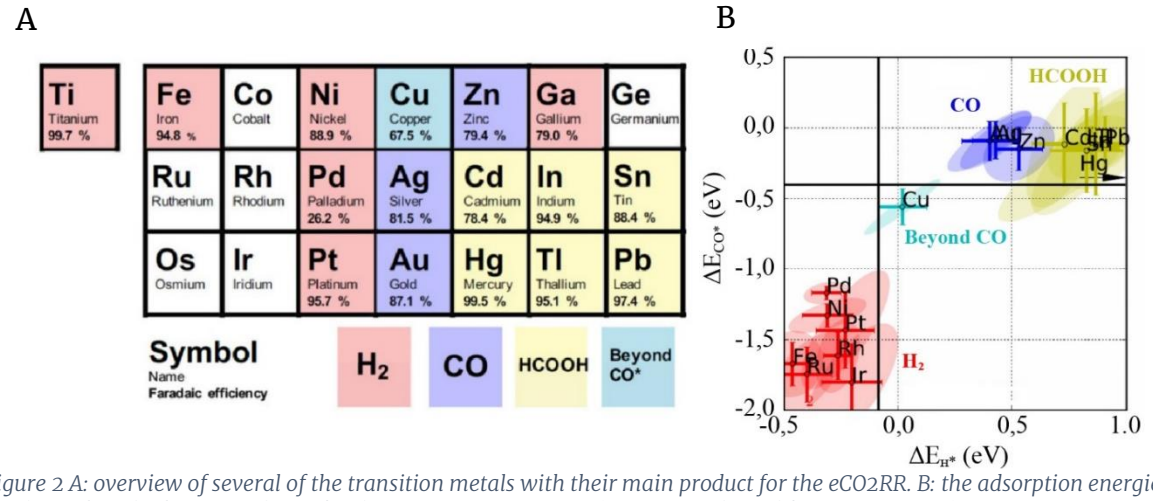

Figure 2 A: overview of several of the transition metals with their main product for the eCO2RR. B: the adsorption energies for the CO and H* intermediates for the same transition metals. Figures adapted from Bagger et al.* [12]

$$2H^+ + 2e^- \rightarrow H_2 \qquad (3)$$

The HER is commonly referred to as the competing reaction as it steals electron density from being used in the eCO2RR, reducing the energy efficiency. Lastly, there are the metals that mainly produce the simpler chemicals CO & HCOOH, which are products from the eCO2RR. Lastly, there is copper, which has the unique ability to form products beyond CO such as CH_4 and is even able to facilitate C-C coupling to form products as C_2H_4. CH_4 and C_2H_4 have a higher energy density and have more uses in the chemical industry than CO and HCOOH, which results in copper being the most widely studied catalyst for the eCO2RR as it is the only metal that is able to produce CH_4 and C_2H_4.

It was long poorly understood why copper was the only metal to form products beyond CO. To understand this, Bagger et al. conducted a theoretical study using DFT to calculate the adsorption energies of key intermediates such as H* and CO* for the eCO2RR on the metals in Figure 2a, and the results are shown in Figure 2b[12]. This graph plots the binding energy of CO* on the y-axis and H* on the x-axis and the metals have the same color code as Figure 2a to indicate their main product. H* is an important intermediate for the eCO2RR as it is the key intermediate for the competing HER and it is used in the eCO2RR for concerted proton-electron reaction steps where a hydrogen atom is attached to an intermediate[8]. CO* is generally accepted as the key intermediate for the eCO2RR as will be explained later in this chapter. Figure 2b shows that too strong adsorption energies for CO* leads to H_2 as the main products, due to CO* poisoning. On the contrary, too weak adsorption energies for CO* results in CO or HCOOH as the main products. The moderate CO* adsorption energy for copper makes that it will not suffer from CO* poisoning and that CO* does not quickly desorb from the surface enabling the further reduction into the products as CH_4 and C_2H_4. Hereinafter, unless stated otherwise, it is assumed that the eCO2RR is performed on a copper-based catalyst.

Just like all catalytic processes, reaction parameters have a large influence on the catalytic activity and selectivity. The most important parameter in the eCO2RR is the applied overpotential, which is the applied potential between the anode and the cathode, expressed in voltage (V). Hori already showed the dependence of selectivity on the applied overpotential in his early work on the eCO2RR and is shown in Figure 3 (hollow points)[13]. Here, the F.E. towards several products is given on the y-axis against the applied overpotential ranging from approximately $-0.4V_{RHE}$ till $-1.05V_{RHE}$, measured on a polycrystalline copper catalyst. The overpotentials are given on the reversible hydrogen electrode (RHE) scale throughout the thesis unless stated otherwise. A clear change in selectivity can be seen over this range of overpotentials, where the lowest overpotentials favor the formation of the competing hydrogen product. Increasing the overpotential (towards more negative values), results in a decrease of hydrogen and an increase of the simpler products from the eCO2RR such as CO and HCOOH. Increasing the overpotential even further, the hydrocarbons CH_4 and C_2H_4 start to dominate with a maximum at ~-1.05V. Later, the work of Kuhl et al. on the same system, but in the potential range of -0.6V till -1.2V, confirmed these findings of Hori (filled points in Figure 3)[14]. However, the work of Kuhl et al. shows that the optimum

potential for the eCO2RR, with the lowest F.E. of hydrogen, is at -1.05V, which is coincidentally the maximum potential that Hori measured. These works show that the catalytic selectivity is strongly dependent on the applied overpotential and that it is an important factor to consider when performing the eCO2RR.

Hori and Kuhl both used polycrystalline copper for these experiments. However, 6 years later in 1995, Hori et al. showed that the eCO2RR also possesses a facet-dependency by using single crystal electrodes[15]. By employing single crystal (100), (110) and (111) copper electrodes, the catalytic selectivity changes drastically with Cu(100) predominantly producing C_2H_4 (F.E.: 37.1%) and Cu(111) primarily producing CH_4 (F.E.: 38.9%). Other studies in the following decades confirmed this finding that the (100) and (111) facets predominantly produce C_2H_4 and CH_4, respectively[16,17]. In his paper, Hori already revealed that the adsorption energy of CO on the different facets is relevant for this difference in selectivity, showing the importance of CO for the eCO2RR. Not much later in the same year, Hori et al. published an *in-situ* infrared study on the eCO2RR showing the presence of adsorbed CO* species under working conditions, evidencing that CO* is an intermediate species for the eCO2RR[18].

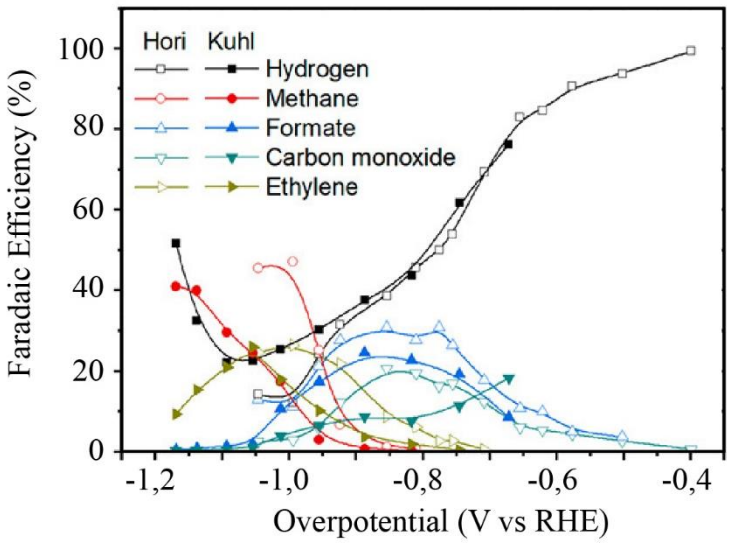

Figure 3: Catalytic selectivity of polycrystalline copper in 0.1M $KHCO_3$ saturated with CO_2 (pH=6.8) in the potential range of -0,4V till -1,2V . Data are from Hori et al.[13] (hollow points) and Kuhl et al.[14] (filled points) Figure adapted from Nitopi et al. [8]

Only 2 years later in 1997, they published a work on the electrochemical reduction of CO instead of CO_2[19]. This work included a reaction pathway diagram for both CH_4 and C_2H_4 from CO and their main finding was that in the early stages of the reaction, CH_4 and C_2H_4 follow different reaction pathways. This was one of the first studies on the reaction mechanism towards the hydrocarbons. In their paper, they suggest that the C-C coupling step, which is a necessary step for C_{2+} products such as C_2H_4, happens via the dimerization of CH_2* to directly form C_2H_4 or via the insertion of CO into CH_2* to form $OCCH_2$*. However, since then, many studies on the reaction mechanism have followed and there is a large debate about the exact nature of the C-C coupling mechanism[20,21]. Nitopi et al. have published an overview of the proposed reaction pathways from the many studies that followed after Hori, which is shown in Figure 4[8]. The y-axis represents the number of electrons transferred during the reaction and the x-axis shows the number of carbon atoms in the intermediate or product. The black lines are from the early works of Hori et al., where you can see their proposed reaction pathways towards CH_4 and C_2H_4 following two different paths. They proposed that CH_4 and C_2H_4 start following different pathways from the CO* intermediate. Up to this day, the concept of CH_4 and C_2H_4 following two different pathways early on is still accepted[22,14]. Koper et al. proposed in 2012 that C_2H_4 has two different possible reaction pathways[22]. One that has a common intermediate with CH_4, while the other selectively produces C_2H_4, presumably via the dimerization of CO* into OCCO*. These two pathways are visible in the overview in Figure 4, where the dimerization of CO* results into C_2H_4 production, and where the reduction of CO* into CHO* could direct both to CH_4 and C_2H_4. This diagram also shows why CO* is generally seen as the key intermediate for the eCO2RR, as all products requiring more than 2 electrons ($\geq 2e^-$) proceed via CO*. Moreover, the further reduction of CO* is often the rate determining step (RDS), as indicated by the arrowed lines coming off CO* in Figure 4. The RDS is the reaction step with the slowest kinetics and determines the reaction rate of the overall reaction[23].

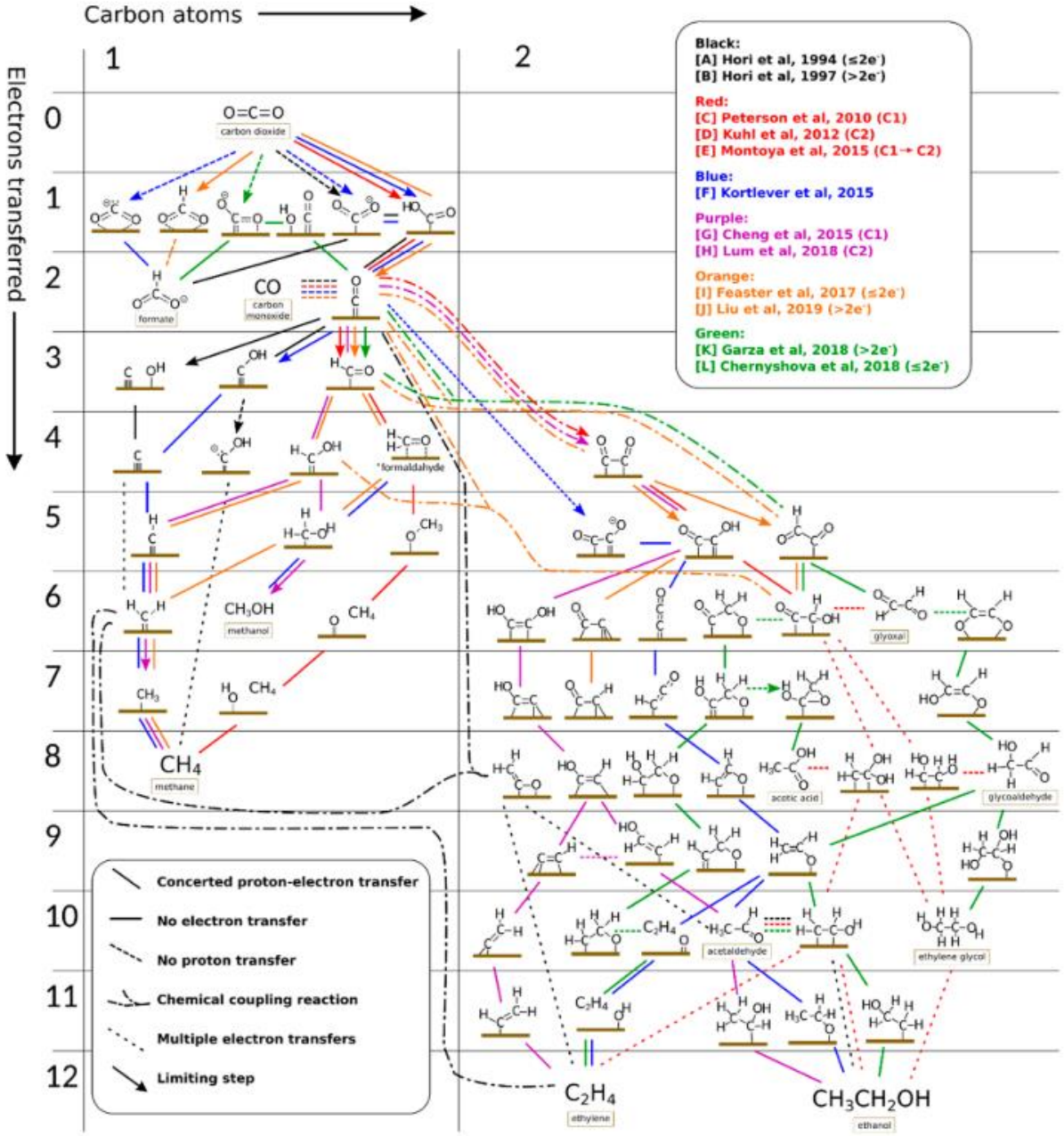

Figure 4: : Overview of all the proposed intermediates for the eCO2RR towards methane, ethylene and ethanol. With the y-axis showing the amount of electrons transferred and the x-axis the amount of carbon atoms. Figure adapted from Nitopi et al. [8]

Most of the intermediates in Figure 4 are proposed via theoretical calculations such as DFT, but experimental evidence is lacking for intermediates beyond CO* (or >2e⁻)[24,25,26]. Spectroscopic techniques such as IR and Raman are ideal for measuring intermediates and providing experimental evidence[27,28,29]. Both techniques can be employed *in-situ* and are able to measure the vibrations of intermediates. Raman often has the preference here over IR due to its ability to measure in the low wavenumber region (100-500 cm^{-1}), where metal-intermediate vibrations are found, and Raman does not suffer from signal from the water, as will be explained in section 2.2. Many of the spectroscopic studies on the eCO2RR are based on the CO* intermediate[30] because (1) it is an important intermediate, what happens next dictates mainly which product will be formed, and (2) as it is the RDS, it remains on the surface for long enough to be measured, simplifying the measurements. As previously mentioned, Hori et al. already performed *in-situ* IR to find evidence for the CO* intermediate and concluded that this intermediate is linearly bound to the surface, like gaseous CO on metal substrates (left in figure 5)[18]. However, in their paper, they already mentioned the possibility of a bridged binding mode of CO* on Cu(111) (right in figure 5). Today, the bridged CO modality is considered to be an inactive species towards C_{2+} products, which is predominantly present at Cu(111)[31]. Later, it was found that linearly bound CO (linear CO) has two different binding modes itself: (1) low-frequency band CO (LFB-CO) and (2) high frequency band CO (HFB-CO)[32]. An et al. employed *in-situ* time-resolved surface-enhanced Raman spectroscopy to investigate the reactivities of these two binding modes[27]. They found that the more static HFB-CO is prone to desorption and thus CO formation, whereas the dynamic LFB-CO is more prone to dimerization and thus responsible for C_{2+} formation. Another important parameter is the CO* coverage, Roldan et al. published an *in-situ* surface-enhanced Raman study on the CO* coverage during catalysis, and found that the coverage is strongly dependent on the applied overpotential[33]. CO* possesses Raman active vibrations in two different regions in a Raman spectrum: (1) the high wavenumber region (~2000 cm^{-1}), corresponding to the vibration between **C-O** (left most vibration in figure 6), and (2) the lower wavenumber region (~300 cm^{-1}) corresponding to the vibration between the substrate and the carbon (**M-C**O, where M=metal) (right two

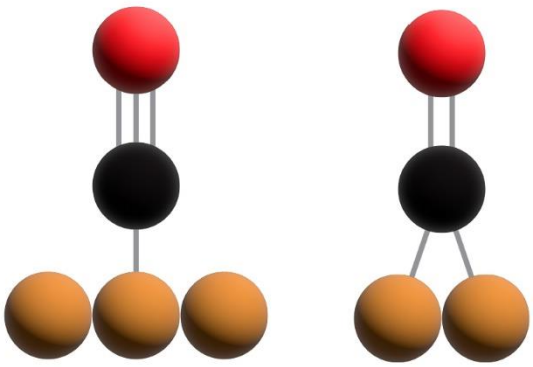

Figure 5: The two binding modes for the CO intermediate on a metal surface. Left: linear CO, where the carbon is single bonded to the metal. Right: bridged CO where the carbon is double bonded to the metal*

vibrations in figure 6). This low wavenumber region contains two vibrations that originate from the CO* intermediate, the stretch vibration (360 cm^{-1}) and the frustrated rotation vibration (280 cm^{-1}) (right and middle vibration in figure 6, respectively). In their paper, Roldan et al. found that the CO* coverage could be estimated via the ratio of these two peaks corresponding to CO in the lower wavenumber region. Nørskov et al. have published work on the CO* coverage of Cu(100), Cu(111), and Cu(211) and show that at the same overpotentials, the different facets have different binding energies for CO*, resulting in different CO* coverages[34].

Several spectroscopic studies have been published on the nature of the first intermediate of the eCO2RR, and how it correlates to the production of HCOOH or CO[25,26]. Since no further reduction is possible once HCOOH is formed as can be seen in Figure 4, it is important to steer the first intermediate away from HCOOH in order to form the hydrocarbons. In their work, Chernyshova et al. found that the conversion of CO_2 towards HCOOH follows a carboxylate intermediate, bound to the surface via carbon and oxygen[25]. Developing catalysts that inhibit this carboxylate intermediate and thus inhibit HCOOH production, will lead to an increase in selectivity towards the hydrocarbons. Despite several spectroscopic studies on the first intermediate and the CO* intermediate, spectroscopic studies on intermediates beyond CO* are lacking. In 2021, Moradzaman et al. published an *in-situ* Raman study on the surface state at different overpotentials using isotopic labeling[35]. They mention the presence of an unknown Cu-C species at eCO2RR relevant overpotentials (-0.6 to -1.4V). No further mentions on the exact nature of the species is given, but they correlate the species to catalyst deactivation. To the best of my knowledge, no other study has reported on this unknown species yet. Furthermore, there are no reports on spectroscopic evidence of intermediates beyond CO.

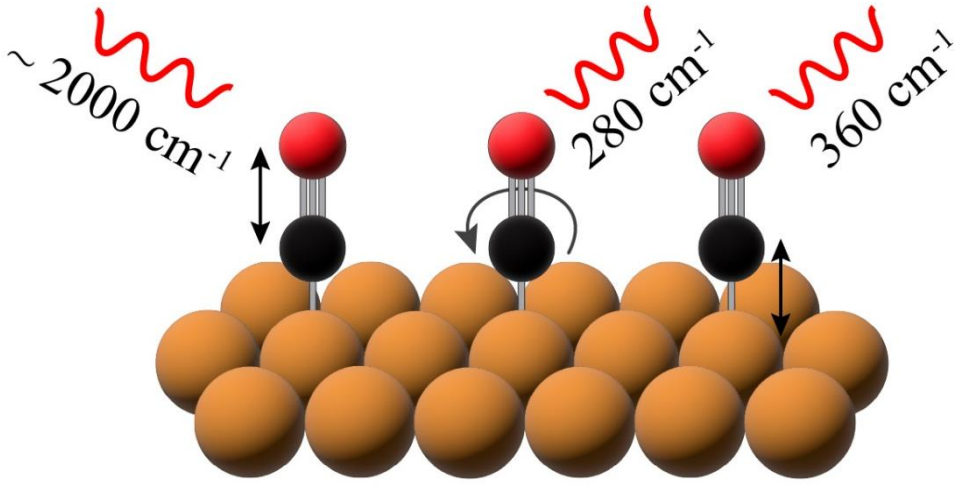

Figure 6: Vibration modes with their corresponding frequency (cm^{-1}) of linearly adsorbed CO on a Cu catalyst. Left vibration is the C-O stretch vibration which is visible at ~2000 cm^{-1}, the middle vibration is the Cu-CO frustrated rotation vibration at 280cm^{-1}, and the right vibration is the Cu-C stretch vibration at 360 cm^{-1}.*

Employing *in-situ* spectroscopic studies to elucidate reaction mechanisms is challenging. Unknown peaks in a spectrum, such as the Cu-C species found by Moradzaman et al., might originate from an intermediate, but determining the exact nature often proofs difficult. Isotopic labeling experiments can help proof the presence of a certain atom but tells nothing about the chemistry of the intermediate. Using a dynamic system that changes selectivity with potential or time can help finding out more about the nature of unknown species found in Raman spectra. Such an approach was used by An et al. to discover the reactivities of LFB-CO and HFB-CO[27]. Lower overpotentials (-0.7V) were characteristic for high CO F.E. and showed a strong signal of HFB-CO and a weak signal of LFB-CO. Increasing the overpotentials to higher values (-0.8V and -0.9V) showed a decrease in CO F.E. and an increase in ethylene F.E., together with a decrease in HFB-CO and an increase in LFB-CO. This led to their conclusion that HFB-CO is responsible for CO production and LFB-CO for C_{2+} production. Another important factor for Raman studies on reaction intermediates is the time resolution of the measurements, i.e. how long does it take to take one spectrum. As mentioned, the CO* intermediate is abundant on the surface and remains for longer periods of time as it is the RDS. However, intermediates beyond CO* often remain for shorter periods of time, making it hard to measure these species. Long acquisition times for one spectrum results in an averaging of everything on the surface and in a loss of dynamics, and thus the fast intermediates.

A recent, highly dynamic system with increasing interest is oxide-derived copper (ODC)[24,36,37]. ODC is found to possess initial increased catalytic activity and selectivity towards C_{2+} products, but also a quicker deactivation[38]. This initial increased performance is a result from a roughened surface due to the rapid removal of oxygen atoms, and from higher valent Cu atoms, such as Cu^{+} and $Cu^{\delta+}$ which arise from residual oxygen atoms after a reductive potential is applied[24] (Figure 7). There is however still a debate in literature about the presence of such residual oxygen atoms[24,39]. Some groups claim that all oxygen atoms are removed

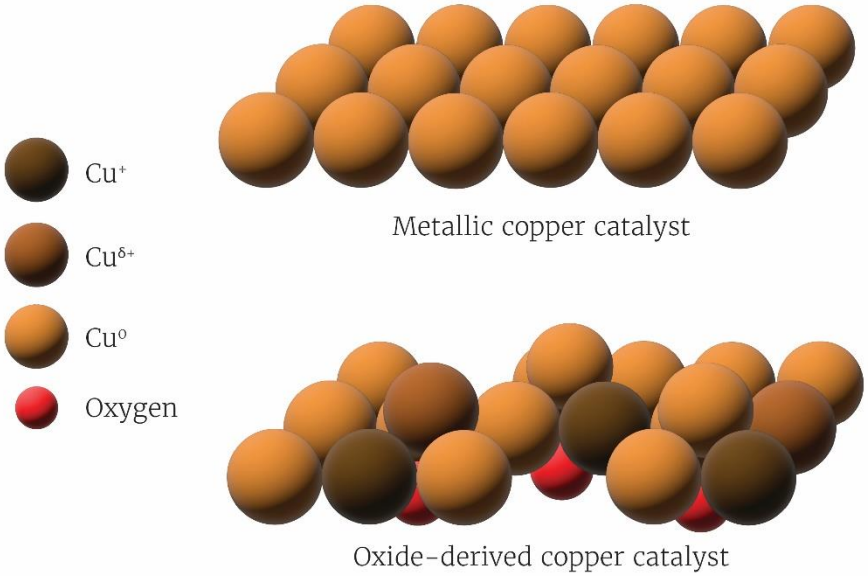

Figure 7: Schematic representation of a metallic copper catalyst and an ODC catalyst. The ODC catalyst possesses a roughened surface with residual oxygen atoms, resulting in higher valent copper atoms at the surface.

in a matter of minutes after a cathodic potential is applied[40,41], while others mention stable oxygen atoms for long periods of time[42,43]. Zhang et al. published a study on a ODC system with Cu_4O stoichiometry, that is stable at potentials up to -1.0V, making it relevant for C_2H_4 production[42]. Nevertheless, because of the initial increased performance and the quicker deactivation, ODC catalysts are ideal for studying the reaction mechanism of eCO2RR. As previously mentioned, the exposed facet also has a large influence on the catalytic performance. Combining this with the dynamic nature of ODC catalysts, a highly dynamic system can be created. By combining time-dependent activity and Raman measurements, simultaneous changes in selectivity and surface state can be correlated and could provide more insights into unknown species in Raman spectra.

In this thesis, well-defined Cu_2O sub-micro crystals are employed to study the reaction mechanism of the eCO2RR with the combination of time-dependent activity and Raman measurements. Three different morphologies of the catalyst are used: cubes with exposed facets of (100), octahedrons with (111), and truncated-octahedrons with a combination of (100) & (111) (Figure 8). As above-mentioned, the combination of ODC catalysts with different facets results in a highly dynamic system which is beneficial for studies on reaction mechanisms. First, the catalysts are obtained via a facile aqueous synthesis from a paper by Zhang et al. which provides accurate control over the exposed facets[44]. The structural properties of the catalysts are investigated with electron microscopy (EM) and X-Ray diffraction (XRD) and the electrochemical properties are studied with cyclic voltammetry (CV). Then, the catalysts are catalytically tested in an electrochemical H-cell, connected to a GC. First, their catalytic performance and its dependency on applied overpotential is investigated which showed an increasing selectivity towards the hydrocarbons at increasing potentials. Only small differences were found between the three catalysts at the higher overpotentials. Their catalytic performance was then studied in the time-domain which showed a dynamic behavior over time with an increase in CH_4 selectivity and decrease of C_2H_4 selectivity. To better understand this catalytic behavior, *in-situ* Raman measurements were employed. First, Raman measurements at different overpotentials (the reversible hydrogen electrode scale is used throughout this thesis) were performed to investigate the potential-dependency of the chemical surface state. An unknown vibration was found at the relevant potentials for CH_4 and C_2H_4 formation. Time-resolved Raman measurements at these overpotentials then showed a dynamic behavior of this vibration over time. Finally, a thorough discussion about this dynamic behavior is provided in which suggestions are made about the unknown vibrations in the Raman measurements and are coupled to the complex reaction mechanism behind the eCO2RR.

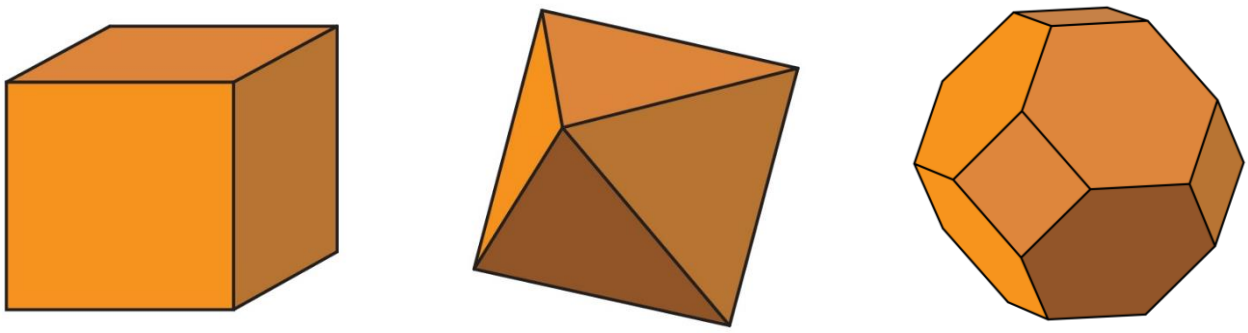

Figure 8: Schematics of left: Cu_2O cube, middle: octahedron, right: truncated-octahedron

2 THEORETICAL BACKGROUND

This chapter will provide some more theoretical background about the theories and principles behind the topics of this thesis. First, the principles of the eCO2RR are discussed, which will help with understanding certain phenomena that are observed in the experiments. Then, some theoretical background is provided about Raman spectroscopy. This will help to understand the Raman spectra that are recorded during this thesis and the discussions that follow.

2.1 Principles of Electrochemical CO_2 Reduction

As mentioned in the introduction, the eCO2RR is a redox half reaction with the general form shown in equation 4. The counter half reaction is often the oxygen evolution reaction (equation 5), where water is oxidized into oxygen, protons, and electrons.

$$x\mathrm{CO_2} + n\mathrm{H^+} + n\mathrm{e^-} \rightarrow \text{product} + y\mathrm{H_2O} \quad (4)$$
$$2\mathrm{H_2O} \rightarrow 4\mathrm{e^-} + 4\mathrm{H^+} + \mathrm{O_2} \quad (5)$$
$$\mathrm{H_2O} \rightarrow \mathrm{OH^-} + \mathrm{H^+} \quad (6)$$
$$\mathrm{Cu_2O} + 2\mathrm{e^-} + \mathrm{H_2O} \rightarrow 2\mathrm{Cu} + 2\mathrm{OH^-} \quad (7)$$

Table 1 shows the half reactions for the most common products of the eCO2RR on copper and the competing HER with its respective thermodynamic standard reduction potential E°[7]. The top part gives the half reactions where H^+(aq) is used as the protons source, whereas the bottom part gives the half reactions where H_2O is used as a proton source. The pH of the electrolyte largely determines whether H^+(aq) or H_2O is used as the proton source and will be discussed in more detail in section 2.1.2. The reactions with H_2O as the proton source are often more accurate than with H^+(aq) because of an alkaline environment near the surface of the catalyst, making it impossible for protons to be present. This alkaline environment is a result from two reactions happening at the surface, (1) the eCO2RR itself produces OH^- via the splitting of water as seen in equation 6 and (2) the reduction of Cu_2O into metallic Cu produces OH^- as can be seen by equation 7. The next subsections will discuss the most important parts of the eCO2RR in more detail.

Table 1: Reaction equations for the most common reaction products for the eCO2RR with their respective redox potentials E° (V_{SHE}) at pH=7.[7]

Reaction	E° (V_{SHE}, pH=7)
$CO_2 + 2H^+ + 2e^- \rightarrow HCOOH$	−0,61
$CO_2 + 2H^+ + 2e^- \rightarrow CO + H_2O$	−0,53
$CO_2 + 8H^+ + 8e^- \rightarrow CH_4 + 2H_2O$	−0,24
$2CO_2 + 12H^+ + 12e^- \rightarrow C_2H_4 + 4H_2O$	−0,35
$2CO_2 + 12H^+ + 12e^- \rightarrow C_2H_5OH + 3H_2O$	−0,33
$2H^+ + 2e^- \rightarrow H_2$	−0,42
$CO_2 + H_2O + 2e^- \rightarrow HCOO^- + OH^-$	−1,49
$CO_2 + H_2O + 2e^- \rightarrow CO + 2OH^-$	−1,35
$CO_2 + 6H_2O + 8e^- \rightarrow CH_4 + 8OH^-$	−1,07
$2CO_2 + 8H_2O + 12e^- \rightarrow C_2H_4 + 12OH^-$	−1,18
$2CO_2 + 9H_2O + 12e^- \rightarrow C_2H_5OH + 12OH^-$	−1,16

2.1.1 Electrochemical Cell Design

The design of the electrochemical cell has a large influence on the catalytic performance too as it can help minimize the kinetic barriers. One of the simpler electrochemical cell designs is the H-cell, which is illustrated in Figure 9a. The cell consists of two compartments, separated by a proton selective membrane. The membrane often consists of a Nafion polymer which is a sulfonated tetrafluoroethylene polymer which has a unique proton conduction ability[45]. The main purpose of this membrane is to block reactants and reaction products and to ensure that only protons pass through[8]. It also helps to stop dissolved platina or copper from the electrodes to deposit onto and possibly deactivate the other electrode. Each compartment contains one of the electrodes submerged in liquid electrolyte. CO_2 is purged through the working electrode compartment via the bottom and reduced at the surface of the catalyst. The gas products and the unreacted CO_2 then exit via the top and are analyzed by the method of choice, often gas chromatography (GC) or mass spectrometry (MS). A reference electrode is placed in the working electrode compartment to ensure a stable applied potential between the working and counter electrode. The H-cell is ideal for lab tests and studies on catalysts performance thanks to its simplicity. On the other hand, it lacks industrial applications as it is unable to reach industrially relevant current densities of ~200mA/cm^2 due to inherent mass transfer limitations[46]. These high current densities are required as it scales directly with rate of conversion, thus the overall production. The CO_2 that is purged through the bottom of the cell has to first reach the working electrode, where it then has to diffuse through the substrate material before it can be reduced on the catalyst.

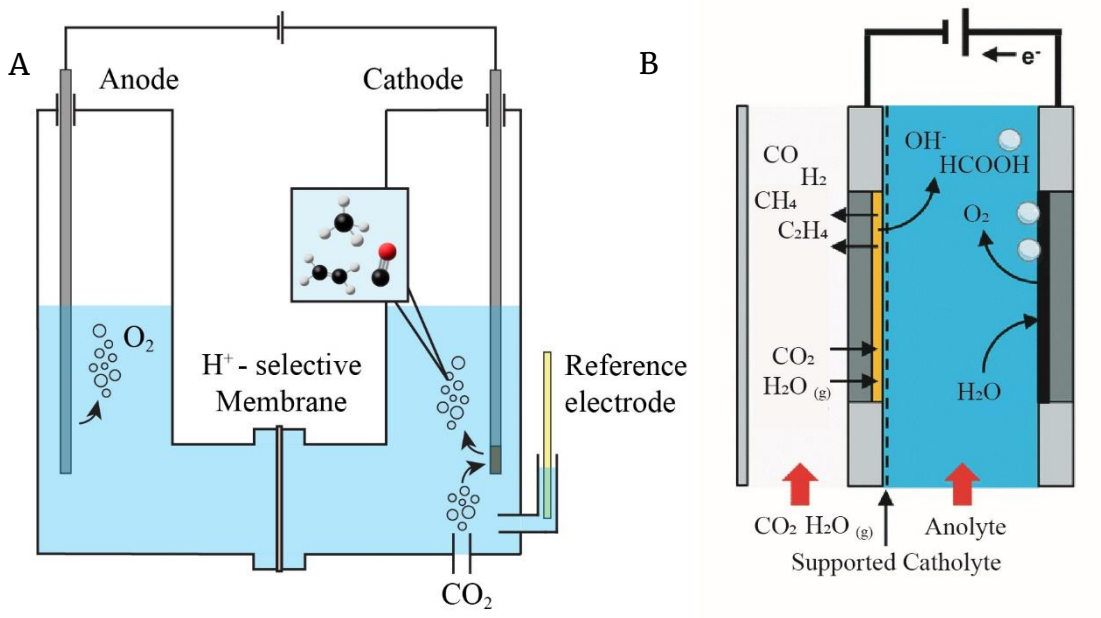

Figure 9: a: schematic of the electrochemical H-cell, consisting of two compartments: the anode and the cathode, separated with a proton-selective membrane. A reference electrode is added to the cathode side, and CO_2 is purged through the system from the bottom. b: schematic for the working electrode part of a GDE, consisting of a porous gas diffusion layer, a catalyst layer and the liquid anolyte. Gaseous CO_2 is purged through the gas diffusion layer circumventing the low solubility in water. Figure adapted from Burdyny et al. [48]

A newer cell design that becomes more popular and is able to reach industrially relevant current densities is the gas diffusion electrode cell (GDE) (Figure 9b)[47,48]. The principle of a GDE is the use of gaseous CO_2 instead of solubilized CO_2, overcoming the intrinsic drawbacks of aqueous systems that arise from the low solubility of CO_2. In Figure 9b you can see that the working electrode consists of a porous gas diffusion layer where CO_2 is purged through from the back. The catalyst is placed in between the gas diffusion layer and the electrolyte resulting in a three-phase boundary. The electrolyte is still necessary to close the electric circuit and for the transportation of reactants and liquid products. This design allows for current densities 10x higher than the H-cell as you overcome the mass transfer limitations of CO_2 in aqueous solutions.

2.1.2 The Electrolyte

The electrolyte is an important part of the electrochemical setup and for the eCO2RR in general[49]. It closes the electric circuit, and it allows for the transfer of the reactants. There are several types of electrolytes: organic solvents, solid electrolytes, or salt solutions, such as the 0,1M $KHCO_3$ electrolyte used in this work. Freshly prepared 0,1M $KHCO_3$ solution has a pH of ~8,3 as it is a weak base. After saturating the solution with CO_2, pushing the equilibrium more towards the right and thus increasing $[H^+]$ (see equation 8), the pH will decrease reaching a pH of ~6,8. In turn, the bicarbonate can dissociate into the carbonate ion (equation 9). Using a bicarbonate salt as the electrolyte helps with the intrinsic low solubility of CO_2 in water (0,076 mol L^{-1}, 273K, p = 1 atm)[50] by converting CO_2 into HCO_3^-, which can again dissociate into CO_2 [51].

$$CO_2 + H_2O \Leftrightarrow H^+ + HCO_3^- : pK_a = 6,35 \quad (8)$$
$$HCO_3^- \Leftrightarrow CO_3^{2-} + H^+ : pK_a = 10,33 \quad (9)$$

The pH of the electrolyte affects the eCO2RR in numerous ways. First of all, it affects the concentrations of the above-mentioned CO_2 and HCO_3^-, with higher concentrations of HCO_3^- in alkaline environments (equation 8). Furthermore, fresh CO_2 tends to form HCO_3^- when purged through alkaline solutions, affecting the CO_2 concentrations near the surface of the catalyst. Secondly, the pH determines the proton source for the eCO2RR as mentioned in section 2.1. The proton source in alkaline solutions is H_2O, whereas H^+(aq) is the proton source in acidic solutions[52]. The activation energies for creating H*, which is the active proton species in the eCO2RR, is different for H_2O and H^+, as can be seen in Figure 10, adapted from a study by Wang et al.[52]. The left graph shows the energy diagram for $H^+ + e^- \rightarrow H^*$ in acidic solution and the right for $H_2O + e^- \rightarrow OH^- + H^*$ in alkaline solution. It is clear that the activation barrier for H^+ is lower than for H_2O. Thus, proton-coupled reaction steps, which are dependent on H*, are dependent on the pH of the electrolyte. This leads to different dependencies on the pH for different products, such as C_2H_4 and CH_4, and this is the third effect of the pH. This difference for C_2H_4 and CH_4 was already discovered in the early work of Hori et al[19,13]. They found that the production of C_2H_4 is independent of the pH, whereas CH_4 is strongly dependent on the pH[19]. This also supports their statement that C_2H_4 and CH_4 follow different reaction pathways early on, which was mentioned in the introduction. This difference in pH dependency is caused by the involvement of a proton transfer in

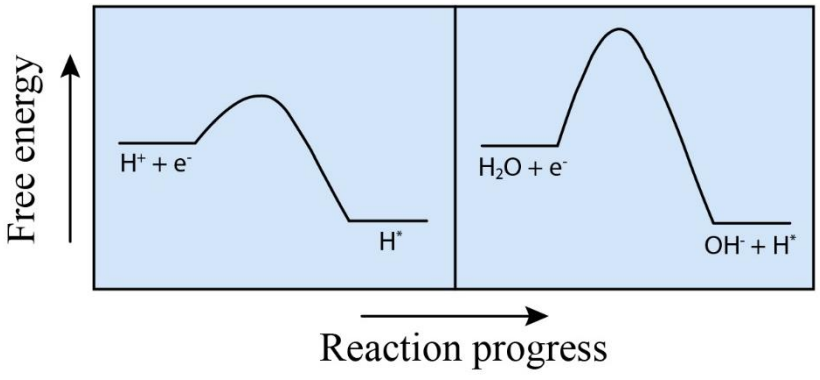

Figure 10: Free energy diagrams for the two possible ways to produce surface adsorbed hydrogen. The left diagram is in acidic solutions when H^+ is present, and the right diagram is in basic solution when no H^+ is present. The activation energy is significantly lower in acidic solutions. Figure adapted from Wang et al.[52].

the RDS for CH_4, which is not the case for the RDS for C_2H_4 (add RDS for both). Overall, the pH of the electrolyte is important for the eCO2RR as it affects both the activity and selectivity. However, controlling the pH is difficult due to the constant supply of OH^- from the surface of the catalyst.
[53,54]

Besides the pH, the cation of the electrolyte (e.g., K^+ or Na^+) also has a large influence on the catalyst's activity and selectivity, especially the size and the charge of the cation[55]. This is because there is always a layer of cations on the surface of the catalyst as the surface is negatively charged (cathode). This cation layer on a negatively charged surface is called the electric double layer. The most important parameters of the cations are the hydrated cation radius and ionic radius. The water molecules in the solvation shells of the cations are suggested to act as a hydrogen-source for the eCO2RR. However, a larger hydrated radius will lead to a stronger repulsion to the surface and decrease the cation concentration near the surface, which then leads to a decrease in the surface charge density. Furthermore, the positive charge of the cations can stabilize intermediate anions, altering the selectivity. The effect of different cations on the partial current to C_{2+} products for the Cu(111) and Cu(100) facets is shown in Figure 11. A decrease in the ionic radii and the solvation shell led to an increase of partial current, as the cation concentration increases, increasing the overall surface charge density.

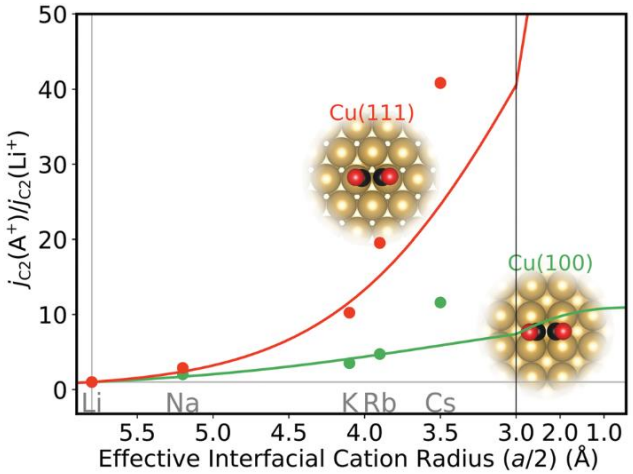

Figure 11: Partial current density towards C_{2+} products for different cations at the Cu(111) and Cu(100) surface. The dots represent theoretical data points and the line experimental data. Figure adapted from Ringe et al.[55]

2.1.3 Kinetic Barriers

From a thermodynamic point of view, the reactions in table 1 to the hydrocarbons are more favorable than to CO or H_2, according to the relation of Gibbs free energy (ΔG) to E°, found in table 1 (equation 10, where n is the number of electrons needed and F is the Faraday constant (96485,3 C mol^{-1})).

$$\Delta G = -nFE^{\circ} \qquad (10)$$

Figure 12 shows the free energy diagram of CO_2 to CH_4 on a Cu(211) surface at two different overpotentials, adapted from Nørskov et al[56]. This Figure also shows favorable thermodynamics for the formation of CH_4 as ΔG<0. However, in practice it is found that the hydrocarbons only become dominant at high overpotentials. This is because besides the thermodynamic effects, the eCO2RR experiences several kinetic barriers, which are depicted in Figure 12 & 13[7,8,57]. The first kinetic barrier is the large activation energy for several elementary reaction steps towards the hydrocarbons as seen in figure 12[58]. The difference in Gibbs free energy (ΔG) for the total reaction might be negative at both overpotentials, making the reaction thermodynamically favorable. However, slow kinetics are observed due to the large activation energies for some reaction steps. Especially large energy barriers early on, such as the further reduction of CO*, can result in the production of CO and prevent CH_4 formation. This makes that certain products such as CH_4 and C_2H_4 are only obtained at large overpotentials (>0,7V)[13,14], which also lowers the activation as can be seen in Figure 12. The second barrier is more of a diffusive barrier for the availability of reactants on the surface of the catalyst. First, as mentioned, many products require proton-coupled reaction steps and are thus dependent on the H* concentration on the surface. When the RDS of a product is a proton-coupled reaction step, such as CH_4, the lack of surface protons could prevent the formation of that product. Besides that, the HER is also competing for the same supply of H*, see Figure 13. Secondly, C_{2+} products are produced via C-C coupling, which requires two intermediate species, as CO*, to be in close proximity and thus a high coverage of these species[20], see Figure 13. A low surface coverage of these species can then again prevent the production of C_{2+} products.

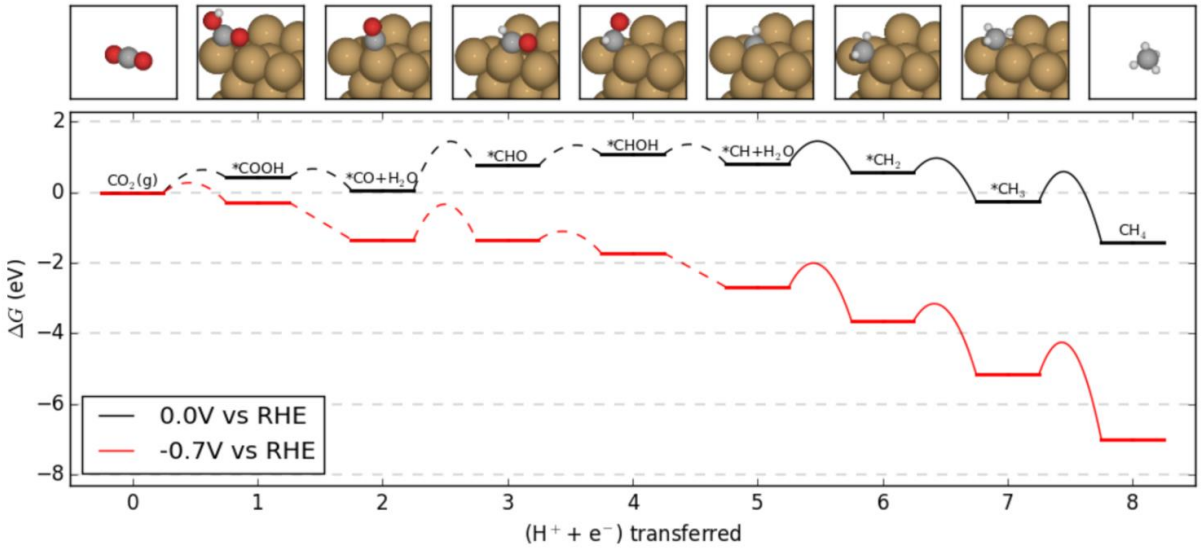

Figure 12: Calculated energy diagrams for the eCO2RR towards methane on the Cu(211) surface. Applying an overpotential lowers the overall ΔG and the energy barriers for each reaction step. Figure adapted from Nørskov et al. [58]

Furthermore, there is a mass transfer limitation for the CO_2 itself in the system. The low solubility of CO_2 in water can result in little CO_2 molecules reaching the surface. Besides the low solubility, the closer to the surface of the catalyst a CO_2 molecule gets, the higher the probability that it forms the bicarbonate ion due to the alkaline environment. This mass transfer limitation of CO_2 can negatively affect the CO* coverage if too little CO_2 molecules reach the surface.

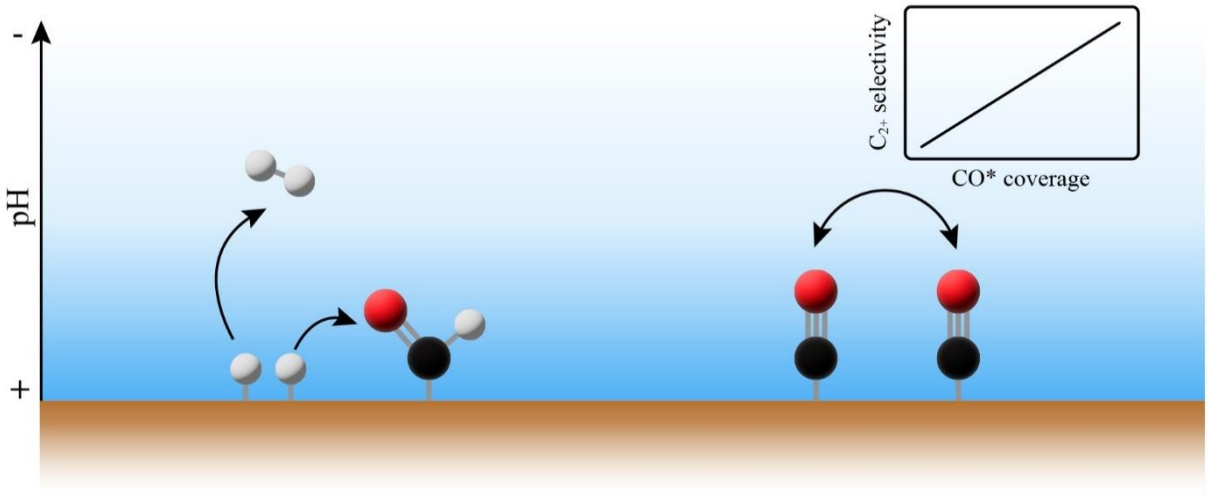

Figure 13: The two diffusive barriers that occur in the eCO2RR. Left visualizes the dependency on surface protons which are required in the proton-coupled reactions steps. Besides the eCO2RR, the surface protons are also used in the competing HER. The right visualizes the dependency on CO coverage, which is an important parameter for the production of C_{2+} products to form a C-C bond. Too low CO* coverage inhibits the C-C coupling and results in less C_{2+} production.*

2.2 Raman Spectroscopy

Raman spectroscopy is a form of vibrational spectroscopy, it measures molecular vibrations such as shown in Figure 14. Bonds in molecules vibrate and can be compared to springs, and the strength of the bond can be described by a simple spring as equation 11, where k is the force constant, x is the displacement and F is the force acting on the spring, or in this case, on the chemical bond[59]. The force constant k is the most important here, as it is characteristic for molecular bonds, a stiffer bond means a higher force constant.

$$F = -kx \qquad (11)$$

The energy of the respective vibration is related to the frequency and can be found with a solution to the Schrödinger equation and is given in equation 12, where v=0,1,2,… and ω is the frequency which is related to the force constant k and the effective mass μ (equation 13). The effective mass can be calculated with equation 14 for a system consisting of two masses.

$$E_v = (v \pm 0{,}5)\hbar\omega \qquad (12)$$

$$\omega = \sqrt{\frac{k}{\mu}} \qquad (13)$$

$$\mu = \frac{m_A m_B}{m_A + m_B} \qquad (14)$$

Equation 13 shows that with a higher force constant, or a stiffer chemical bond, the frequency of the vibration increases. You will often see the vibrational energies expressed in wavenumbers with unit cm^{-1}, which expresses the number of oscillations per cm (equation 15). Thus, a higher wavenumber in vibrational spectra means a stronger bond.

$$\tilde{\nu} = \frac{\omega}{2\pi c} \qquad (15)$$

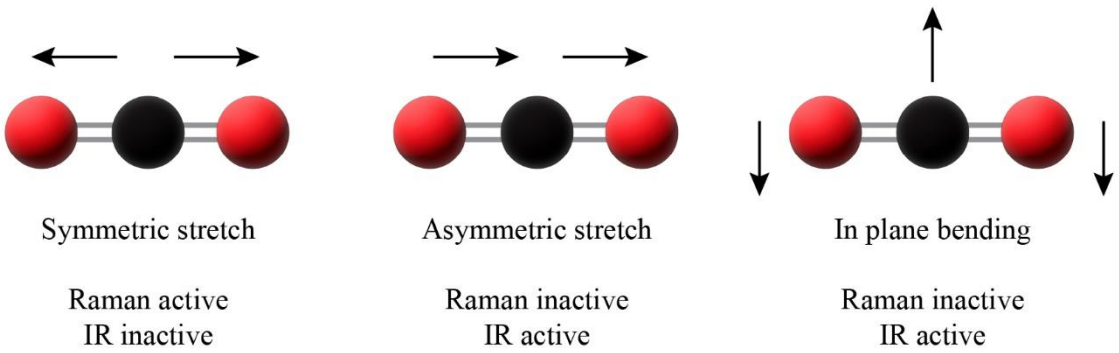

Figure 14: Different vibration modes for the symmetric CO_2 molecule, where Raman and IR are complementary to each other.

The title on the x-axis of a Raman spectrum is often Raman shift (cm^{-1}) instead of wavelength to indicate that the emitted light is energy-shifted in comparison to the light source. The light source of Raman spectrometers are intense monochromatic lasers. This is different to an IR spectrum as that measures the absorption of IR light by molecular vibrations. The working principle of Raman is schematically visualized in Figure 15. Here you see that most of the light does not change energy and only undergoes elastic scattering, this is called Rayleigh scattering. Part of the incoming light undergoes inelastic scattering and induces a vibration, which excites the molecule to a higher virtual state from where it falls back into a real vibrational energy level that is higher than the ground state. This emits a photon with lower energy than the initial incoming photon, which is called a Stokes shift. Since Raman scattering is inelastic, the probability is intrinsically low. According to the Boltzmann distribution, there is always a small part of the molecule already in a thermally excited state, depending on the temperature[60]. This is possible as the energy levels are close in energy and kT is enough energy to excite molecules to these thermally excited levels. Molecules in a thermally excited state will cause anti-Stokes shifts, leading to emitted photons with a higher energy than the initial incoming light. However, since the fraction of molecules in the higher excited state is generally small at room temperature, the intensity of anti-stokes light is also low compared to Stokes scattering.

How many vibrations a molecule has depends on the number of atoms and the symmetry of the molecule. Linear molecules have 3N-5 vibration modes, where N is the number of atoms, and nonlinear molecules have 3N-6 vibration modes. Not all vibrations are Raman or IR active; vibrations that cause a change in the electric dipole moment are IR active, whereas vibrations that cause a change in the polarizability, which describes the ability to polarize a bond (i.e.: move the electrons in the bond), are Raman active. If the molecule also has a center of inversion, such as the CO_2 molecule in Figure 14, then IR and Raman are complementary to each other; IR active vibrations are not Raman active and vice versa. The symmetric stretch vibration of CO_2 as depicted in Figure 14, is Raman active and IR inactive as it does not change the electric dipole moment, but it does change the polarizability of the molecule. The asymmetric stretch and in plane bending vibrations do change the electric dipole moment and are thus IR active and Raman inactive.

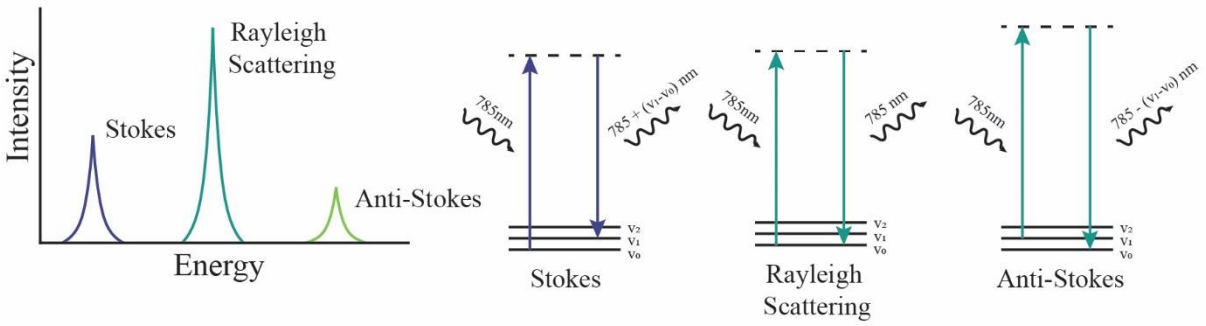

Figure 15: Working principle of Raman spectroscopy. Most of the incoming light gets elastically scattered, resulting in Rayleigh scattering. Some of the incoming light gets inelastically scattered, resulting in an energy shift (stokes or anti-stokes shift).

A disadvantage of Raman spectroscopy over IR spectroscopy is due to the selection rules of Raman. As stated, a vibration is Raman active if it causes a change in the polarizability. Apolar bonds are easy to polarize because the electrons are evenly divided over the bond and not strongly bound to one part, thus, moving the electrons is easy. Polar bonds on the other hand have their electron density concentrated on one part of the bond because of high electronegativity, resulting in a low polarizability of these bonds. This makes that polar bonds are often invisible to Raman spectroscopy. At the same time, this is also an advantage for *in-situ* measurements in aqueous solutions, as water is invisible in Raman due to its polarity. Another advantage of Raman over IR spectroscopy is the ability to measure in the lower wavenumber region (200-500 cm^{-1}). Based on fundamental vibrational spectroscopy theory, IR should be able to measure in this lower region, but IR spectrometers often lack optics for the low wavenumber light such as lenses and light sources[61]. This lower wavenumber region is important for *in-situ* measurements of the eCO2RR as metal-intermediate bonds typically vibrate at low energies.

2.2.1 Surface Enhanced Raman Spectroscopy (SERS)

Raman spectroscopy itself often suffers from low scattering cross sections, resulting in very little signal[62]. This is not a problem when measuring a powder, but it does become a problem when one wants to measure intermediate species *in-situ*, as you need long acquisition times to obtain enough signal. However, a special phenomenon called surface enhancement was found in the 1970s which enhances the Raman signal significantly on certain surfaces. A 10^6-fold enhancement was found when measuring adsorbed pyridine molecules at a silver surface[63]. This phenomenon was long poorly understood, and at the time it was only divided into two mechanisms: (1) electromagnetic enhancement and (2) chemical enhancement. Since the electromagnetic enhancement accounts for a 10^4-fold enhancement, only this mechanism will be briefly explained in this thesis.

The electromagnetic enhancement occurs when an electromagnetic wave interacts with a metal surface. When observing the electromagnetic fields at the surface of the metal, there is a strong enhancement when compared to the far field. This happens because the electromagnetic waves may resonate and excite localized surface plasmons (collective oscillations of electrons), resulting in an amplification of the electromagnetic fields. Resonance can occur here because the collective oscillations of electrons, which carry a charge, will induce an electromagnetic field itself. This enhancement is not only for the incident fields, but is also possible for the scattered fields, which contains the Raman scattering. The local surface plasmon resonance (LSPR) only happens when the frequency of the incident light is in resonance with the frequency of the plasmon resonance in the metal structure (Figure 16). The then scattered Raman intensity scales linearly with the incident field intensity (i.e. your laser power). The strength of the enhancement also depends on the distance of the adsorbates to the metal surface, and scales with r^{-10}. This is a strong distance dependency; this will however not be a problem for small, adsorbed intermediates. It will only become problematic when you want to measure large biological samples for example. When choosing the optimum frequency of the incident light source, the models predict that it must coincide with the LSPR, resulting in maximum resonance and thus enhancement. This is however

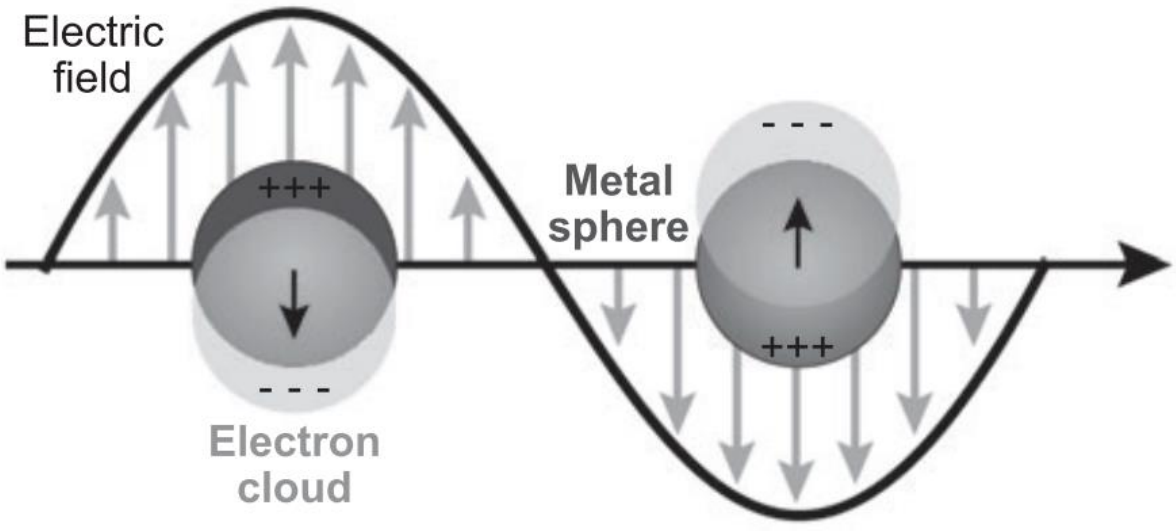

Figure 16: Schematic representation of the resonance of incoming light with the plasmon vibration, resulting in an increase of the electromagnetic field

not the case in practice. Raman scattering is always energy-shifted in comparison to the incident light source, so, to also enhance the Raman scattering effectively, the frequency of the light source should be adjusted accordingly to maximally enhance the LSPR and the Raman scattering. It was found that the maximum SERS enhancement occurred when the light source frequency is higher in energy than the maximum of the LSPR extinction spectrum. The maximum of the LSPR extinction spectrum tells you what the best frequency is for enhancing the LSPR.

The requirement for a substrate that supports SERS, is the presence of surface plasmons. Most of the research on SERS has been conducted on Au, Ag, and Cu as they have plasmons in the visible light region. This is very convenient for *in-situ* Raman studies on the eCO2RR, as the most widely studied metal is Cu, which is also the used metal in this thesis. Conducting *in-situ* Raman studies on metals without plasmons such as Ni is harder because of the absence of plasmons in the visible light region.

3 METHODOLOGIES

This chapter describes the methods that are used throughout the thesis. First, the synthesis of the Cu_2O sub-microcrystals is given after which the preparation methods for the electrodes is discussed. Then the characterization methods of choice are described followed by the method of the catalytic testing and calculating the F.E.. Finally, the methods for the Raman measurements together with the specially designed *in-situ* Raman cell are discussed.

The following chemicals were purchased from Sigma-Aldrich: polyvinylpyrrolidone (Mw=29000), l-ascorbic acid (99%), sodium hydroxide (pellets, ≥98%), and copper(II) chloride anhydrous (>98%). Ultrapure water was retrieved via a Direct-Q® 3 UV water purification system.

3.1 Synthesis

A procedure by Zhang et al., published in 2009 was used to synthesize the catalyst particles[44]. This is a colloidal synthesis with easy control over the exposed facets of the particles by adding various amounts of the stabilizing agent polyvinylpyrrolidone (PVP). Without PVP, the particles grow as well-defined cubes with the exposed facet being $Cu_2O(100)$. With increasing amounts of PVP, which stabilizes the (111) facet, the particles transition into octahedrons. By playing with the amount of added PVP, high control over the exposed facets can be achieved.

In a typical synthesis, 135.0 mg of $CuCl_2$ was added to a 250 mL round bottom flask with stirrer and dissolved in 80 mL of ultrapure H_2O. This mixture was heated with a water bath set to 55 °C under stirring. Upon reaching this temperature, PVP powder was directly added if needed. For the octahedrons, 3.0 g of PVP was added, and 1.0 g was added for the truncated-octahedrons. The cubes did not use PVP. After everything was dissolved, 10 mL of 2.0 M NaOH was slowly added over the course of 10 minutes. A color change is observed from light blue to brown, and this is set to react for 30 minutes. After 30 minutes, 10mL 0.6 M of the reducing agent l-ascorbic acid solution was added to the mixture also over the course of 10 minutes. This mixture was set to react for 3 hours in which a color change from dark brown to a brick-red color is observed. The reaction mixture was then centrifuged for 2 minutes at 3000 rpm and the supernatant was discarded. The remaining particles were washed three times with a 1:1 ethanol:water mixture and stored in 10mL of pure ethanol.

Table 2: amount of chemicals used for the synthesis of all three different catalyst shapes.

Sample	$CuCl_2$ (mg)	PVP (g)	2M NaOH (mL)	0,6M l-ascorbic acid (mL)
Cubes	135.0	0	10.0	10.0
Octahedrons	135.0	3.0	10.0	10.0
T-octahedrons	135.0	1.0	10.0	10.0

3.2 Electrode preparations

Two different substrate materials have been used to prepare the electrodes, carbon paper and glassy carbon. TGP-H 060 carbon paper is used and is cut into pieces of 1x2cm. The cut carbon papers are then treated overnight in an aqua regia solution and afterwards washed 5 times with ultrapure water and twice with ethanol. After washing, the carbon papers are dried in an oven set to 60 °C. To prepare the carbon paper electrode (CPE), the carbon paper is placed horizontally in a clamp and the catalyst is drop casted in amounts of 10µL with a finnpipette, directly from the ethanol suspension. After each 20µL added, the electrode was let to dry. This was typically repeated until ~0,4mg of catalyst was added per cm^2 and the electrode was dried thoroughly.

The glassy carbon electrodes (GCE) were all cut to a size of 1x1cm, and they were polished using Al_2O_3 powder. After polishing, they were transferred into a small flask together with a mixture of ethanol, acetone and water in ratio 1:1:2. The flask was then sonicated for ~10 minutes and the glassy carbon was washed with ultrapure water afterwards. The catalyst was then added directly from the ethanol suspension on top of the dry glassy carbon. After the GCE was dry, they were transferred to a Ossila UV Ozone Cleaner to get rid of any residual ethanol or ligands. A typical electrode had ~80µL of the catalyst suspension. After each experiment, the glassy carbon was cleaned with a wet wipe and polished and cleaned again.

3.3 Characterization

The main methods for structure characterization of the catalysts were X-Ray diffraction (XRD) and electron microscopy (EM). XRD measurements were performed on a Bruker-AXS D2 Phaser powder X-ray diffractometer equipped with a cobalt source ($K_{\alpha1,2}$, λ = 1.79026 Å) and a divergence slit of 1.0mm. A typical diffractogram was taken in the 20°-100° 2θ range with an increment of 0.02° 2θ, a time per step of 0,4s and a rotational speed of 15°/s. The sample was prepared by dropcasting the catalyst directly from the ethanol suspension onto a special zero-background silicon wafer to reduce background noise. The ethanol was slowly evaporated to air and nothing else was done for the sample preparation.

High-resolution SEM measurements were performed on a FEI Helios Nanolab G3 at an electron energy of 5.0 kV and a probe current of 0.2 nA. Samples were prepared by first drying some catalyst powder and adding it onto an aluminum SEM stub with a carbon sticker. This sample was then coated with a gold layer of 6-8nm thick. Low-resolution SEM measurements were performed on the PhenomProX desktop SEM at 10-15 kV. The sample preparation is identical to the samples for the high-resolution SEM without the gold layer.

Cyclic voltammograms (CV) were recorded on an Ivium Technologies CompactStat.h. The measurements were performed in the electrochemical H-cell equipped with a CPE and the potential ranging from -1.4 V to 1.6 V. 15 cycles were recorded at a speed of 50mV/s and a step-size of 10mV.

3.4 Catalytic Testing

Catalytic tests were performed using an H-cell with a CPE connected to a GAS CompactGC 4.0 gas chromatograph equipped with two thermal conductivity detectors and two flame ionization detectors. A picture of the setup is shown in figure 30 in appendix A. All the CPE's had ~0.4 mg of the catalyst drop casted on ~1cm^2 of the carbon paper, and no further treatment was applied to the working electrode. The counter electrode consisted of a platina mesh, and the two electrode compartments were separated with a piece of Nafion membrane. CO_2 and krypton gas are both bubbled into the working electrode compartment with a flow rate of 10 mL/min and 0.2 mL/min, respectively. The krypton is used as an internal standard hydrogen. A magnetic stirrer and an Ag/AgCl reference electrode were added to the working electrode compartment, and both compartments were filled with CO_2-satured 0.1 M $KHCO_3$ electrolyte (pH = 6.8). It was also necessary to make the working electrode part airtight in order to not let any product gas escape. After closing the whole system, everything was connected to an Ivium Technologies potentiostat, and the GC was connected to the top of the working electrode side.

The F.E. for the gas products were then calculated with the data of the GC, and liquid products were examined with H-NMR and could only be detected after the catalytic run was over. The formula to calculate the F.E. is given in equation 16.

$$F.E. = \frac{C_x \times Q \times F \times n_x}{A \times V_M \times j \times 10^6} \times 100\% \qquad (16)$$

Here

C	=	concentration of product x (ppm)
Q	=	flow of CO_2 (s^{-1})
F	=	Faradaic constant (C mol^{-1})
n	=	number of electrons transferred for product x
A	=	area of the electrode (cm^2)
V_M	=	molar volume (24,0 mL mol^{-1})
j	=	current density (A cm^{-2})

3.5 Raman Measurements

All the Raman measurements were performed on a Renishaw® inVia confocal Raman microscope equipped with a 785 nm laser. For the *in-situ* measurements, a Nikon 40X, 0.80 NA water immersion objective was used, and the system was connected to an Metrohm Autolab PGSTAT101 potentiostat. A special electrochemical cell was designed for the *in-situ* measurements (Figure 17). The design allows for the Raman objective to be submerged into the electrolyte during the reaction. The working electrode for the *in-situ* Raman measurements was a GCE, prepared as described in section 3.2. The GCE is placed on a gold pin connecter in the middle of the cell and held in place with a plastic slide. Just as the catalytic tests, CO_2-saturated 0.1M $KHCO_3$ is used as the electrolyte and is added directly into the cell, submerging the working electrode. A typical Raman spectrum was recorded in the 200-3200 cm^{-1} range with the laser power set to 2,3 mW and an acquisition time of 2 s. All the *in-situ* Raman spectra were baseline corrected with the SNIP algorithm to create a smooth baseline and get rid of the sporadic fluorescence from the particles[64].

Regular ex-situ Raman measurements on powder were performed with a 50X, 0.50 NA objective. The spectra were also taken in the 200-3200 cm^{-1} range and with the laser power set to 2.3 mW, but now with higher acquisition times, depending on the amount of signal from the samples.

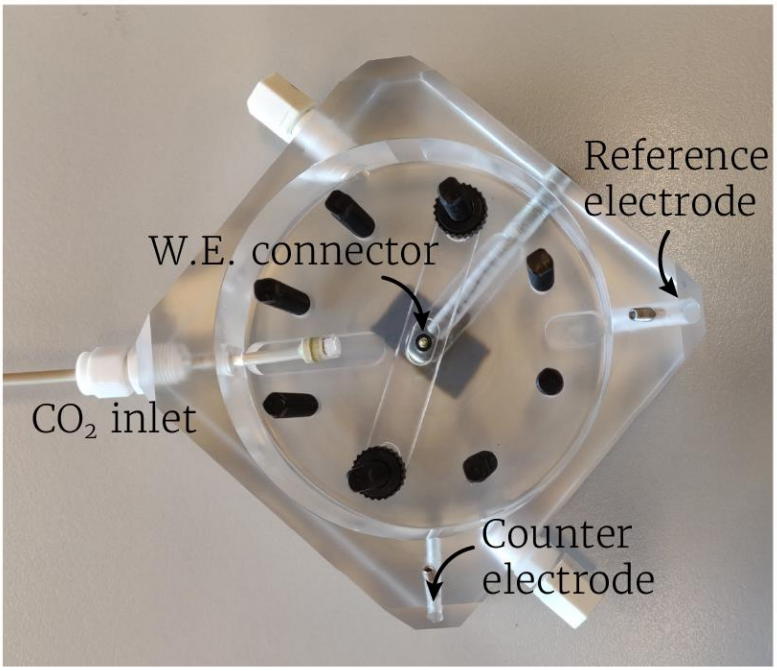

Figure 17: Picture of the designed in-situ Raman cell with its components.

4 RESULTS

This chapter will provide the results of the conducted experiments and discuss them. All the experiments were performed on copper-oxide sub-microcrystals with varying shapes, which were obtained via the facile aqueous synthesis as described in section 3.1. First, the results of the synthesis and the material characteristics are discussed followed by the catalytic properties of the catalysts. The general catalytic properties are be discussed, after which the time-dependent catalytic behavior is provided and discussed. Then, the results of the Raman measurements are discussed with first potential-dependent measurements to understand the system we are looking at. Lastly, the time-dependent Raman measurements are discussed together with the results from the time-dependent activity measurements. This combination has proven to be beneficial to explain trends in catalytic behavior, which can then be correlated to the reaction mechanism behind the eCO2RR.

4.1 Material Characteristics

First, the morphologies of the as-synthesized catalyst particles were characterized with high-resolution SEM and the results are shown in Figure 18. From these images it is clear that the particles exhibit the intended shapes from cubes to octahedrons. The synthesis without PVP produced well-defined cubic particles whereas the syntheses with increasing amounts of PVP start to truncate the cubes, eventually into well-defined octahedrons. As the particles are not spherical, comparing the sizes is difficult as the length differs with position. The size of the cubes and octahedrons were measured along their edge from the SEM images, as all edges have an equal length, and were 510±58 nm & 548±59 nm, respectively, with N=100. The truncated-octahedrons do not have a constant length edge, which makes it impossible to give an accurate size distribution.

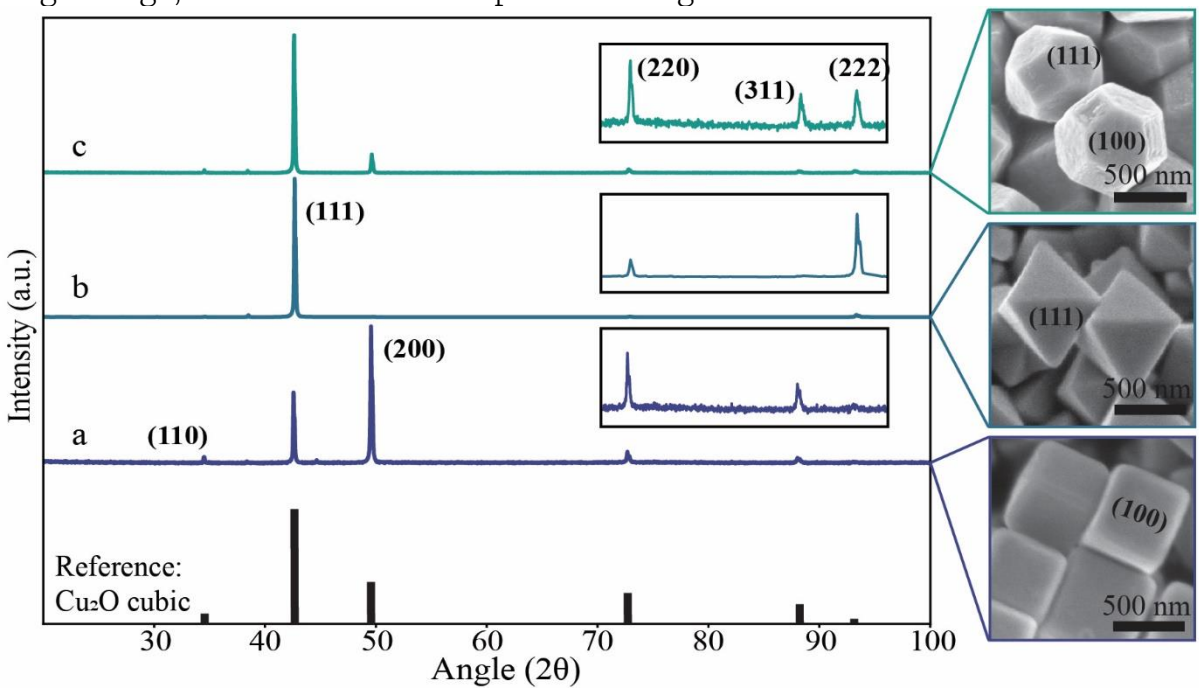

Figure 18: High-resolution SEM images of all three catalysts with their respective X-ray diffractograms and a reference diffractogram for Cu_2O.

However, from the scale bar in Figure 18, it is clear that the size is similar to the cubes and octahedrons. Zoomed out SEM images of all three catalysts are shown in figure 32 in appendix A which shows homogeneity in the particle size and shape. To further investigate the crystal structure and phase of the particles, XRD measurements were performed.

Figure 18 also shows the X-ray diffractograms of the three different Cu_2O particles. All three particles show the cubic phase, according to the reference diffractogram. The difference in morphology of the particles is also visible in the diffractograms via the peak ratio of Cu(111) to Cu(200) ((111)/(200)). This ratio is the largest for the octahedrons, as they mainly exhibit the (111) facet. The cubes have the lowest (111)/(200) ratio and the truncated-octahedrons have a ratio that is in between the cubes and the octahedrons. Besides the difference in the (111) & (200) peaks, the particles also show differences in the high angle region for the (220), (311) & (222) peaks. Here you can see that the octahedrons possess a strong (222) peak which is absent for the cubes, and the cubes possess the (311) peak which is absent for the octahedrons. The (222) facet has the same crystal orientation as the (111) facet, but with half the length, which is why its intensity is higher for the octahedrons than for the cubes, just as the (111) peak. The truncated-octahedrons show an average of the cubes and octahedrons and possess both the (222) and (311) facet. The as-synthesized particles thus exhibit the cube morphology with the (100) exposed facet, the octahedron morphology with the (111) facet and the truncated-octahedron morphology with a combination of the (100) and (111) facet, as evidenced by SEM and XRD.

Next, the electrochemical properties of the particles were investigated by recording CVs. CVs provide information about at what potentials a chemical reaction takes place by recording the current over a potential-window. A sudden increase in current means a chemical transition/reaction occurs at that potential.

The CVs were recorded in an H-cell with a CPE containing ~0.4mg catalyst per cm^2 in CO_2-saturated 0.1M $KHCO_3$ (pH = 6.8) with a constant CO_2 flow of 10 mL min^{-1}. The cyclic voltammograms (CVs) for the Cu_2O cubes and octahedrons are shown in Figure 19. The CVs are very similar for both catalysts, which is to be expected as they consist of the same material. There is however a small difference in exact position of the reduction and oxidation peak between the catalysts which is more pronounced for the reduction peak. The reduction peak for the cubes is at a slightly higher potential than for the octahedrons, which might indicate that the reduction of the (100) facet is easier than the (111) facet. The distinct reduction and oxidation areas are present in both CVs at 0.1V and 0.7V, respectively. As the copper in Cu_2O has a valence state of +1, there is only one reduction peak and one oxidation peak. However, copper can also have a valence state of +2, but there is no distinct second oxidation or reduction peak visible in this CV. Roldan et al. published a work where they also used a Cu_2O electrocatalyst for the eCO2RR. Their recorded CVs do show two distinct reduction and oxidation peaks, ours not. Reduction peaks are found at 0.4V & 0.1V, and oxidation peaks at 0.5V & 0.8V in their data. The oxidation peak in our CV stretches from 0.5V – 0.9V, which would mean that if there is a second oxidation peak, it might be underneath the larger peak. Our CV also shows a reduction peak at 0.1V, but no second reduction peak at 0,4V. As the presence of a second oxidation peak cannot be proven, and there is no second reduction peak,

it might suggest that our catalyst cannot be converted into the +2 state in this system.

After the oxidation of copper at 0.9V, the current starts to increase into the anodic direction. As this is not at overpotentials relevant to the eCO2RR, the increase in caused by the OER, now happening at the copper electrode instead of the counter platina electrode[65]. After the reduction of copper-oxide at 0,1V, there is first a plateau in current till around -0.2V, after which it also starts increasing. This is the onset potential for the eCO2RR (and the HER), which is the potential at which the reaction starts. The exact onset potential for the eCO2RR depends on your system, and onset potentials of -0.1V have been reported in literature on an ODC catalyst[36]. If we look at the early work of Hori (Figure 3 in the introduction), there is an onset potential of -0.4V for the eCO2RR[13]. However, at -0.4V, only small amounts of CO and HCOOH are being produced and the HER is dominant. Increasing the overpotential further into the cathodic direction, the current density keeps increasing as can be seen in Figure 19, and new products which require more electrons (>2e$^-$), as C_2H_4 and CH_4, start to being produced and even dominate at -0.9V (Figure 3).

Catalytic activity measurements were then performed on the catalysts to further look into the selectivity at the overpotentials relevant to the eCO2RR, and the results are discussed in the next section.

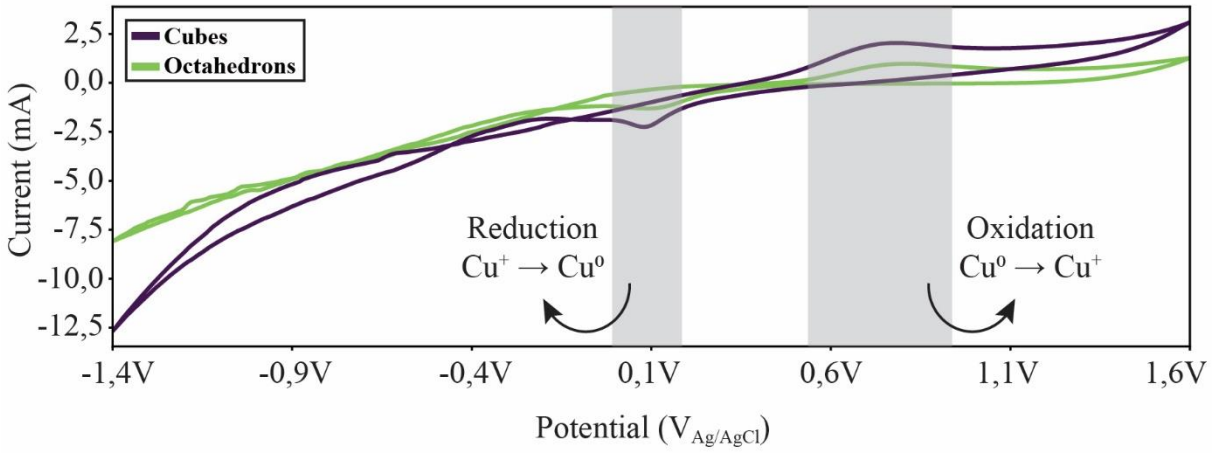

Figure 19: Recorded CVs for the Cu_2O cubes and octahedrons from -1,4V to 1,6V. Both catalysts show a distinct reduction and oxidation area.

4.2 Catalytic Performance

The catalytic selectivity is highly dependent on the applied overpotential[8,13,52], and the activity of the three catalysts were analyzed at -1.2V and -1.4V. For copper catalysts, -1.0V is generally seen as the ideal overpotential for C_2H_4 production[8,13]. However, our system consists of copper-oxide, which is often found to possess a higher optimal overpotential for C_2H_4 production[66]. Activity measurements at -1.0V with our system displayed F.E.'s for ethylene of <5% (figure 31 in appendix A), so higher overpotentials were chosen. The measurements were performed in an electrochemical H-cell, and a picture of the setup is shown in Figure 30 in appendix A.

Nevertheless, the results of the activity measurements are shown in Figure 20. The left Figure is the average F.E. for the gas products for the first 30 minutes, and the right Figure is the average F.E. for all products, including the liquid product HCOOH, over the entire experiment. In general, the selectivity for the gas products of all three catalysts at the same overpotential does not display significant differences, similar to a previously reported study on these catalysts[17]. This suggests that the different facets in general do not possess large difference in catalytic performance, in contrary to their metallic counterparts, where Cu(100) and Cu(111) do possess large differences in catalytic performance. Another possibility is that the catalysts possess similar surface structures under working conditions. For this, post-catalytic SEM and XRD were measured to investigate the post-catalytic structure, and they will be discussed in the next section. At -1.2V, CO is the dominant product with a F.E. of 25-30% for all three catalysts, followed up by C_2H_4 with a F.E. for the cubes of 12%, the octahedrons of 8% and the truncated-octahedrons of 14%. This is in line with the other study on these catalysts where the octahedrons also possessed the lowest F.E. for C_2H_4 and the truncated-octahedrons the highest. Furthermore, the F.E. for CH_4 is only ~1% for all three catalysts at -1.2V. The selectivity changes and the differences between the catalysts grow when the potential is increased to -1.4V, where CO is decreased to

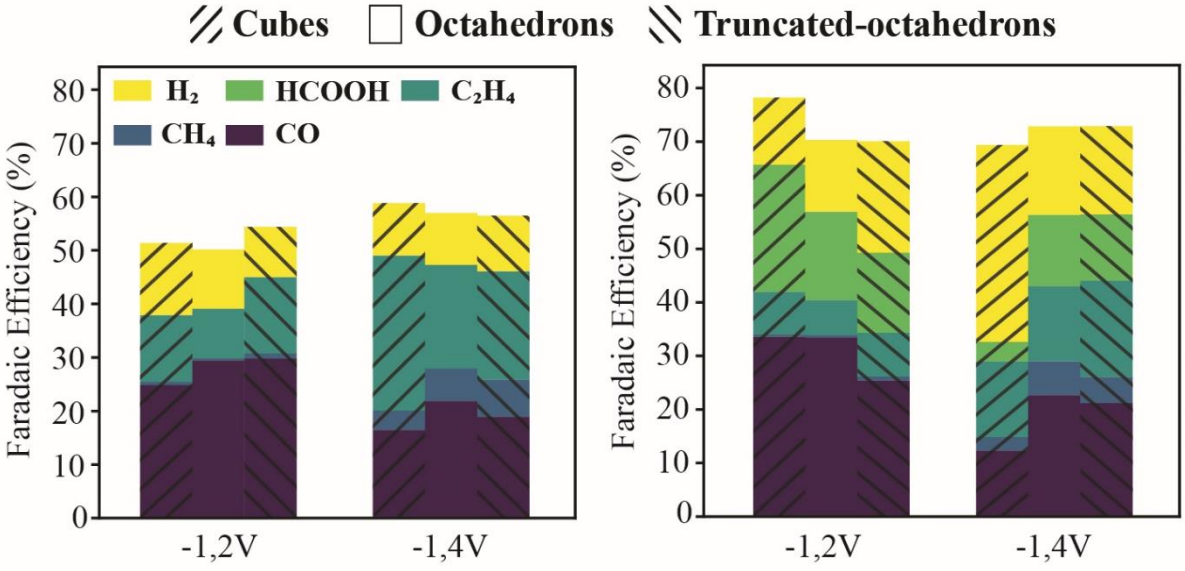

Figure 20: Left: average catalytic performance for all three catalysts at -1,2V and -1,4V over 30 minutes. Only the gas products has been plotted here. Right: overall catalytic performance for all three catalysts as the same overpotentials, now also with HCOOH added.

16-22% and C_2H_4 is now the dominant product with a F.E. of 29% for the cubes and 20% for the octahedrons and truncated-octahedrons. Also, CH_4 is now being produced in more significant amounts with the highest F.E. of 6% for the truncated-octahedrons and the lowest for the cubes with 4%. At this potential, the competing HER is also more suppressed. The cubes are now the best catalyst for the production of C_2H_4 (F.E. 29%) which was not the case in the previously reported study on these catalysts[17]. There, they found the highest F.E. of C_2H_4 for the truncated-octahedrons with 59% at an overpotential of -1.1V. However, they used 0.5 M CO_2-saturated $KHCO_3$ as the electrolyte, instead of 0.1 M which was used in this thesis. They do not show a picture or detailed schematic of their electrochemical setup , but they reach current densities of >30 mA cm^{-2} at -1.1 V while our system was unable to reach 10 mA cm^{-2} at -1.4 V, indicating that their system is significantly different than ours. Nevertheless, our activity measurements show similarities with other trends found in literature, where increasing overpotentials show decreased production of the lower reduced species (e.g. CO) and H_2, and an increased production of the higher reduced species (C_2H_4 & CH_4)[8]. The onset potential for C_2H_4 is also lower than for CH_4, which is also often seen in literature.

The liquid products could not be analyzed during the reaction, such as the gas products, since it is analyzed afterwards with NMR. Furthermore, the experiments were not conducted in the same time span, with some running overnight, which gives rise to two problems. First, it is hard to compare the catalysts as the selectivity changes over time, as will be seen in section 4.4. This change is not equally distributed over the products, where some products decrease and others increase over time. The second problem is a slow malfunctioning of the whole system, where the potentiostat cannot apply the set overpotential, resulting in a slow decrease of overpotential and current. Figure 21 shows the current, overpotential and F.E. over time for the duplo experiment on the truncated-octahedrons at -1.2V. The red line indicates where the malfunctioning happens with a sudden decrease in current, overpotential and F.E.. This malfunctioning was unavoidable and the exact time it occurs seemed to be dependent on the set overpotential; higher overpotentials caused an earlier malfunctioning. The corresponding F.E. shows that after the malfunctioning occurs, there is still production of the lower reduced species, H_2 and CO, but no C_2H_4 and CH_4. The reason for the malfunctioning is still unclear, but since the applied potential also decreases, it is most likely not due to a deactivation of the catalyst. These two problems make it hard to accurately compare the complete F.E. with HCOOH for the catalysts.

Another thing to notice is that the F.E. does not add up to 100% in the Figure with liquid products. This suggests that there are still some other products that are not added. Some products that are often added in literature that are not added here are ethanol, acetate and 1-propanol[8]. However, since these are liquid products and usually have a low F.E. (<5%), they are often not visible in NMR spectra due to a too low concentration. However, there is a deficit of 20-30%, and the cumulative F.E. of the above-mentioned products never add up to 20-30% in literature. Since this system consists of ODC catalysts, some current also goes into the reduction of the copper-oxide. However, as can be seen from figure 21, the time span of the experiment is in the order of hours. If the reduction of the copper-oxide only

happens once at the start of the experiment, you would not expect that ~20% of the total current is needed for the reduction of the copper-oxide. This might be true if during the reaction, there is reoxidation of the Cu^0 happening. Several studies have reported reoxidation of Cu^0 during the reaction by oxidative species in the electrolyte, and might thus be the reason for the deficit in the F.E.[67,68].

As mentioned, the catalysts do not display a significant difference in selectivity, suggesting that their structure are more similar under working conditions. The next section will discuss their post-catalytic structures measured with *ex-situ* XRD and SEM.

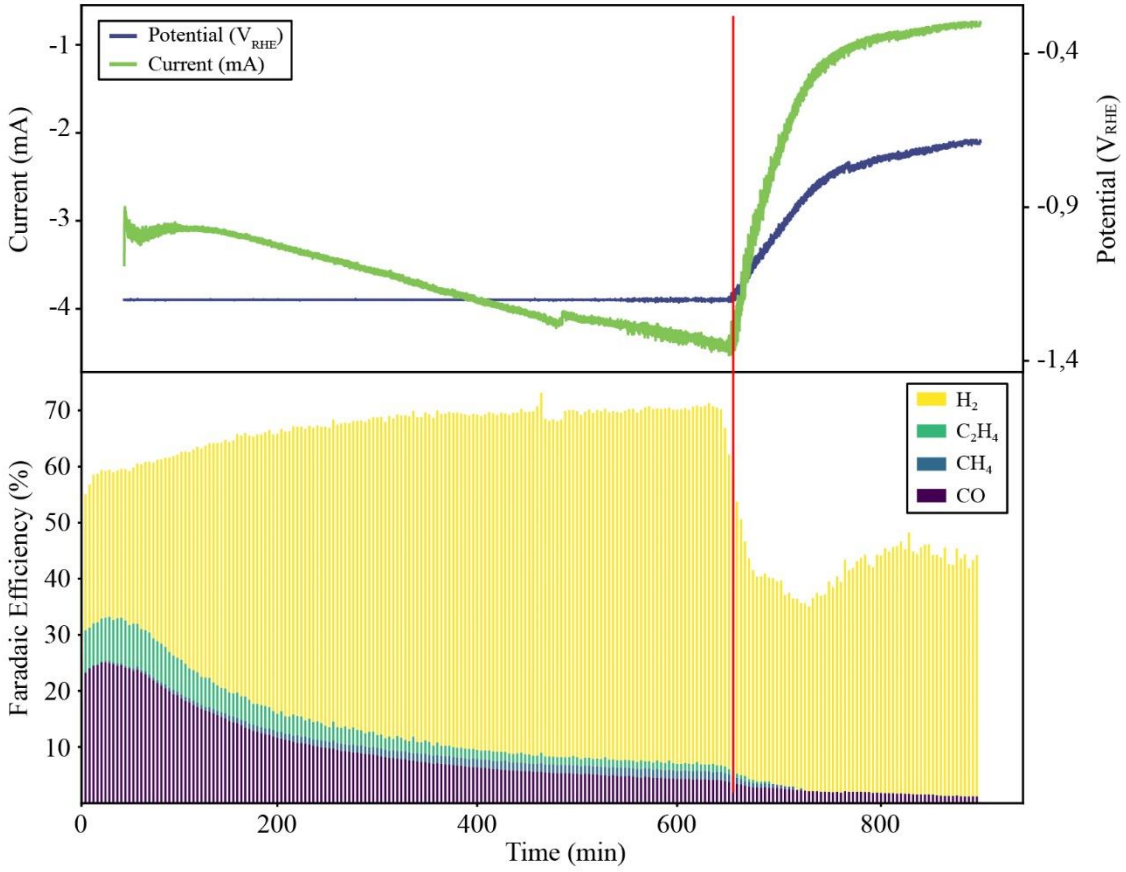

Figure 21: Upper graph: current and potential over time for the catalytic test of the truncated-octahedrons at -1,2V. A clear decrease in both can be seen after ~650 minutes, indicating the malfunctioning of the system. Lower graph: F.E. over time for the same experiment, with the same decrease after the malfunctioning happens.

4.3 Post-catalytic Structure & Morphology

The results of both the *ex-situ* XRD and SEM are shown in Figure 22. The upper graph shows the results of the *ex-situ* XRD and the lower Figure the *ex-situ* SEMs. All experiments were performed at -1.0V, with XRD samples after 5 minutes and 60 minutes, and SEM samples after 5, 15, and 60 minutes.

To compare, the diffractograms of the as-synthesized cubes and octahedrons are added and vertical lines are added to indicate Cu_2O (111) & (200) in red and Cu (111)/(200) in blue. After just 5 minutes, most of the peaks relating to Cu_2O have disappeared already, and new sharp peaks at 29,8° & 45,6° start to develop. The peak ratio of Cu_2O (111) / (200) for the cubes also changes after 5 minutes. Before applying a potential, the (200) peak dominates over the (111) peak with (200)/(111) = 2,04, but after 5 minutes, the (111) peak dominates and (200)/(111) = 0.95. This could indicate that the (111) facet is more stable than the (200) facet. Furthermore, no significant peaks for metallic copper arise after applying the potential, not even after 60 minutes. However, there seems to be a small peak for Cu(111) after 5 minutes for both the cubes and the octahedrons, but not for the Cu(200). One could then argue that the Cu_2O gets mainly transformed into Cu(111), but the peak is too small to draw this conclusion. Also, no conclusions about the stability of Cu_2O (111) & (200) can be drawn from the octahedrons, as there is no Cu_2O(200) peak present in the fresh catalyst, nor after 5 or 60 minutes. Then there are the sharp and strong peaks at 29,8° & 45,6° that remain unidentified. No match was found for the peaks in the ICDD (International Centre for Diffraction Data), while searching with a chemical filter containing the elements H, C, O, K & Cu. No combination of the elements could provide a good match with both peaks. Performing HR-TEM and EDX could provide more information about the crystalline structure and atomic composition of this phase. Even though they are unidentifiable for now, they do show different peak ratios for the cubes and the octahedrons. This shows that this unknown phase has different growth directions on the two catalysts. *Ex-situ* XRD experiments are difficult, as the sample may alter in the time between the electrochemical setup and the diffractometer. Even though the transfer time has been kept to a minimum, a diffractogram takes approximately ~30 minutes, meaning that the sample may still be altering during the measurement. To get a better understanding about the evolution of the crystalline structure, *in-situ* XRD experiments would be ideal. However, *in-situ* XRD experiments require very sophisticated setups. An *in-situ* XRD electrochemical cell was available, but the measurements failed. The system was not able to apply the set potential (-1.0V), it was not able to reach appreciable current densities, and the peaks for copper-oxide did not disappear, even after ~30 minutes.

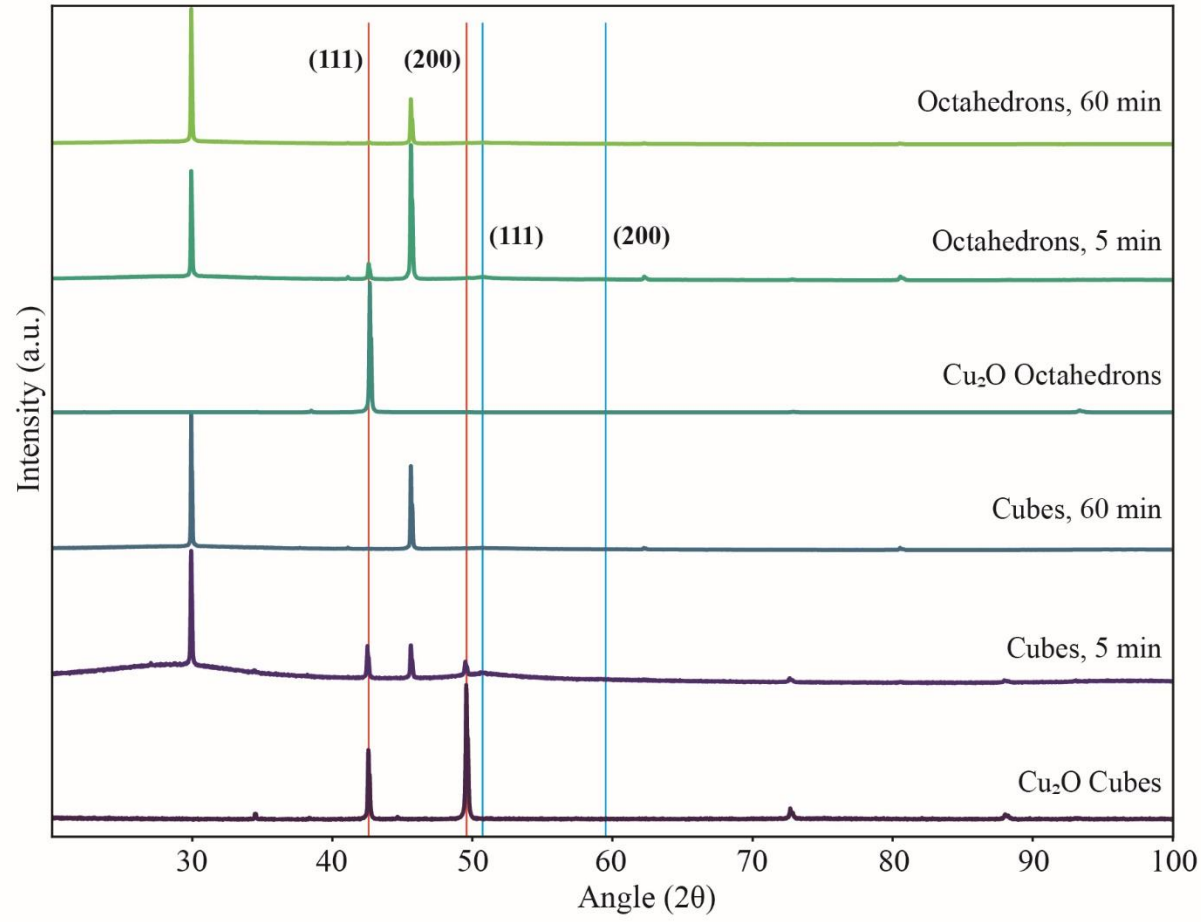

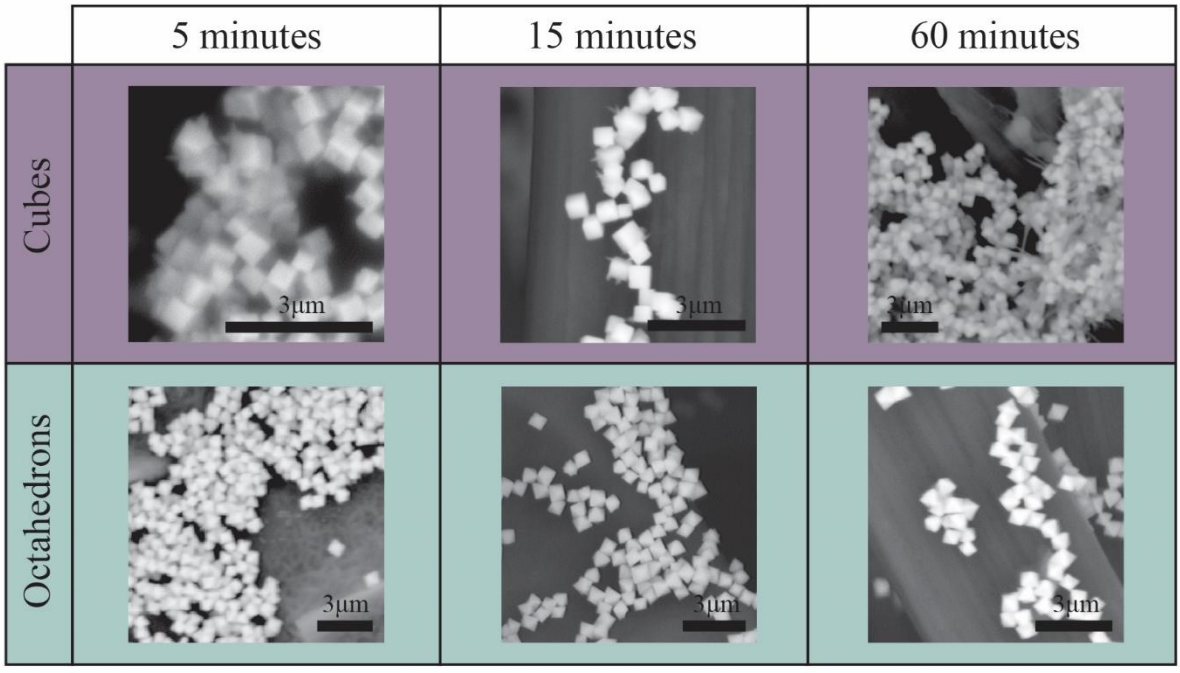

Figure 22: Upper graph: ex-situ XRD measurements of the cubes and octahedrons after 5 and 60 minutes at -1.0V. With the red lines indicating the Cu_2O (111) & (100) and the blue lines the Cu(111) & (100). Lower graph: ex-situ SEM pictures of the cubes and octahedrons after 5, 15 & 60 minutes at -1.0V. The cubes show more dendrite formation over time than the octahedrons.

The argument that the $Cu_2O(111)$ facet is more stable than the (200) facet can be further supported by the *ex-situ* SEM images. After 5 minutes at -1.0V, the cubes already show dendrites growing out of the particles, which is not the case for the octahedrons. With increasing times, the dendrites become more common for the cubes, whereas the octahedrons retain their pristine morphology. The octahedrons also showed some dendrite formation after some time as can be, but this was way less common than for the cubes. Still, SEM is not a bulk technique, making this conclusion less strong as there is a possibility that the SEM measurements were taken at spots that contain more or less dendrite formations.

These experiments show that we have a structurally dynamic system, that changes over time. Figure 21 in the previous section also showed a dynamic catalytic behavior over time, before the malfunctioning happened. As mentioned in the introduction, a dynamic system is preferable when conducting kinetic studies on reaction mechanisms. By measuring the surface intermediates of the catalyst over time via time-resolved *in-situ* Raman spectroscopy, changes in the catalytic behavior could be correlated to changes in the surface intermediates and could provide more insights into reaction pathways towards certain products. Therefore, the next section describes the catalytic behavior over time, after which the system is described with *in-situ* Raman spectroscopy.

4.4 Time-dependent catalytic behavior

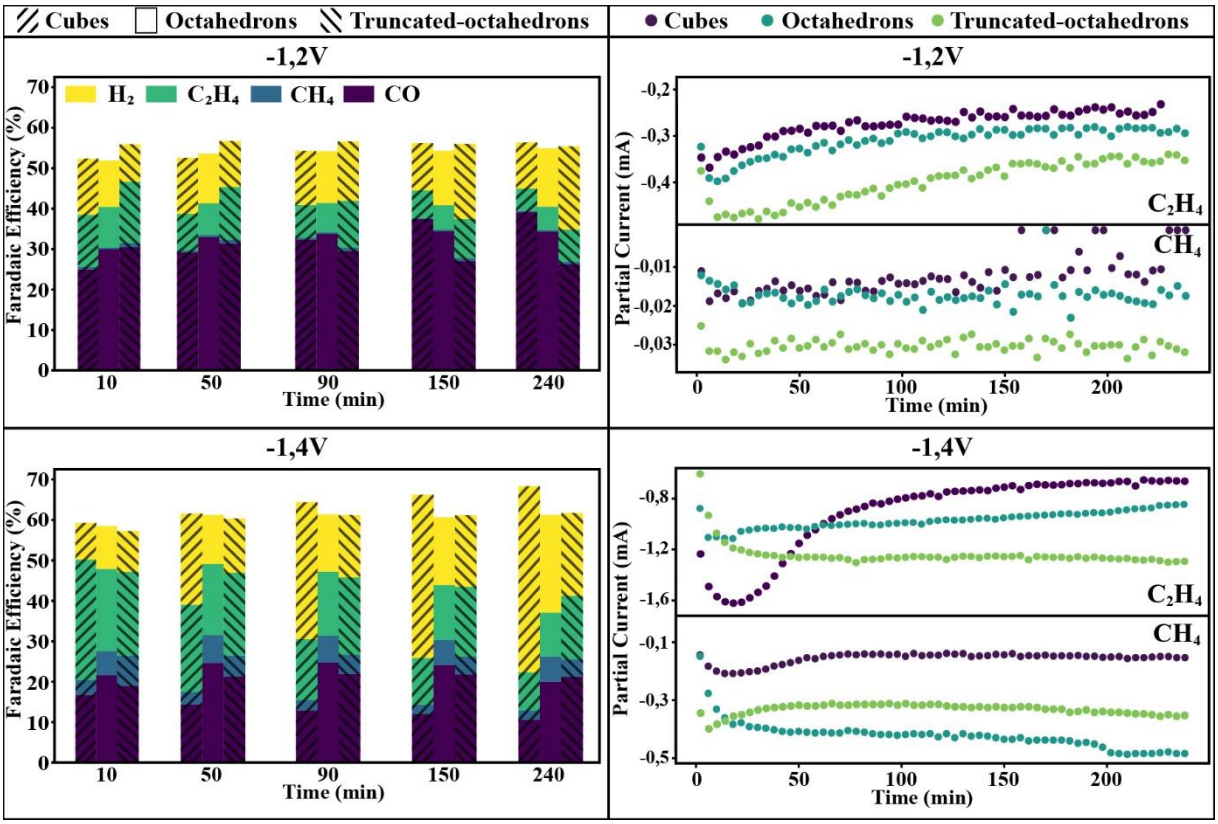

Figure 23: Time-dependent activity data for all three catalysts at -1,8$V_{Ag/AgCl}$ (top) & -2,0$V_{Ag/AgCl}$ (bottom). The left two graphs show the F.E. over time for all 4 the gas products, the right two graphs show the partial current over time for C_2H_4 and CH_4.

This section describes the catalytic behavior of all three catalysts over 4 hours. The measurements were performed on -1.2V and -1.4V, and just like the previous activity measurements of section 4.2, only gaseous products are analyzed. All measurements were performed in duplo. Figure 23 shows the time-dependent catalytic behavior of the first experiments. The left two graphs show the F.E. over time and the right two graphs show the partial current densities for methane and ethylene. The upper two graphs are measured at -1.2V and the lower two graphs at -1.4V. The results of the duplo experiments are shown in Figure 33 in appendix A. The duplo experiments all have a quicker deactivation then the first experiments, with a F.E. of >50% for H_2 after 4 hours. One explanation for the quicker deactivation could be the loss of catalyst particles on the substrate during the experiments. The duplo experiments were performed on a different batch of prepared carbon paper which might have had worse adhesion properties for the catalyst particles. Nonetheless, the F.E. for both experiments to CH_4 at both overpotentials remains rather stable, in comparison to the rather quick decrease of C_2H_4. This stability of CH_4 is difficult to distinguish as it is a rather small percentage, but it is more visible for the corresponding partial currents in the right two graphs. There, one can see that the partial current for CH_4 remains stable or even increases over time for all 3 catalysts at both overpotentials, whereas the partial current for C_2H_4 decreases. The increase of the partial current of CH_4 is the most pronounced at both overpotentials for the octahedrons and the truncated-octahedrons. The cubes have a more stable partial current for CH_4 at both

overpotentials. At -1.2V, all three catalysts have a similar decrease in partial current for C_2H_4. At -1.4V, the cubes have a quick initial decrease for C_2H_4 and then attenuates and the truncated-octahedrons even have a stable partial current for C_2H_4. The duplo experiments show similar trends in selectivity over time. At both overpotentials, the selectivity towards C_2H_4 decreases over time for all the catalysts and the selectivity towards CH_4 increases, except for the cubes, where it remains rather stable.

In the introduction, we saw that CH_4 and C_2H_4 have a few intermediates in common, such as CO*. But immediately after that, they mainly follow different pathways. And since there is a noticeable change in selectivity over time for all three catalysts, the surface intermediates should also change over time. Especially since the efficiency for CH_4 remains stable or even increases, the surface state likely changes towards a more beneficial environment for CH_4 production, even though the production is still low (~6%). This could be due to a change in the pH of the environment near the catalyst's surface, as the RDS for CH_4 is pH dependent as mentioned in the introduction. However, measuring the pH near the surface of the catalyst is difficult and a change in pH will nonetheless lead to a change in surface intermediates. By employing *in-situ* Raman spectroscopy on the same time-scale of the activity measurements, this change could be made visible, and vibrations could be assigned to be CH_4-directing or C_2H_4-directing. As all three catalysts possess different selectivities over time, they will also possess differently changing surface intermediates. *In-situ* Raman is an ideal technique to visualize these changing surface intermediates and to monitor the dynamic behavior of the catalysts which could then provide more mechanistic insights into the pathways towards to key products CH_4 and C_2H_4. The next section will discuss the Raman measurements.

4.5 Raman spectroscopy

In the previous section, the catalytic behavior of the catalysts as a function of time and potential was discussed. All catalysts showed a dynamic behavior that changes over time and with potential, and differences between the catalysts were found. This section will discuss the Raman measurements to better understand the catalytic behavior.

4.5.1 Potential Dependent Raman

First, to better understand the chemical surface state of the catalysts under working conditions, Raman spectra at different overpotentials were taken, and the results are shown in Figure 24. These spectra are the average of 25 spectra taken consecutively on the octahedrons at overpotentials ranging from −0.3V to −1.0V. Higher overpotentials (>−1.0V) are not added as the catalyst became too active at these conditions and produced too many bubbles. If a bubble was formed on or near the laser spot, the objective became out focus and the signal disappeared. There also seemed to be a driving force for the bubbles to stick to the objective, resulting in the same problems. It should be noted that the Raman measurements are performed in another electrochemical cell than the activity measurements. The Raman measurements could not be performed on the H-cell as the microscope objective is required to be in close proximity (<1 mm) to the electrode. Using a different cell could have an influence on the dynamics of the eCO2RR. So, −1.0V in both cells might not give the same catalytic performances, also because of possible differences in the IR drop. The IR drop was not calculated for the Raman cell and this possible difference could thus not be corrected for. The measurements were also performed on the cubes at -1.0V, and the respective spectra are shown Figure 34 in appendix A. As mentioned in section 2.2, the power of Raman, compared to IR, is the ability to measure low vibrational frequencies of molecules and intermediates (100-500 cm^{-1}) which contains information of intermediates bound to the metal surface.

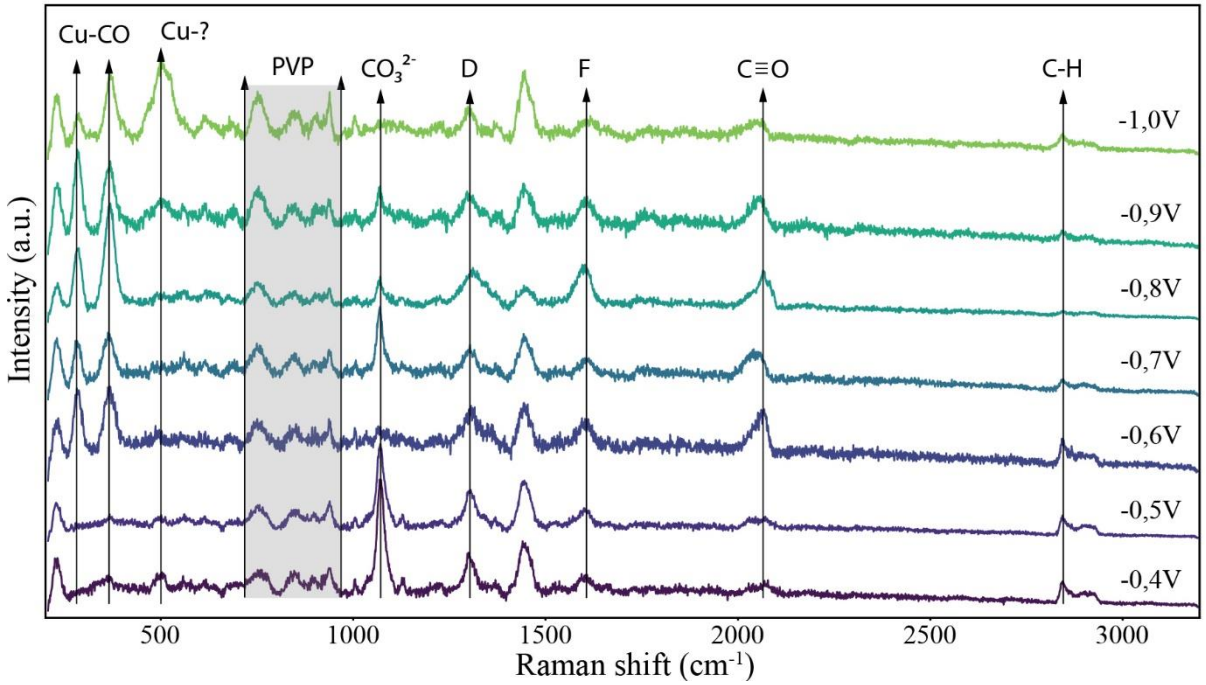

Figure 24: Average of 25 Raman spectra taken at different overpotentials for the Cu_2O octahedrons. Peaks for reaction intermediates, electrolyte species, the glassy carbon substrate and PVP can be found. There is also the unknown peak at 500 cm^{-1}.

First, the vibrations that do not originate from intermediates from the eCO2RR are discussed. The D- and F- bands of the glassy carbon substrate are often visible and are located at 1320 and 1600 cm^{-1}, respectively. The intensity of these bands depends on the location where the measurement is taken, with lower intensities where more Cu_2O particles are present as the particles then block the signal of the glassy carbon. A Raman spectrum of the GCE can be found in Figure 35 in appendix A, where the D- and F- bands are clearly visible. Next, there are the vibrations between ~750 – 1000 cm^{-1} originating from residual PVP, which is used during the synthesis of the octahedrons. PVP was added during the synthesis of the octahedrons as a stabilizing agent for the (111) facet. These vibrations could be characterized as PVP by comparing them to the recorded Raman spectrum of PVP powder shown in figure 35 in appendix A. Besides that, these vibrations are not present in the spectra recorded with the cubes, where no PVP is used during the synthesis. Lastly, there is the sharp carbonate (CO_3^{2-}) symmetric stretch vibrations at 1060cm^{-1}, which originates from the electrolyte, $KHCO_3$. This vibration is also visible in the spectrum of pristine glassy carbon in CO_2-saturated $KHCO_3$, where no catalysis is taking place. Furthermore, this assignment is reported in other studies as well on this system utilizing $KHCO_3$ as the electrolyte[27,35]. No signal originating from the bicarbonate (HCO_3^-) is found in the spectra, which should be at 1020cm^{-1}. Other studies have reported on the absence of the bicarbonate peak too, and ascribed it to the rapid deprotonation of bicarbonate into carbonate due to the alkaline environment near the surface of the catalyst[27]. The alkaline environment is a result of the rapid reduction of copper-oxide, which produces hydroxide ions, as can be seen from equation 7

Secondly, there are many vibrations that do originate from intermediates of the eCO2RR. First, the two intense peaks at 280/360 cm^{-1} originate from the CO* intermediate and indicate the frustrated rotation of Cu-CO and stretch vibration of the Cu-CO bond, respectively (see figure 6 in the introduction). These vibrations are always accompanied by the stretch vibrations of the much stronger C-O bond at 2000-2100 cm^{-1} (figure 6 in the introduction). The distinct shape of this band is due to the different vibration modes of CO when bound to the surface, LFB-CO & HFB-CO, as discussed in the introduction[32,27]. These CO* vibrations only occur at potentials of -0.6 V and more cathodic for both the cubes and octahedrons, while the study by Moradzaman et al. reported these vibrations from -0.4 V[35]. However, they used an electropolished, polycrystalline copper electrode. At ~2900 cm^{-1}, there are the C-H stretch vibrations which could originate from different intermediates. PVP also possesses some vibrations in this region, but the cubes also show C-H vibrations, meaning that there are at least some C-H vibrations originating from intermediates. Furthermore, since the C-H stretch vibrations also occur at the low overpotentials (-0.4V), where only CO and HCOOH are produced, they might originate from formate-like intermediates. Two still unknown peaks in Figure 24 are located at 500 cm^{-1} and 1440 cm^{-1}. The 1440 cm^{-1} peak is strong and sharp at all overpotentials for both the octahedrons and the cubes. Species that are often found here are carbonate and formate-like species, but there is still a lot unknown about this region, also because there is much happening[29]. A study from 1999 on a $Pt/Au/SiO_2$ thermocatalyst assigned a band at 1440cm^{-1} in an IR spectrum to adsorbed ethylene on silica[69]. They found several vibrations in this region that corresponded to different binding modes of ethylene and ethylene-like species. Even though our system is completely different, it might suggest that the vibration

at 1440cm^{-1} in our system originates from an ethylene-like species. However, the 1440cm^{-1} vibration is visible at all overpotentials and the intensity does not seem to change with potential, and ethylene production generally only becomes relevant at higher overpotentials as reported already by Hori[13]. A study by Zahid et al. does report an on-set potential of -0.1V for ethylene on a CuO catalyst[36]. ODC catalysts are known for lowering the on-set potential of the eCO2RR, and the on-set potential for ethylene in our system might thus be -0.4 V or even more anodic[8,24]. Activity measurements at these low overpotentials can prove the low on-set potential for ethylene in our system. Furthermore, Raman measurements at overpotentials more anodic than -0.4 V can reveal more on the dynamics of this intermediate. The other unknown vibration at 500 cm^{-1} is often ascribed to a surface-bound hydroxyl species, Cu-OH[27,35], but it lacks experimental evidence[35]. Furthermore, the band at 500 cm^{-1} in Figure 24 consists of at least three peaks as indicated by the shoulders, suggesting that, if one of them is Cu-OH, there are more species. Interestingly, this band only appears from -0.9V and more cathodic, suggesting that it is an intermediate towards a product that is only produced at these higher overpotentials. An unpublished work by our group proved the presence of a carbon atom in these intermediates through labeling experiments. $^{13}CO_2$ was used in these experiments which showed a peak shift for the 500 cm^{-1} vibrations. This means that the frequency of the vibration changed due to the increased mass in the carbon atom (see equation 13 and 14), and thus proves the presence of the labeled atom.

As seen in section 4.2, the catalytic selectivity is strongly dependent on the applied potential. This might suggest that the vibrations at 500 cm^{-1} originate from intermediates towards a certain product that is only obtainable at certain potentials. Since the catalytic activity also changes over time, the surface intermediates likely also changes over time. Performing time-resolved Raman measurements could then provide more insights into these unknown bands at 500 cm^{-1}. The time-resolved Raman measurements are discussed in the next section.

4.5.2 Temporal Spectral Evolution

Section 4.2 & 4.4 showed the dynamic catalytic behavior of the catalysts with time and potential, and the previous section showed that the surface adsorbed species also shows a potential dependency, especially the unknown bands at 500 cm^{-1}. To now also look into the time-domain for the surface state, time-resolved Raman measurements were performed on all three catalysts at -1.0V and the results for the cubes and octahedrons are shown in Figure 25. The truncated-octahedrons gave very little signal originating from the eCO2RR and are the least discussed. The low signal could be due to low SERS, as there is strong signal from the glassy carbon, but not adsorbed species on the catalyst. The results for the truncated-octahedrons are shown in figure 36 in appendix A. The spectra are the average of 5 spectra taken each 5 minutes at different spots, to take into account possible spatial variations for a total of 2 hours. The graphs on top show the recorded Raman spectra in a window of 200–3200 cm^{-1}. For the first 15 minutes, the cubes and octahedrons show similar spectra as in the previous section. However, spectral changes are found at longer times in the low (250 – 550 cm^{-1}) and high (1900 – 2100 cm^{-1}) wavenumber regions.

For clarity, zoom-in graphs are added in the bottom of figure 25 of the low and high wavenumber regions. Considering the initial spectra for the first 15-30 minutes of the cubes and the octahedrons, intense Cu-CO and C-O bands are observed at 280, 360 and 2090 cm^{-1}, respectively. However, these bands disappear in a timeframe of 30 minutes while at the same time, new Raman features arise. For both the cubes and octahedrons, the strong bands around 500 cm^{-1} develop,

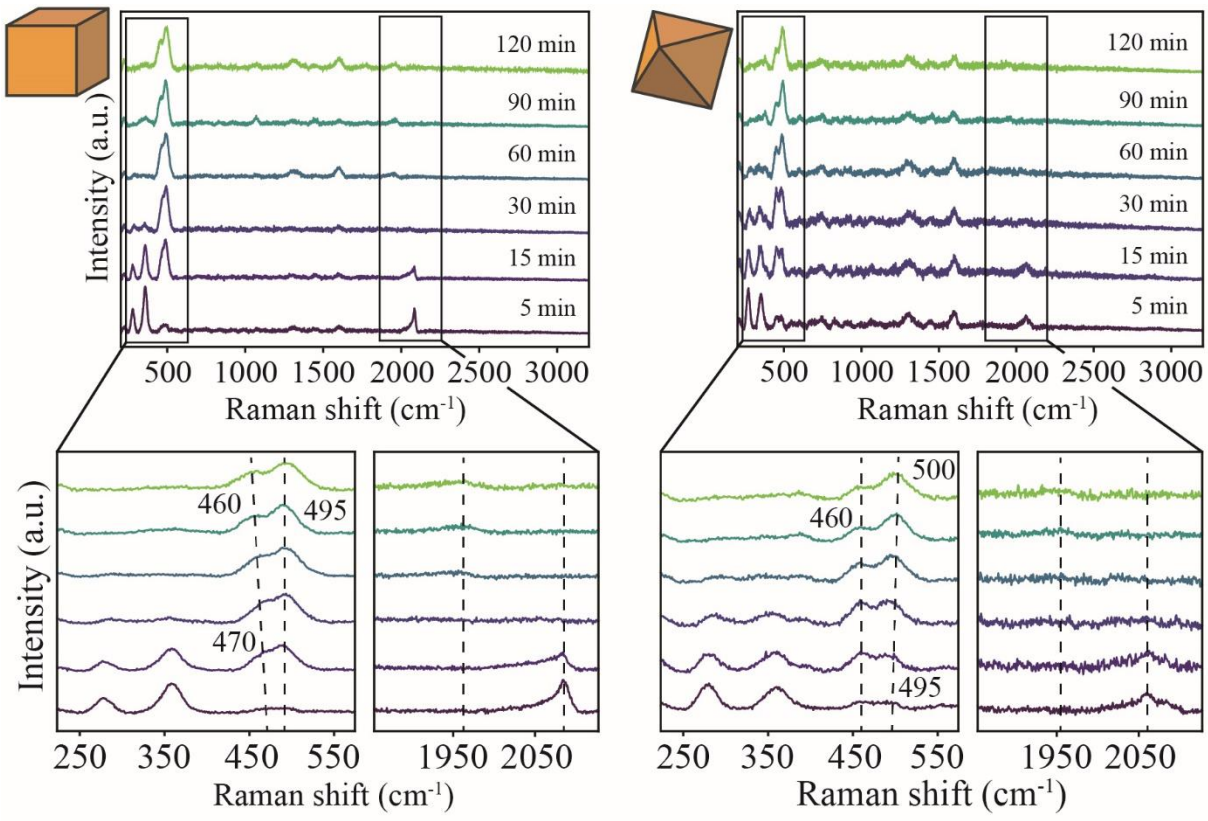

Figure 25: Time-resolved Raman spectra recorded on the cubes (left) and the octahedrons (right). All measurements were taken in the timespan of 2 hours at -1.0V. The bottom shows the zoomed in parts of the 400 cm^{-1} and 2000 cm^{-1} regions for each experiment.

which were also visible in the potential-dependent Raman measurements. These ~500 cm^{-1} bands last for the remainder of the experiments and change spectral shape over time. Furthermore, the disappearance of the high wavenumber CO bands is accompanied by the development of a weak band at 1950 cm^{-1}, which is known to be from a bridged CO modality[27]. Bridged CO is double bonded to the catalyst, and it has been suggested that it is less selective towards ethylene than linear CO[31]. The CO bands in both the low and high wavenumber regions are absent for the truncated-octahedrons. However, a weak band at 505 cm^{-1} appears after 30 minutes just like the cubes and octahedrons. The peaks at ~500 cm^{-1} for the cubes and the octahedrons look very similar; they both possess a strong band at 495/500 cm^{-1} with a shoulder. Furthermore, the shoulder for the cubes seems to shift from 470 cm^{-1} to 460 cm^{-1}, whereas it remains stable for the octahedrons at 460 cm^{-1}. A peak-shift that is clearer, is the shift for the 495 cm^{-1} peak for the octahedrons. This peak shifts from 495 cm^{-1} to 500 cm^{-1} over the course of the 2 hours, whereas it stays at 495 cm^{-1} for the cubes. The weak band for the truncated-octahedrons also shifts from 492 cm^{-1} to 505 cm^{-1} over time. As mentioned in section 2.2, a higher wavenumber in a Raman spectrum means a stronger bond which means that the bond of the 495 cm^{-1} increases over time.

As stated in section 4.4, combining the time-dependent activity measurements with the time-dependent Raman data could potentially provide more insights into the reaction mechanism of the eCO2RR. Simultaneous changes in product selectivity and spectral characteristics could highlight certain intermediates that are selective towards certain products. Figure 23 revealed that at -1.2V, the F.E. and partial current for ethylene always decreased for all three catalysts. The F.E. and partial current for methane on the other hand increased over time for the octahedrons and truncated-octahedrons, except for the cubes. The partial current for ethylene was also twice as high for the cubes than the other catalysts. In the time-dependent Raman, we see that the cubes have the stable band at 495 cm^{-1}. This peak is also visible in the early stages for the octahedrons, but it then shifts towards higher wavenumbers. This combination of the time-dependent

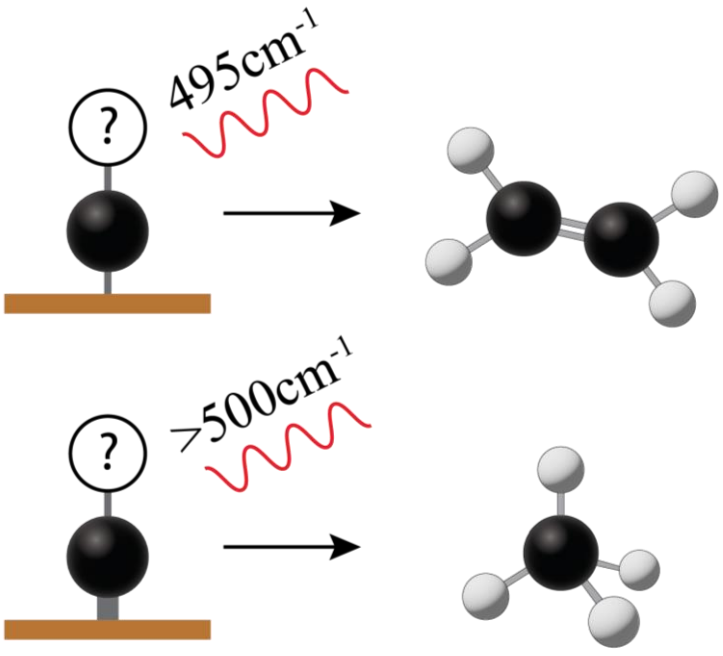

Figure 26: The vibration at 495 cm^{-1} is suggested to be an ethylene directing species (top) and the 500 cm^{-1} vibration is suggested to be a methane directing species which also has a slightly stronger bond to the metal surface than the 495cm^{-1}, as indicating by the thicker bond.

activity and Raman can then suggest that the 495 cm^{-1} peak might be an ethylene directing species, whereas the >500 cm^{-1} band might be a methane directing species (Figure 26). As higher wavenumbers in Raman indicate stronger bonds, the >500 cm^{-1} species might be a stronger bound intermediate, that dimerizes more difficult than the 495 cm^{-1}, inhibiting the production of C_{2+} products. The truncated-octahedrons show very similar time-dependent catalytic behavior as the octahedrons, and they also show a similar peak shift from 492 cm^{-1} to 505 cm^{-1}, supporting the statement. There is also the 460 cm^{-1} peak which is still unknown and appears at both the cubes and octahedrons. This band might originate from the bridged CO modality which is also visible in the higher wavenumber region and since it takes over the linear CO bands at 280/360 cm^{-1}. This is also in line with the theory about higher wavenumber, stronger bond, as bridged CO is double bonded to the surface, in comparison to the single bond of linear CO, resulting in a stronger bond. The 460 cm^{-1} band is also absent for the truncated-octahedrons, which also shows the absence of the bridged CO band in the higher wavenumber region.

To further investigate these bands, the spectral evolution of the peaks in the 500 cm^{-1} region for the cubes and the octahedrons is given in Figure 27 in a stacked manner, together with the ratio of the 495/500 cm^{-1} (B2) band over the 460 cm^{-1} (B1) band. Blue graphs in Figure 27 represent the start of the experiment with more yellow graphs representing the end of the experiment. Something that becomes clear when visualizing the spectral evolution in this stacked manner, is that both B1 and B2 simultaneously grow and remain relatively the same for the cubes, where B1 increases and B2 decreases over time for the octahedrons. The shift of B2 from 495 cm^{-1} to 500 cm^{-1} for the octahedrons also becomes clearer. The peak ratio B2/B1 strongly increases for the octahedrons where the ratio stays more stable for the cubes. This is something that we have seen for the partial currents for methane too. There, the partial current increased for the octahedrons whereas it also stayed stable for the cubes. This could indicate that there is a relation between methane production and the bands in the 500 cm^{-1} region. If the 460 cm^{-1} peak is bridged CO, then Figure 27 can suggest that the bridged CO coverage stays stable for the cubes and decreases over time for the octahedrons, as the peak intensity decreases.

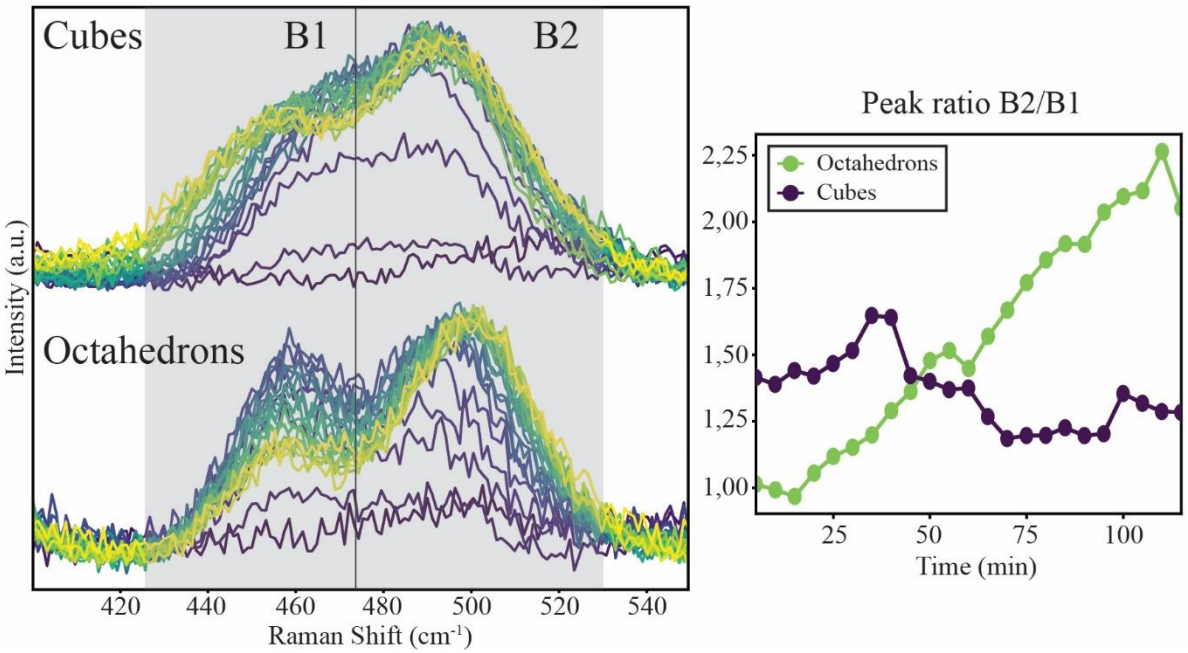

Figure 27: Left: evolution of the 500 cm^{-1} Raman bands over time for the cubes and octahedrons, with blue spectra representing the start of the experiment and yellow the end of the experiment. Right: the peak ratio B2/B1 over time for the cubes and octahedrons.

As stated in the introduction and section 2.1.2, the CO* coverage is an important factor for C_{2+} production as two CO* species need to be close enough to each other to form a C-C bond. A decrease in CO* coverage for the octahedrons then might be partially the reason for the decrease in C_{2+} production and the increase in methane production, as lone CO* species are then more prone to further reduction to methane instead of CO-CO coupling. The work by Roldan et al., discussed in the introduction, also provides a method of measuring the CO* coverage for linear CO. For this, the ratio of the two linear CO vibrations in the lower wavenumber region (360 cm^{-1} / 280 cm^{-1}) should be calculated with a higher ratio indicating a higher coverage. This spectral evolution of these two bands and their respective ratio are given in figure 28 for the cubes and the octahedrons. The first thing to notice is the overall higher ratio for the cubes, meaning that they possess a higher CO* coverage. As seen in the temporal Raman measurements, linear CO disappears after ~30 minutes, which is also clear in figure 28. The cubes show a decreasing ratio of these bands before linear CO disappears, indicating a decrease in coverage. The octahedrons on the other hand show an increase in ratio, which would indicate that before linear CO disappears, the coverage actually increases. Overall, the CO* coverage is higher for the cubes than for the octahedrons, which might then be partially the reason that the cubes in general produce more C_{2+} products. However, previous literature suggest that CO-CO coupling is not the only possible mechanism for the production of C_{2+} products. The work published by Koper et al. back in 2012 suggested two different reaction pathways for the formation of ethylene, based on high time-resolution activity measurements[22]. One of these pathways has a shared intermediate with the methane pathway, the other one does not yield methane[57]. The two pathways could explain the spectral behavior that we observe in the temporal Raman measurements. The first pathway occurs at the start of the experiment, where linear CO is involved, and the second pathway occurs after ~30 minutes, involving a bridged CO and the new 495 - 500 cm^{-1} intermediates. As all catalysts show the 495 cm^{-1} band, this might be the shared intermediate towards CH_4 and C_2H_4.

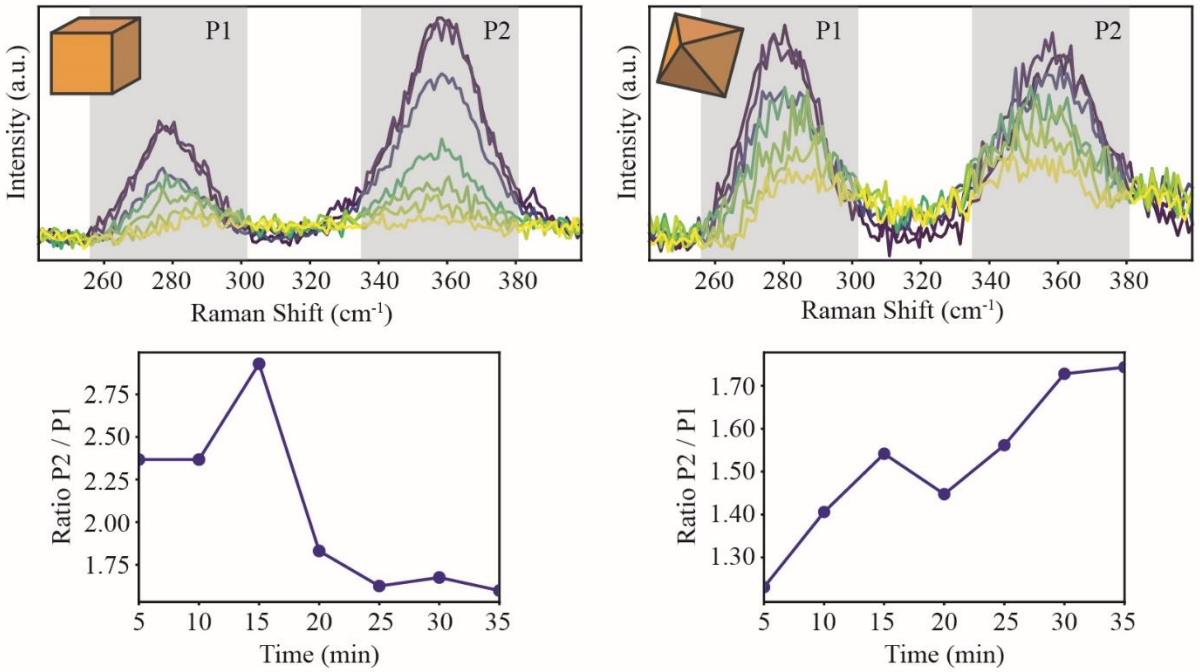

Figure 28: Spectral evolution of the frustrated rotation vibration of linear CO (P1 @ 280 cm^{-1}) and the stretch vibration of linear CO (P2 @ 360 cm^{-1}) in the first 35 minutes of the temporal Raman measurements. The left graph is for the cubes and the right graph for the octahedrons. The bottom two graphs show the ratio of P2/P1 over this timeframe where a decrease is found for the cubes and an increase for the octahedrons before linear CO disappears from the surface (after 35 minutes).

To try and find what these new intermediates might be, and what the possible reaction pathways are, the overview of all the proposed intermediates provided by Nitopi et al. can be used[8]. The speculations that we made in the previous sections are that 460 cm^{-1} is a bridged CO modality, 495 cm^{-1} is an ethylene directing species and a shared intermediate with methane, and >500 cm^{-1} is a mainly methane directing species. Figure 29 shows a simplified version of the large overview by Nitopi et al., highlighting the most important reaction intermediates. From CO, there are two main pathways, towards ethylene and towards methane. The ethylene pathway requires a C-C coupling step, where methane does not. It has often been speculated that the C-C coupling mechanism goes via CO-CO coupling, resulting in the OCCO* intermediate. However, our time-dependent Raman data suggests that there are species beyond linear CO that are still able to produce ethylene, as the vibrations of linear CO disappear after 30 minutes. As the F.E. for methane increases and ethylene decreases over time, it is unlikely that this species beyond CO is the OCCO* intermediate, since that should result in more C_{2+} products. The other possibility then is the aldehyde (-CHO) intermediate, as shown in Figure 29, which has one more electron than CO*. According to the overview by Nitopi et al., this intermediate can still be reduced into both methane and ethylene. This intermediate can produce C_{2+} products via CO insertion which results in the OCCHO* intermediate. This aldehyde species is thus a shared intermediate for ethylene and methane and could then be ascribed to the 495 cm^{-1} band. This would mean that the bond strength then also increases as the wavenumber increases. The carbon is still bound to the metal surface through one bond, but the chemistry of the intermediate does change. Oxygen becomes double bonded with the carbon, making the oxygen less electron withdrawing and a hydrogen bond is formed, which is electron donating. This all results in more electron density at the carbon and thus into the bond with the metal surface, strengthening the bond. Furthermore, since there is no linear CO on the surface, the dimerization likely occurs with a bridged CO, which, as discussed, would then be the 460 cm^{-1} band. This is however conflicting with literature about bridged CO, which describes bridged CO as a bystander or even deactivating species[31]. However, our data suggests that hydrocarbons production is achievable without linear CO. This does not exclude the possibility that bridged CO is a bystander species and that C-C coupling occurs without a CO species. The peak shift for the octahedrons and truncated-octahedrons towards >500 cm^{-1} could then be caused by the further reduction of the -CHO species into the alcohol intermediate -CHOH. The increase in wavenumber can then be explained by the double bond nature that the -CHOH intermediate has as can be seen in Figure 29, increasing the bond strength. This species is one step closer to methane and has a stronger bond to the surface, which potentially makes it more methane directing. These assignments are speculations based on the time-dependent activity and Raman measurements, together with previously proposed intermediates via theoretical calculations, and are no conclusive proof.

To summarize, our Raman data suggests that with time, the surface intermediates of the catalyst change from dominated by linear CO to species beyond CO, found at 460, 495 and >500 cm^{-1}. It is speculated that the 495 cm^{-1} species is a shared intermediate between C_2H_4 and CH_4 and that the >500 cm^{-1} species is a methane-directing intermediate. A weak band at 1950 cm^{-1} suggests the presence of bridged CO after the disappearance of linear CO and might also be the origin of the 460 cm^{-1} band.

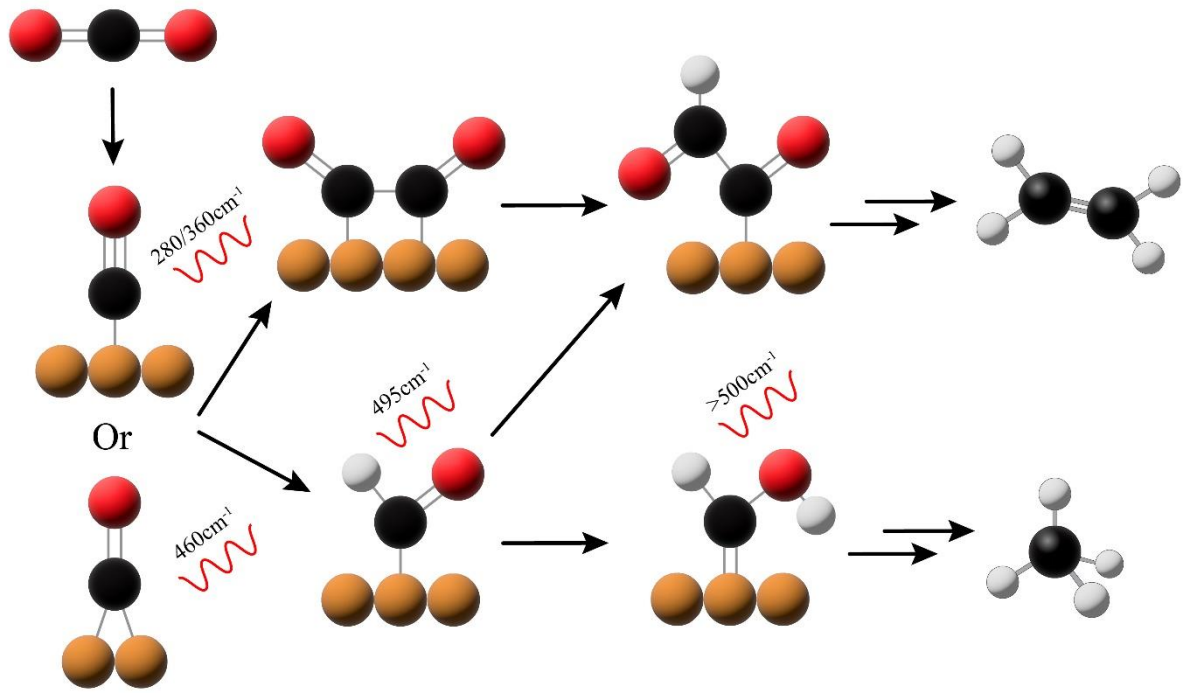

Figure 29: Simplified version of the complete overview of all the reaction intermediates as provided by Nitopi et al.[10]. The key intermediates have been added together with their proposed vibrational energies as discussed in the last section.

CONCLUSIONS

This thesis describes a spectroscopic study on the reaction mechanism of the electrochemical CO_2 reduction reaction, using well-defined Cu_2O sub-microcrystals as the catalyst. The catalysts were prepared via a facile aqueous synthesis route with delicate control over the exposed facets by adding varying amounts of the stabilizing agent PVP. This synthesis yielded cubes with (100) facets, octahedrons with (111) facets and truncated-octahedrons with a combination of the (100) & (111) facets. Characterization of the catalysts by X-ray diffraction revealed the presence of the cubic phase and cyclic voltammetry showed distinct reduction and oxidation regions for the catalysts.

Next, the catalysts were tested in an H-cell at -1.2V and -1.4V to investigate their activity. At -1.2V, CO was the dominant product with a F.E. of 25-30% followed up by C_2H_4 and there were only small differences found between the catalysts. Furthermore, at -1.2V, CH_4 only had a F.E. of ~1% for all three catalysts. At -1.4V, C_2H_4 became the dominant product for all three catalysts, the F.E. for CH_4 increased to 4-6%, and the differences between the catalysts also became more significant. The cubes had the highest F.E. for C_2H_4 with 29% and the lowest F.E. for CH_4 with 4%, and the octahedrons had the lowest F.E. for C_2H_4 with 20% and the highest F.E. for CH_4 with 6%. Post-catalytic *ex-situ* characterization with XRD and SEM showed that most of the copper-oxide is reduced after 5 minutes at -1.0V, and a still unknown phase develops. HR-TEM and EDX on this unknown phase could provide more insights into the crystalline structure and the atomic composition. Furthermore, the ratio of $Cu_2O(100)$ / $Cu_2O(111)$ decreased after 5 minutes for the cubes, suggesting a higher stability for the (111) facets. SEM revealed the growth of dendrites over time, especially for the cubes, where the octahedrons seemed more stable.

The catalytic behavior was then investigated in the time-domain. These experiments revealed a general decrease in selectivity towards C_2H_4 where the F.E. approximately halved over 2 hours, and a stable or even increasing selectivity towards CH_4. The increase in CH_4 selectivity was the most pronounced for the octahedrons, and the cubes had a more stable CH_4 selectivity, but the selectivity remained quite low (~1% at -1.2V and ~5% at -1.4V). To better understand this catalytic behavior, *in-situ* Raman measurements were performed. First, potential-dependent Raman measurements were conducted to gain knowledge about the present intermediates of the eCO2RR and other non-intermediate vibrations. Vibrations from the glassy carbon substrate, residual PVP and the electrolyte were found, along with vibrations originating from intermediates of the eCO2RR. Vibrations from the CO* intermediate were located at 280, 360 & 2090 cm^{-1} and C-H stretch vibrations were visible between 2800-2900 cm^{-1}. The origin of the C-H stretch vibrations remains unclear as many possible intermediates and reactants used in the synthesis possess such bonds. An unknown peak consisting of at least 3 vibrations located at 500 cm^{-1} showed signs of potential-dependency and was only visible at overpotentials lower than -0.8V for the octahedrons. The low vibrational energy of this vibration suggests a metal-intermediate nature and to gain more insights into the nature of these species, time-dependent Raman measurements at -1.0V were performed. These measurements revealed dynamic

surface intermediates over the course of 2 hours, with spectral changes in the low (250 – 550 cm^{-1}) and high (1900 – 2100 cm^{-1}) wavenumber regions. The strong bands originating from linear CO at 280, 360, and 2090 cm^{-1} disappeared in a timeframe of 30 minutes, whilst new strong vibrations develop between 460 – 500 cm^{-1}. Furthermore, the disappearance of the high energy C-O vibrations at 2090 cm^{-1} was accompanied by the development of a weak band at 1950 cm^{-1} which originates from a bridged CO modality.

To discuss the nature of these new species between 460 – 500 cm^{-1}, the data of the time-dependent activity and Raman measurements was combined. The time-dependent activity measurements showed a significant C_2H_4 and CH_4 production from start to end (4 hours), and the time-dependent Raman measurements revealed a dynamic change in surface intermediates. This combination suggests that there are two possible reaction routes towards these products, the first one involving linear CO that occurs in the initial stage of the experiments, and the second one involving the new species found between 460 – 500 cm^{-1}. The surface state changed to intermediates beyond CO, which then suggests that C_2H_4 and CH_4 have a shared intermediate beyond CO. The vibration at 495 cm^{-1} has been ascribed to this shared intermediate as all three catalysts possessed this vibration and was assigned to the -CHO intermediate. The vibration at ≥500 cm^{-1} was solely visible for the octahedrons and truncated-octahedrons over time, which also showed a more significant increase in methane production over time. For this reason, this vibration has been ascribed to a methane-directing species and was assigned to the -CHOH intermediate. Lastly, the vibration at 460 cm^{-1} has been speculated to be bridged CO, as the presence of this species was also proven by the vibration at 1950 cm^{-1}.

This thesis showed that *in-situ* Raman spectroscopy with good time resolution is ideally suited to gain insights into the dynamic catalytic behavior of a Cu_2O catalyst employed in the eCO2RR as it simultaneously probes the surface state and adsorbed species. Together with time-dependent activity measurements, the experiments revealed that there are two possible reaction pathways towards CH_4 and C_2H_4. The first pathway involves linear CO which occurs at the initial stage of the reaction, the second pathway involves an intermediate that is shared between CH_4 and C_2H_4 which occurs in the later stage of the reaction.

OUTLOOK

In this thesis, the presence of a second possible reaction pathway towards CH_4 and C_2H_4 has been found for the eCO2RR that happens via intermediates beyond linear CO. The nature of these intermediates has been discussed and several other experiments could be conducted to further prove the presence and nature of these intermediates.

First, temporal Raman measurements at different overpotentials could provide more dynamic insights into these new intermediates and their spectral evolution as the activity measurements also revealed a strong potential-dependency. Especially higher overpotentials would be interesting and might be more comparable with the current activity measurements. However, as explained in section 4.5, this is shown to be more difficult due to the higher activity of the catalyst resulting in bubble formation and the loss of focus for the objective. Ideally, an *operando* cell could be designed in which the catalytic performance and the spectral evolution over time could be measured simultaneously. This could possibly be achieved with the use of Differential Electrochemical Mass Spectrometry (DEMS) which uses mass spectrometry instead of GC to gain a higher time-resolution for the activity measurements.

Another experiment that could prove the presence of carbon atoms in these vibrations is performing CV during Raman. Changing the overpotential during the experiment can induce a Stark shift which will cause a shift in the peak position[25]. A negative Stark shift is characteristic for vibrations that include a carbon atom. If the vibrations possess a Stark shift, and the calculated Stark shift is negative, this will prove the presence of a carbon atom.

Using CO instead of CO_2 as the starting molecule could also provide more insights. If the same spectral changes occurs, with the development of the vibrations between 460 – 510 cm^{-1}, this will exclude the possibility that these vibrations originate from intermediates between CO_2 and CO. However, experiments with CO require sophisticated setups as CO is highly toxic. Furthermore, a different electrolyte must be used, such as KOH, as $KHCO_3$ is in equilibrium with CO_2 which will inevitably introduce CO_2 into the system. However, using KOH will lead to a more alkaline electrolyte which will then alter the catalytic performance as discussed in section 2.1.2. An acid can be added to the system, but this will also introduce more species which can again alter the catalytic performance.

Finally, pulsed electrolysis experiments can potentially provide more insights into the dynamics of the vibrations between 460 – 510 cm^{-1}, especially with anodic pulses. Anodic pulses will periodically reoxidize the surface and alter the surface state and morphology. The anodic pulses will also cause the removal of reaction intermediates between cathodic pulses. It is then interesting to see if linear CO reappears after an anodic pulse, or if the vibrations between 460 – 510 cm^{-1} will remain. Besides that, pulsed electrolysis is found to highly alter the catalytic selectivity which then also might alter the surface intermediates[70].

BIBLIOGRAPHY

(1) Robert, M. Running the Clock: CO2 Catalysis in the Age of Anthropocene. *ACS Energy Lett.* **2016**, *1* (1), 281–282. https://doi.org/10.1021/acsenergylett.6b00159.

(2) Pörtner, H.-O.; Roberts, D. C.; Adams, H.; Adler, C.; Aldunce, P.; Ali, E.; Begum, R. A.; Betts, R. *Climate Change 2022 - Impacts, Adaptation and Vulnerability - Summary for Policymakers*; 2022.

(3) Boot-Handford, M. E.; Abanades, J. C.; Anthony, E. J.; Blunt, M. J.; Brandani, S.; Mac Dowell, N.; Fernández, J. R.; Ferrari, M. C.; Gross, R.; Hallett, J. P.; Haszeldine, R. S.; Heptonstall, P.; Lyngfelt, A.; Makuch, Z.; Mangano, E.; Porter, R. T. J.; Pourkashanian, M.; Rochelle, G. T.; Shah, N.; Yao, J. G.; Fennell, P. S. Carbon Capture and Storage Update. *Energy Environ. Sci.* **2014**, *7* (1), 130–189. https://doi.org/10.1039/c3ee42350f.

(4) Al-Mamoori, A.; Krishnamurthy, A.; Rownaghi, A. A.; Rezaei, F. Carbon Capture and Utilization Update. *Energy Technol.* **2017**, *5* (6), 834–849. https://doi.org/10.1002/ente.201600747.

(5) Wu, J.; Zhou, X. D. Catalytic Conversion of CO2 to Value Added Fuels: Current Status, Challenges, and Future Directions. *Cuihua Xuebao/Chinese J. Catal.* **2016**, *37* (7), 999–1015. https://doi.org/10.1016/S1872-2067(16)62455-5.

(6) Aresta, M.; Dibenedetto, A. Utilisation of CO2 as a Chemical Feedstock: Opportunities and Challenges. *J. Chem. Soc. Dalt. Trans.* **2007**, No. 28, 2975–2992. https://doi.org/10.1039/b700658f.

(7) Sun, Z.; Ma, T.; Tao, H.; Fan, Q.; Han, B. Fundamentals and Challenges of Electrochemical CO 2 Reduction Using Two-Dimensional Materials. *CHEMPR* **2017**, *3* (4), 560–587. https://doi.org/10.1016/j.chempr.2017.09.009.

(8) Nitopi, S.; Bertheussen, E.; Scott, S. B.; Liu, X.; Engstfeld, A. K.; Horch, S.; Seger, B.; Stephens, I. E. L.; Chan, K.; Hahn, C.; Nørskov, J. K.; Jaramillo, T. F.; Chorkendorff, I. Progress and Perspectives of Electrochemical CO2 Reduction on Copper in Aqueous Electrolyte. *Chem. Rev.* **2019**, *119* (12), 7610–7672. https://doi.org/10.1021/acs.chemrev.8b00705.

(9) Ni, Z.; Liang, H.; Yi, Z.; Guo, R.; Liu, C.; Liu, Y.; Sun, H.; Liu, X. Research Progress of Electrochemical CO2 Reduction for Copper-Based Catalysts to Multicarbon Products. *Coord. Chem. Rev.* **2021**, *441*, 213983. https://doi.org/10.1016/j.ccr.2021.213983.

(10) ME, R. Réduction de l'acide Carbonique En Acide Formique. *Comptes Rendus Chim.* **1870**, 731–732.

(11) Hori, Y.; Kikuchi, K.; Suzuki, S. Production of CO and CH4 in Electrochemical Reduction of CO2 at Metal Electrodes in Aqueous Hydrogencarbonate Solution. *Chem. Lett.* **1985**, *14* (11), 1695–1698. https://doi.org/10.1016/S0075-7535(08)70092-5.

(12) Bagger, A.; Ju, W.; Varela, A. S.; Strasser, P.; Rossmeisl, J. Electrochemical CO2 Reduction: A Classification Problem. *ChemPhysChem* **2017**, *18* (22), 3266–3273. https://doi.org/10.1002/cphc.201700736.

(13) Hori, Y.; Murata, A.; Takahashi, R. Formation of Hydrocarbons in the Electrochemical Reduction of Carbon Dioxide at a Copper Electrode in Aqueous Solution. *J. Chem. Soc. Faraday Trans. 1 Phys. Chem. Condens.*

Phases **1989**, *85* (8), 2309–2326. https://doi.org/10.1039/F19898502309.
(14) Kuhl, K. P.; Cave, E. R.; Abram, D. N.; Jaramillo, T. F. New Insights into the Electrochemical Reduction of Carbon Dioxide on Metallic Copper Surfaces. *Energy Environ. Sci.* **2012**, *5* (5), 7050–7059. https://doi.org/10.1039/c2ee21234j.
(15) Hori, Y.; Wakebe, H.; Tsukamoto, T.; Koga, O. Adsorption of CO Accompanied with Simultaneous Charge Transfer on Copper Single Crystal Electrodes Related with Electrochemical Reduction of CO2 to Hydrocarbons. *Surf. Sci.* **1995**, *335* (C), 258–263. https://doi.org/10.1016/0039-6028(95)00441-6.
(16) De Gregorio, G. L.; Burdyny, T.; Loiudice, A.; Iyengar, P.; Smith, W. A.; Buonsanti, R. Facet-Dependent Selectivity of Cu Catalysts in Electrochemical CO2 Reduction at Commercially Viable Current Densities. *ACS Catal.* **2020**, *10* (9), 4854–4862. https://doi.org/10.1021/acscatal.0c00297.
(17) Gao, Y.; Wu, Q.; Liang, X.; Wang, Z.; Zheng, Z.; Wang, P.; Liu, Y.; Dai, Y.; Whangbo, M. H.; Huang, B. Cu2O Nanoparticles with Both {100} and {111} Facets for Enhancing the Selectivity and Activity of CO2 Electroreduction to Ethylene. *Adv. Sci.* **2020**, *7* (6), 1–7. https://doi.org/10.1002/advs.201902820.
(18) Hori, Y.; Koga, O.; Yamazaki, H.; Matsuo, T. Infrared Spectroscopy of Adsorbed CO and Intermediate Species in Electrochemical Reduction of CO2 to Hydrocarbons on a Cu Electrode. *Electrochim. Acta* **1995**, *40* (16), 2617–2622. https://doi.org/10.1016/0013-4686(95)00239-B.
(19) Hori, Y.; Takahashi, R.; Yoshinami, Y.; Murata, A. Electrochemical Reduction of CO at a Copper Electrode. *J. Phys. Chem. B* **1997**, *101* (36), 7075–7081. https://doi.org/10.1021/jp970284i.
(20) Feng, Y.; Roldan Cuenya, B. Revealing the CO Coverage-Driven C-C Coupling Mechanism for Electrochemical CO2Reduction on Cu2O Nanocubesvia OperandoRaman Spectroscopy SI. *Aldenderfer, Mark S., Craig, Nathan M., Speak. Robert Jeff, Popelka-Filcoff, Rachel S.* **1997**, *2* (1), 1–5.
(21) Sandberg, R. B.; Montoya, J. H.; Chan, K.; Nørskov, J. K. CO-CO Coupling on Cu Facets: Coverage, Strain and Field Effects. *Surf. Sci.* **2016**, *654*, 56–62. https://doi.org/10.1016/j.susc.2016.08.006.
(22) Schouten, K. J. P.; Qin, Z.; Gallent, E. P.; Koper, M. T. M. Two Pathways for the Formation of Ethylene in CO Reduction on Single-Crystal Copper Electrodes. *J. Am. Chem. Soc.* **2012**, *134* (24), 9864–9867. https://doi.org/10.1021/ja302668n.
(23) McMurry, J. E. *Organic Chemistry*, 8th ed.; Mary Finch, 2012.
(24) Dattila, F.; Garclá-Muelas, R.; López, N. Active and Selective Ensembles in Oxide-Derived Copper Catalysts for CO2Reduction. *ACS Energy Lett.* **2020**, *5* (10), 3176–3184. https://doi.org/10.1021/acsenergylett.0c01777.
(25) Chernyshova, I. V.; Somasundaran, P.; Ponnurangam, S. On the Origin of the Elusive First Intermediate of CO2 Electroreduction. *Proc. Natl. Acad. Sci. U. S. A.* **2018**, *115* (40), E9261–E9270. https://doi.org/10.1073/pnas.1802256115.
(26) Pan, Z.; Wang, K.; Ye, K.; Wang, Y.; Su, H. Y.; Hu, B.; Xiao, J.; Yu, T.; Wang, Y.; Song, S. Intermediate Adsorption States Switch to Selectively Catalyze Electrochemical CO2 Reduction. *ACS Catal.* **2020**, *10* (6), 3871–3880. https://doi.org/10.1021/acscatal.9b05115.

(27) An, H.; Wu, L.; Mandemaker, L. D. B.; Yang, S.; de Ruiter, J.; Wijten, J. H. J.; Janssens, J. C. L.; Hartman, T.; van der Stam, W.; Weckhuysen, B. M. Sub-Second Time-Resolved Surface-Enhanced Raman Spectroscopy Reveals Dynamic CO Intermediates during Electrochemical CO 2 Reduction on Copper. *Angew. Chemie* **2021**, *133* (30), 16712–16720. https://doi.org/10.1002/ange.202104114.
(28) Li, H.; Wei, P.; Gao, D.; Wang, G. ScienceDirect In Situ Raman Spectroscopy Studies for Electrochemical CO2 Reduction over Cu Catalysts. *Curr. Opin. Green Sustain. Chem.* **2022**, *34*, 100589. https://doi.org/10.1016/j.cogsc.2022.100589.
(29) Ruiter, J. De; An, H.; Wu, L.; Gijsberg, Z.; Yang, S.; Hartman, T.; Weckhuysen, B. M.; Stam, W. Van Der. Probing the Dynamics of Low-Overpotential CO2-to-CO Activation on Copper Electrodes with Time-Resolved Raman Spectroscopy. *J. Am. Chem. Soc.* **2022**. https://doi.org/10.1021/jacs.2c03172.
(30) Jin, L.; Seifitokaldani, A. In Situ Spectroscopic Methods for Electrocatalytic Co2 Reduction. *Catalysts* **2020**, *10* (5). https://doi.org/10.3390/catal10050481.
(31) Gunathunge, C. M.; Ovalle, V. J.; Li, Y.; Janik, M. J.; Waegele, M. M. Existence of an Electrochemically Inert CO Population on Cu Electrodes in Alkaline PH. *ACS Catal.* **2018**, *8* (8), 7507–7516. https://doi.org/10.1021/acscatal.8b01552.
(32) Gunathunge, C. M.; Li, J.; Li, X.; Waegele, M. M. Surface-Adsorbed CO as an Infrared Probe of Electrocatalytic Interfaces. *ACS Catal.* **2020**, *10* (20), 11700–11711. https://doi.org/10.1021/acscatal.0c03316.
(33) Zhan, C.; Dattila, F.; Rettenmaier, C.; Bergmann, A.; Kühl, S.; García-Muelas, R.; López, N.; Roldan Cuenya, B. Revealing the CO Coverage-Driven C–C Coupling Mechanism for Electrochemical CO2Reduction on Cu2O Nanocubesvia OperandoRaman Spectroscopy. *ACS Catal.* **2021**, *11* (13), 7694–7701. https://doi.org/10.1021/acscatal.1c01478.
(34) Sandberg, R. B.; Montoya, J. H.; Chan, K.; Nørskov, J. K. CO–CO Coupling on Cu Facets: Coverage, Strain and Field Effects. *Surf. Sci.* **2016**, *654*, 56–62. https://doi.org/10.1016/j.susc.2016.08.006.
(35) Moradzaman, M.; Mul, G. In Situ Raman Study of Potential-Dependent Surface Adsorbed Carbonate, CO, OH, and C Species on Cu Electrodes During Electrochemical Reduction of CO2. *ChemElectroChem* **2021**, *8* (8), 1478–1485. https://doi.org/10.1002/celc.202001598.
(36) Zahid, A.; Shah, A.; Shah, I. Oxide Derived Copper for Electrochemical Reduction of CO2 to C2+ Products. *Nanomaterials* **2022**, *12* (8), 1380. https://doi.org/10.3390/nano12081380.
(37) Yang, P. P.; Zhang, X. L.; Gao, F. Y.; Zheng, Y. R.; Niu, Z. Z.; Yu, X.; Liu, R.; Wu, Z. Z.; Qin, S.; Chi, L. P.; Duan, Y.; Ma, T.; Zheng, X. S.; Zhu, J. F.; Wang, H. J.; Gao, M. R.; Yu, S. H. Protecting Copper Oxidation State via Intermediate Confinement for Selective CO2 Electroreduction to C2+ Fuels. *J. Am. Chem. Soc.* **2020**, *142* (13), 6400–6408. https://doi.org/10.1021/jacs.0c01699.
(38) Kas, R.; Kortlever, R.; Milbrat, A.; Koper, M. T. M.; Mul, G.; Baltrusaitis, J. Electrochemical CO2 Reduction on Cu2O-Derived Copper Nanoparticles: Controlling the Catalytic Selectivity of Hydrocarbons. *Phys. Chem. Chem. Phys.* **2014**, *16* (24), 12194–12201. https://doi.org/10.1039/c4cp01520g.

(39) Arán-Ais, R. M.; Scholten, F.; Kunze, S.; Rizo, R.; Roldan Cuenya, B. The Role of in Situ Generated Morphological Motifs and Cu(i) Species in C2+ Product Selectivity during CO2 Pulsed Electroreduction. *Nat. Energy* **2020**, *5* (4), 317–325. https://doi.org/10.1038/s41560-020-0594-9.
(40) Lee, S. H.; Lin, J. C.; Farmand, M.; Landers, A. T.; Feaster, J. T.; Avilés Acosta, J. E.; Beeman, J. W.; Ye, Y.; Yano, J.; Mehta, A.; Davis, R. C.; Jaramillo, T. F.; Hahn, C.; Drisdell, W. S. Oxidation State and Surface Reconstruction of Cu under CO2Reduction Conditions from in Situ X-Ray Characterization. *J. Am. Chem. Soc.* **2021**, *143* (2), 588–592. https://doi.org/10.1021/jacs.0c10017.
(41) Permyakova, A. A.; Herranz, J.; El Kazzi, M.; Diercks, J. S.; Povia, M.; Mangani, L. R.; Horisberger, M.; Pătru, A.; Schmidt, T. J. On the Oxidation State of Cu2O upon Electrochemical CO2 Reduction: An XPS Study. *ChemPhysChem* **2019**, *20* (22), 3120–3127. https://doi.org/10.1002/cphc.201900468.
(42) Zhang, W.; Huang, C.; Xiao, Q.; Yu, L.; Shuai, L.; An, P.; Zhang, J.; Qiu, M.; Ren, Z.; Yu, Y. Atypical Oxygen-Bearing Copper Boosts Ethylene Selectivity toward Electrocatalytic CO2Reduction. *J. Am. Chem. Soc.* **2020**, *142* (26), 11417–11427. https://doi.org/10.1021/jacs.0c01562.
(43) Liu, C.; Lourenço, M. P.; Hedström, S.; Cavalca, F.; Diaz-Morales, O.; Duarte, H. A.; Nilsson, A.; Pettersson, L. G. M. Stability and Effects of Subsurface Oxygen in Oxide-Derived Cu Catalyst for CO2 Reduction. *J. Phys. Chem. C* **2017**, *121* (39), 25010–25017. https://doi.org/10.1021/acs.jpcc.7b08269.
(44) Zhang, D. F.; Zhang, H.; Guo, L.; Zheng, K.; Han, X. D.; Zhang, Z. Delicate Control of Crystallographic Facet-Oriented Cu2O Nanocrystals and the Correlated Adsorption Ability. *J. Mater. Chem.* **2009**, *19* (29), 5220–5225. https://doi.org/10.1039/b816349a.
(45) Mauritz, K. A.; Moore, R. B. State of Understanding of Nafion. *Chem. Rev.* **2004**, *104* (10), 4535–4585. https://doi.org/10.1021/cr0207123.
(46) Weekes, D. M.; Salvatore, D. A.; Reyes, A.; Huang, A.; Berlinguette, C. P. Electrolytic CO2 Reduction in a Flow Cell. *Acc. Chem. Res.* **2018**, *51* (4), 910–918. https://doi.org/10.1021/acs.accounts.8b00010.
(47) Higgins, D.; Hahn, C.; Xiang, C.; Jaramillo, T. F.; Weber, A. Z. Gas-Diffusion Electrodes for Carbon Dioxide Reduction: A New Paradigm. *ACS Energy Lett.* **2019**, *4* (1), 317–324. https://doi.org/10.1021/acsenergylett.8b02035.
(48) Burdyny, T.; Smith, W. A. CO2 Reduction on Gas-Diffusion Electrodes and Why Catalytic Performance Must Be Assessed at Commercially-Relevant Conditions. *Energy Environ. Sci.* **2019**, *12* (5). https://doi.org/10.1039/c8ee03134g.
(49) Moura de Salles Pupo, M.; Kortlever, R. Electrolyte Effects on the Electrochemical Reduction of CO2. *ChemPhysChem* **2019**, *20* (22), 2926–2935. https://doi.org/10.1002/cphc.201900680.
(50) Bouwens, R. E. A.; de Groot, P. A. M.; Kranendonk, W.; van Lune, J. P.; Prop - van den Berg, C. M.; van Riswick, J. A. M. H.; Westra, J. . *BiNaS*, 6th ed.; Noordhoff, 2013.
(51) Lucile, F.; Serin, J.; Houssin, D.; Arpentinier, P. Solubility of Carbon Dioxide in Water and Aqueous Solution Containing Sodium Hydroxide at Temperatures from (293.15 to 393.15) K and Pressure up to 5 MPa: Experimental Measurements. **2012**, *57* (3), 784–789.

(52) Wang, L.; Nitopi, S. A.; Bertheussen, E.; Orazov, M.; Morales-Guio, C. G.; Liu, X.; Higgins, D. C.; Chan, K.; Nørskov, J. K.; Hahn, C.; Jaramillo, T. F. Electrochemical Carbon Monoxide Reduction on Polycrystalline Copper: Effects of Potential, Pressure, and PH on Selectivity toward Multicarbon and Oxygenated Products. *ACS Catal.* **2018**, *8* (8), 7445–7454. https://doi.org/10.1021/acscatal.8b01200.
(53) Varela, A. S.; Kroschel, M.; Reier, T.; Strasser, P. Controlling the Selectivity of CO2 Electroreduction on Copper: The Effect of the Electrolyte Concentration and the Importance of the Local PH. *Catal. Today* **2016**, *260*, 8–13. https://doi.org/10.1016/j.cattod.2015.06.009.
(54) Cheng, T.; Xiao, H.; Goddard, W. A. Full Atomistic Reaction Mechanism with Kinetics for CO Reduction on Cu(100) from Ab Initio Molecular Dynamics Free-Energy Calculations at 298 K. *Proc. Natl. Acad. Sci. U. S. A.* **2017**, *114* (8), 1795–1800. https://doi.org/10.1073/pnas.1612106114.
(55) Ringe, S.; Chan, K.; Ringe, S.; Seger, B. Understanding Cation Effects in Electrochemical CO2 Reduction. **2019**, *12* (10). https://doi.org/10.1039/c9ee01341e.
(56) Shi, C.; Chan, K.; Yoo, J. S.; Nørskov, J. K. Barriers of Electrochemical CO2 Reduction on Transition Metals. *Org. Process Res. Dev.* **2016**, *20* (8), 1424–1430. https://doi.org/10.1021/acs.oprd.6b00103.
(57) Birdja, Y. Y.; Pérez-Gallent, E.; Figueiredo, M. C.; Göttle, A. J.; Calle-Vallejo, F.; Koper, M. T. M. Advances and Challenges in Understanding the Electrocatalytic Conversion of Carbon Dioxide to Fuels. *Nat. Energy* **2019**, *4* (9), 732–745. https://doi.org/10.1038/s41560-019-0450-y.
(58) Liu, X.; Xiao, J.; Peng, H.; Hong, X.; Chan, K.; Nørskov, J. K. Understanding Trends in Electrochemical Carbon Dioxide Reduction Rates. *Nat. Commun.* **2017**, *8* (May), 1–7. https://doi.org/10.1038/ncomms15438.
(59) Weller, M.; Overton, T.; Rourke, J.; Armstrong, F. *Inorganic Chemistry*, 6th ed.; 2014.
(60) Ball, D. W. *Physical Chemistry*, 2nd ed.; Cengage Learning, Inc, 2015.
(61) Ryczkowski, J. IR Spectroscopy in Catalysis. *Catal. Today* **2001**, *68* (4), 263–381. https://doi.org/10.1016/S0920-5861(01)00334-0.
(62) Stiles, P. L.; Dieringer, J. A.; Shah, N. C.; Van Duyne, R. P. Surface-Enhanced Raman Spectroscopy. *Annu. Rev. Anal. Chem.* **2008**, *1* (1), 601–626. https://doi.org/10.1146/annurev.anchem.1.031207.112814.
(63) Jeanmaire, D. L.; Duyne, R. P. VAN. Surface Raman Spectroelectrochemistry. *J. Electroanal Chem.* **1977**, *84*, 1.
(64) Ryan, C. G.; Clayton, E.; Griffin, W. L.; Sie, S. H.; Cousens, D. R. SNIP, a Statistics-Sensitive Background Treatment for the Quantitative Analysis of PIXE Spectra in Geoscience Applications. *Nucl. Inst. Methods Phys. Res. B* **1988**, *34* (3), 396–402. https://doi.org/10.1016/0168-583X(88)90063-8.
(65) Zhou, Z.; Li, X.; Li, Q.; Zhao, Y.; Pang, H. Copper-Based Materials as Highly Active Electrocatalysts for the Oxygen Evolution Reaction. *Mater. Today Chem.* **2019**, *11*, 169–196. https://doi.org/10.1016/j.mtchem.2018.10.008.
(66) Pang, Y.; Burdyny, T.; Dinh, C. T.; Kibria, M. G.; Fan, J. Z.; Liu, M.; Sargent, E. H.; Sinton, D. Joint Tuning of Nanostructured Cu-Oxide Morphology and Local Electrolyte Programs High-Rate CO2 Reduction to C2H4. *Green Chem.* **2017**, *19* (17), 4023–4030. https://doi.org/10.1039/c7gc01677h.
(67) Wang, J.; Tan, H.; Zhu, Y.; Chu, H.; Chen, H. M. Linking the Dynamic Chemical State of Catalysts with the Product Profile of Electrocatalytic CO 2

Reduction Angewandte. **2021**, 17254–17267. https://doi.org/10.1002/anie.202017181.
(68) Chang, C. J.; Hung, S. F.; Hsu, C. S.; Chen, H. C.; Lin, S. C.; Liao, Y. F.; Chen, H. M. Quantitatively Unraveling the Redox Shuttle of Spontaneous Oxidation/Electroreduction of CuOx on Silver Nanowires Using in Situ X-Ray Absorption Spectroscopy. *ACS Cent. Sci.* **2019**, *5* (12), 1998–2009. https://doi.org/10.1021/acscentsci.9b01142.
(69) Shen, J.; Hill, J. M.; Watwe, R. M.; Podkolzin, S. G.; Dumesic, J. A. Ethylene Adsorption on Pt / Au / SiO 2 Catalysts. *Catal. Letters* **1999**, *60*, 1–9.
(70) Jeon, H. S.; Timoshenko, J.; Rettenmaier, C.; Herzog, A.; Yoon, A.; Chee, S. W.; Oener, S.; Hejral, U.; Haase, F. T.; Roldan Cuenya, B. Selectivity Control of Cu Nanocrystals in a Gas-Fed Flow Cell through CO2Pulsed Electroreduction. *J. Am. Chem. Soc.* **2021**, *143* (19), 7578–7587. https://doi.org/10.1021/jacs.1c03443.

ACKNOWLEDGMENTS

First of all, I would like to greatly thanks my daily supervisor Jim de Ruiter. Doing my master thesis under your supervision has been a great pleasure in which I have learned an unimaginable amount of things. Besides learning a lot, you brought a pleasant environment socially in which I felt appreciated and had a lot of fun too; having a supervisor that (really) likes a borrel has its pros. You immediately took away the hierarchy of PhD and students and made me feel like we are all working together and not for each other. This thesis has been a full academic year, but it flew by. Thanks for everything!

Secondly, I want to thank dr. Ward van der Stam for all the help and discussion during my thesis. Having the discussions about my data were highly effective and always made me look at my own data and conclusions from a different angle. Just like Jim, you also brought a pleasant environment to work in, and it made my thesis much more enjoyable.

I would also like to thank dr. Matteo Monai for the insightful input during the discussion after my presentations. Your expertise always shed light on the parts which I looked over.

I want to thank Shuang Yang for her time and discussions, every time I had specific questions. You were always available and ready to help me which I greatly appreciate.

A special thanks goes out to Martijn Hut for making my time at ICC just so much more enjoyable. Besides all the fun times that we had; it was also very nice to have a master student on the same topic with which you can discuss your data with.

I thank Longfei Wu and Joren Dorresteijn for spending their time to measure beautiful SEM images for me.

Last but not least, I would like to thank all the other master students in the David de Wied building for making the days more joyful and the lunch breaks more fun.

Appendix A. Supplementary Figures

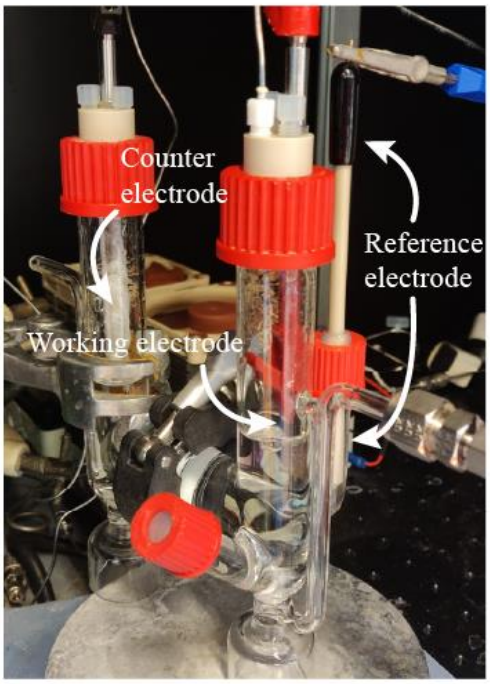

Figure 30: Picture of the H-cell for the catalytic tests with the three different electrodes.

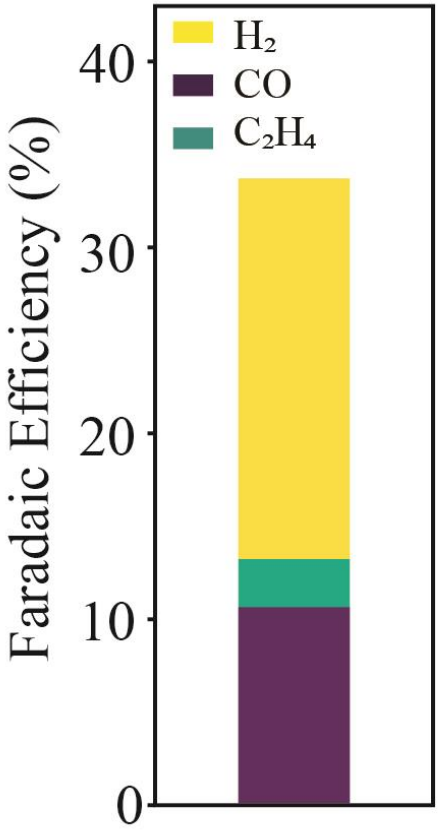

Figure 31: Catalytic selectivity of the octahedrons after 20 minutes at -1.0V. Only ~3% C_2H_4 is found at these overpotentials.

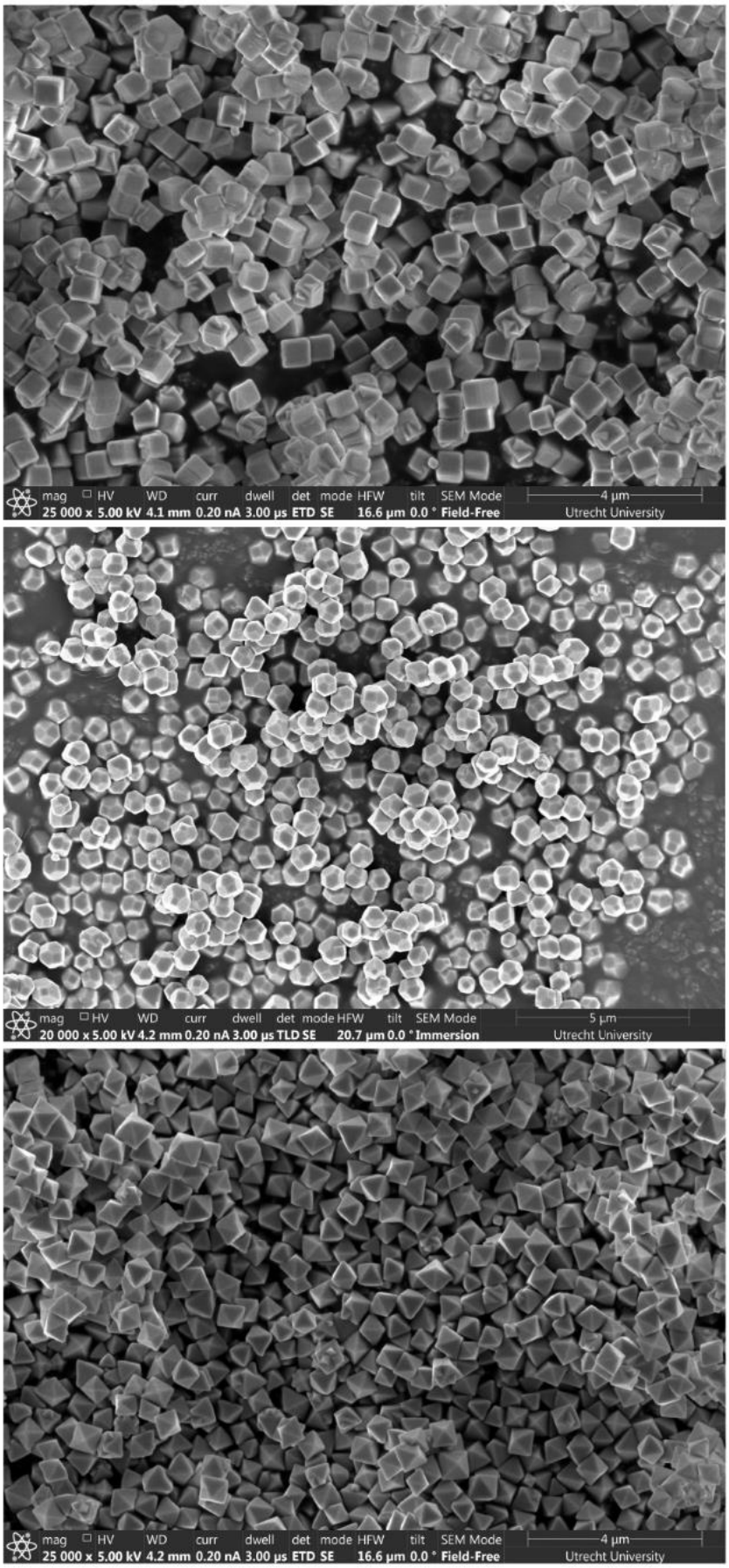

Figure 32: Zoomed out SEM images of the Cu_2O cubes (top), truncated-octahedrons (middle) and octahedrons (bottom).

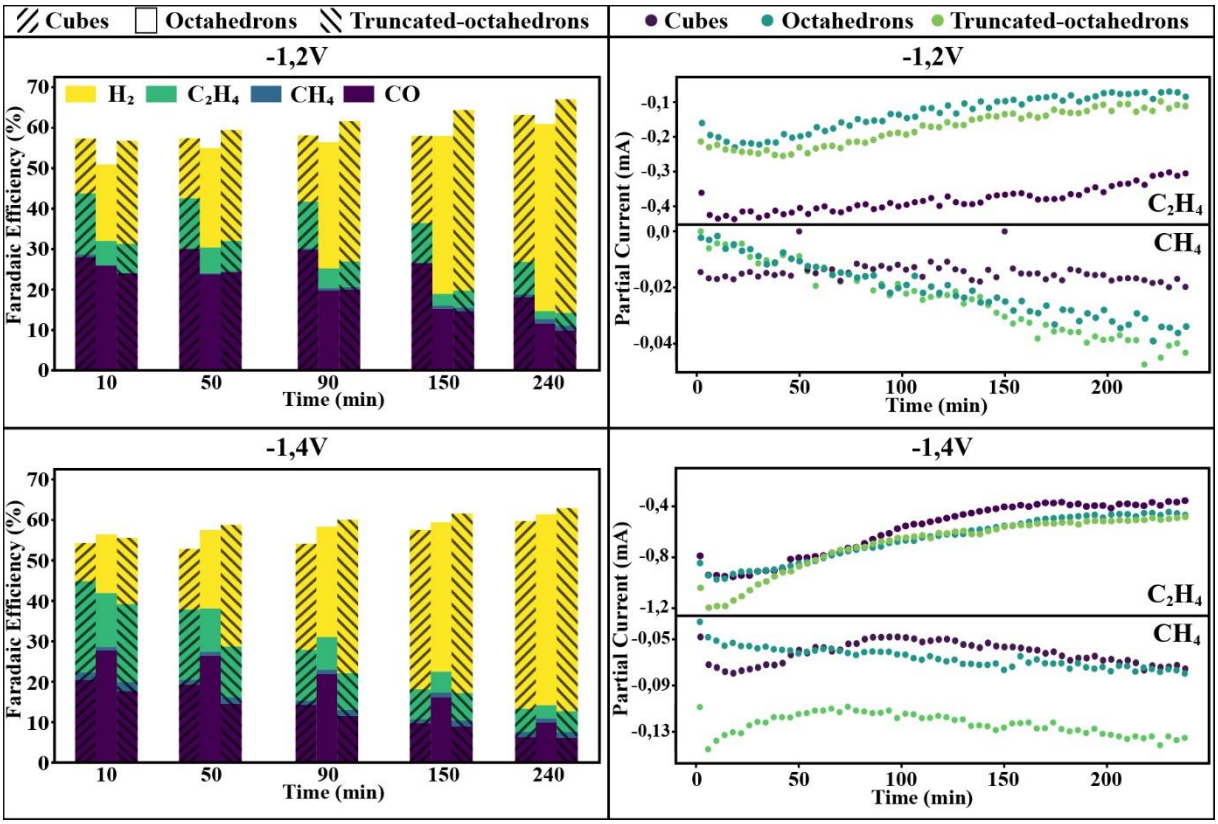

Figure 33: The duplo experiments of the time-dependent activity data for all three catalysts at -1,2V (top) & -1,4V (bottom). The left two graphs show the F.E. over time for all 4 the gas products, the right two graphs show the partial current over time for C_2H_4 and CH_4.

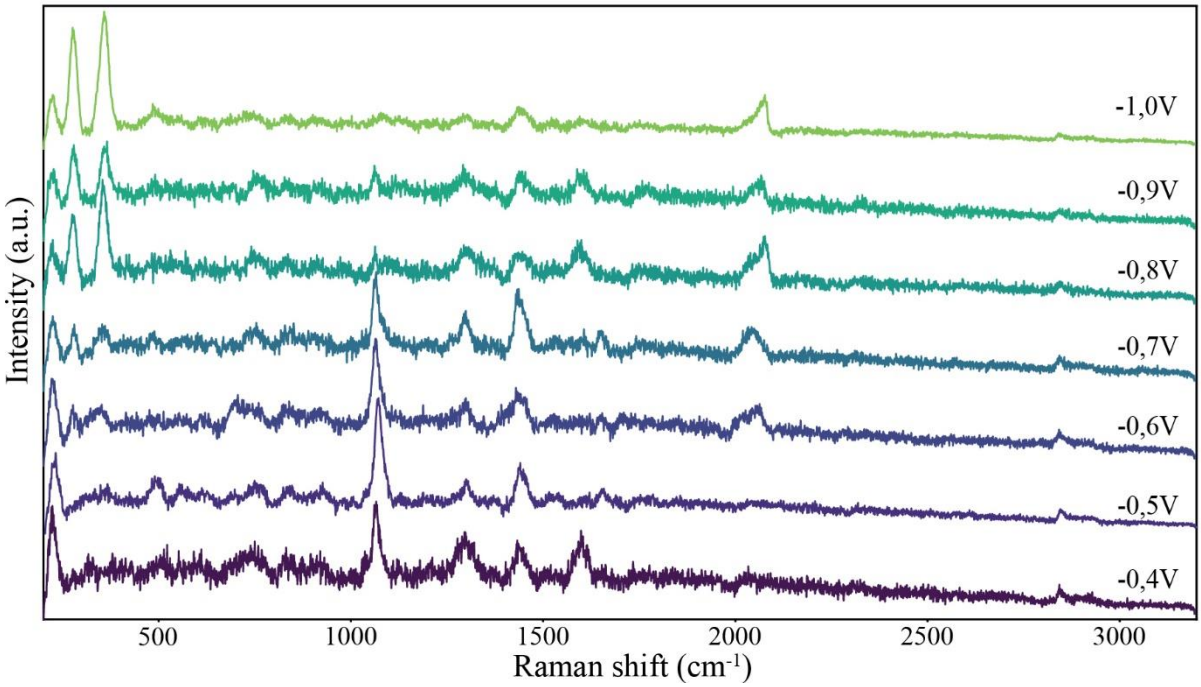

Figure 34: Average of 25 Raman spectra taken at the given overpotentials for the Cu_2O cubes in 0.1M $KHCO_3$.

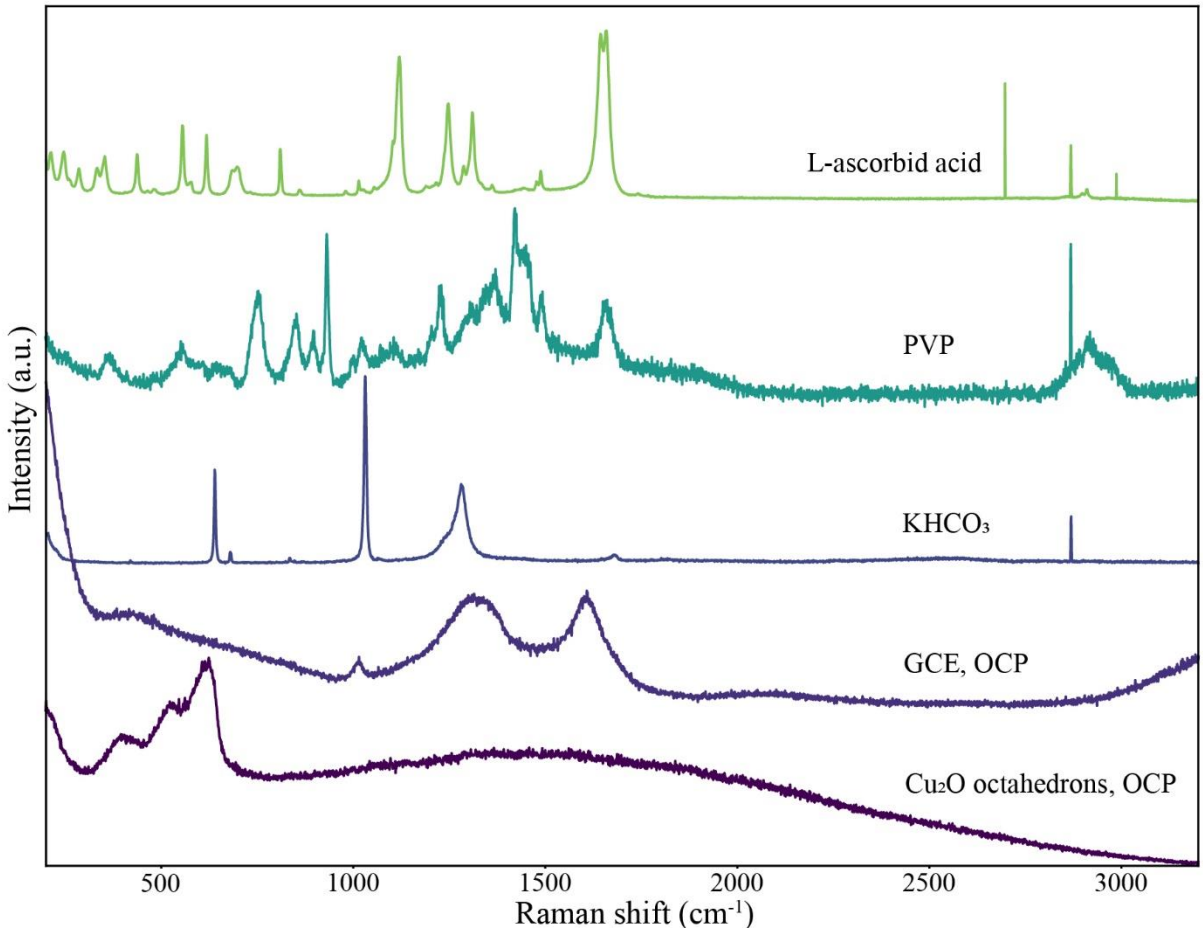

Figure 36: Raman spectra of the Cu_2O catalyst and the glassy carbon at OCP in CO_2-saturated 0.1M $KHCO_3$ (pH=6.8). The top three spectra are from $KHCO_3$, PVP, and l-ascorbid acid powders.

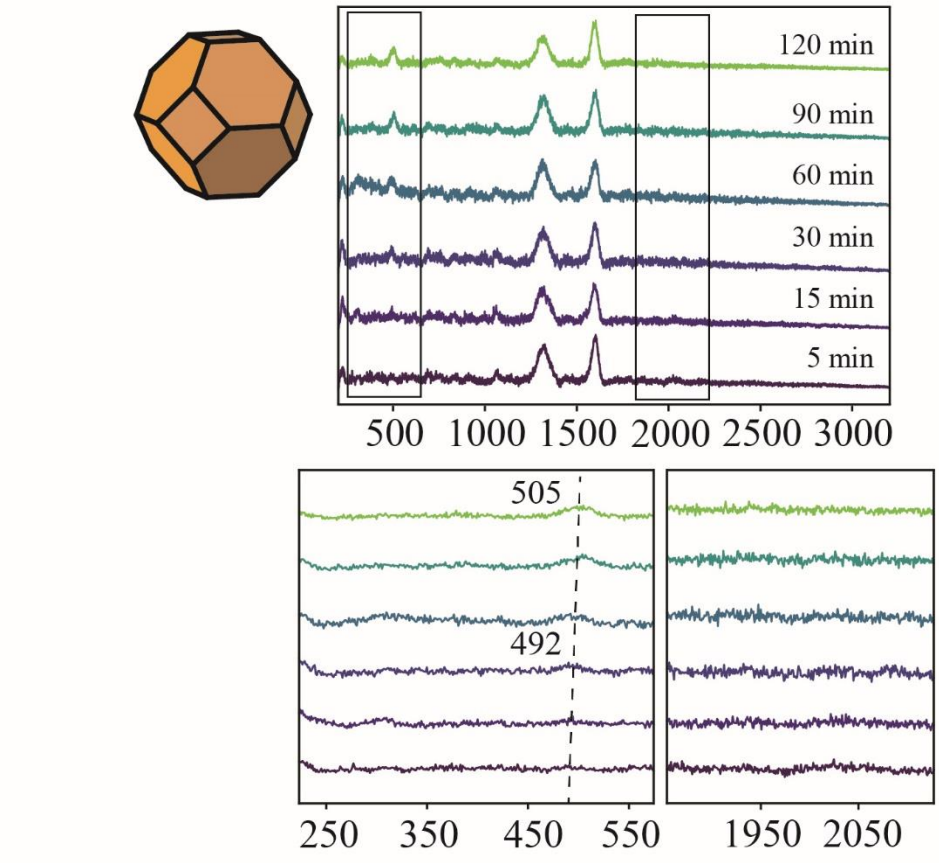

Figure 35: temporal Raman measurements of the truncated-octahedrons. The truncated-octahedrons gave very little signal from intermediates from the eCO2RR.